FACULDADE DE ENGENHARIA DA UNIVERSIDADE DO PORTO

Design and manufacturing of a carbon fibre-reinforced accumulator container for a Formula Student-spec car

Renato Silva Costa

Master in Mechanical Engineering

Supervisor: Prof. Albertino Arteiro

Company Supervisor: Eng. Frederico Ribeiro

July 20, 2024

© Renato Silva Costa, 2024

Design and manufacturing of a carbon fibre-reinforced accumulator container for a Formula Student-spec car

Renato Silva Costa

Master in Mechanical Engineering

July 20, 2024

Resumo

Nos últimos anos, o mercado e a indústria dos veículos elétricos têm vindo a evoluir a um ritmo acelerado, uma vez que a procura de energia e transportes mais sustentáveis é cada vez mais forte. Com esta maior procura, surgem novos desafios, como a autonomia e a eficiência. O peso desempenha um papel importante nestes dois parâmetros, pelo que a redução do peso é fundamental para o desempenho dos veículos eléctricos. Por outro lado, os materiais compósitos, especialmente os polímeros reforçados de fibras de carbono (CFRP), oferecem uma alternativa de baixo peso aos materiais metálicos clássicos.

Num veículo, um componente cujas propriedades mecânicas podem ser melhoradas por materiais compósitos, reduzindo simultaneamente o peso estrutural, é o contentor da bateria. A utilização de materiais compósitos neste componente está a tornar-se mais comum, quer em veículos de alto desempenho, como os desportos motorizados, quer em veículos de transportes regulares. Os materiais compósitos não só têm uma relação resistência/peso mais elevada, como também oferecem outras vantagens, tais como baixa condutividade e maior rigidez. Têm também a possibilidade de fabricar formas mais complexas.

Tal como no caso dos desportos motorizados de alto desempenho, os materiais compósitos podem ser utilizados em contextos relacionados com a engenharia, como as competições realizadas para promover a integração dos estudantes. A Formula Student é uma competição mundial em que os estudantes são desafiados a conceber e fabricar carros de corrida do tipo fórmula. Estes carros podem ter um grupo motopropulsor a combustão, elétrico ou híbrido. Um componente crucial de um carro elétrico é a sua bateria e, consequentemente, o seu contentor, que garante a integridade estrutural e a segurança. Este contentor é fabricado por muitas equipas em alumínio. No entanto, muitas equipas optaram por passar a utilizar materiais compósitos, acompanhando o mercado dos veículos elétricos.

Neste trabalho, é proposta a conceção de um contentor em CFRP para melhorar o desempenho e a segurança do componente. Após algumas iterações de design, o desempenho da caixa de bateria concebida em CFRP é investigado através de simulações de elementos finitos. Isto foi feito não só para conhecer o comportamento da nova estrutura, mas também para garantir que cumpre os regulamentos das competições em que o carro vai participar. Foi também efectuada uma revisão dos modelos analíticos utilizando as teorias clássicas dos compósitos, o que levou à comparação de alguns dos modelos com os ensaios experimentais realizados posteriormente neste trabalho. Foram realizadas simulações de otimização de camadas para casos de carregamento críticos utilizando o ALTAIR Hypermesh, a fim de reduzir o peso ou aumentar a resistência em áreas seleccionadas. Finalmente, foram efectuados ensaios experimentais com um material semelhante ao da caixa do acumulador para criar um fluxo de trabalho a utilizar nos ensaios do material utilizado na caixa da bateria.

Keywords: Compósitos, Veículos elétricos, Análise de Elementos Finitos, Formula Student, Contentor da bateria, Simulação, Testes de flexão.

Abstract

In the past years, the electric vehicle market and industry have been evolving at a fast pace, as the search for more sustainable energy and transportation is becoming even stronger. With this higher demand, new challenges arrive, such as autonomy and efficiency. Weight plays an important role in those two parameters, thus lower weight is key to the performance of electric vehicles. On the other hand, composite materials, especially carbon-fibre reinforced polymers (CFRP), offer a low-weight alternative to classic metallic materials.

In a vehicle, one component whose mechanical properties can be improved by composite materials while reducing structural weight is the battery container. The use of composite materials in this component is becoming more common, whether in high-performance vehicles, like Motorsport, or regular transportation. Composite materials not only have a higher strength-to-weight ratio but also offer other advantages, such as low conductivity and higher stiffness. They also have the possibility to manufacture more complex shapes.

Just like in the case of high performance motorsports, composite materials my be used in engineering-related context, such as competitions held to promote the integration of students. Formula Student is a worldwide competition where students are challenged to design and manufacture formula-type racecars. These cars can have a combustion, electric or hybrid powertrain. One crucial component of an electric car is its battery and, consequently, its container, which ensures structural integrity and safety. This container is manufactured by many teams using aluminium. However, many teams have chosen to move to composite materials, following the electric vehicle market.

In this work, the design of a CFRP container is proposed to improve both the performance and safety of the component. After some design iterations, the performance of the CFRP-designed battery box is investigated via Finite Element simulations. This was done not only to know the behaviour of the new structure but also to ensure that it follows the regulations of the competitions where the car is going to be enter in. A review on analytical models using classical composite theories was also conducted leading to the comparison of some of the models to the experimental tests performed later in this work. Lay-up optimisation simulations for critical load cases were carried out using ALTAIR Hypermesh in order to reduce weight or increase strength in select areas. Finally, experimental tests were carried out with a material similar to that of accumulator box to create a workflow to be used when testing the material used in the battery box.

Keywords: Composites, Electric vehicles, Finite elements analysis, Formula Student, Battery container, Simulation, Flexural tests.

Acknowledgments

First of all, I would like to thank my supervisors, Prof. Albertino Arteiro and Eng. Pedro Campos, for accepting my theme and for all the help and knowledge given throughout my project.

Then, I am very grateful to all the staff in Dragon Equation, especially to Eng. Frederico Ribeiro and Eng. Gerardo Menezes, that were always available to help and support me through the last months.

To my family, for their unconditional love. This could never have been done without their support over these last five years. I am extremely grateful to my parents' effort to give me such an opportunity that they provided me by affording all the costs of the course. This achievement is also theirs. To my brothers, for always listening and supporting me when I needed them and for never letting me down.

To my girlfriend, Beatriz, who over the last years has heard me complaining, overthinking, and going through an existential crisis, but never failed to be by my side both in the good and bad moments, celebrating or crying. Without you, this final journey would have been much more difficult. Thank you for always listening and loving me.

To all members of Formula Student FEUP, who I have shared countless hours designing and manufacturing what at first seemed to be impossible. To all the good and bad moments that got us where we are. To all the nights in the lab building our dream. All the hours that I didn't sleep made me learn about engineering and my limits.

I would also like to thank all of my friends who have walked this path with me. These five years with you were incredible, whether it was studying, partying or even just existing. You have made this walk easier and worth it. May this be just the end of the beginning of the rest of our lives.

Finally, there is a special friend that I would like to thank the most. To you, Gonçalo Caldas. Without your help over the last few years, I would not be finishing now. Thank you for all the support, for all the work when I couldn't be present, and for always helping me study for the exams. You were my first university friend and I'm glad we've made it all the way to the end.

Renato Silva Costa

"Success is not final, failure is not fatal, it is the courage to continue that counts."

Winston Churchill

Contents

1 Introduction **1**
- 1.1 The evolution of electric cars . . . 1
- 1.2 Formula Student . . . 2
  - 1.2.1 Brief history of Formula Student . . . 2
  - 1.2.2 The competition . . . 3
  - 1.2.3 Formula Student FEUP . . . 7
- 1.3 Powertrain of an electric vehicle . . . 7
  - 1.3.1 Road car electric powertrain . . . 8
  - 1.3.2 Formula Student car electric powertrain . . . 8
- 1.4 Motivation . . . 10
- 1.5 Thesis structure . . . 10

2 Literature review **12**
- 2.1 Battery housings . . . 12
  - 2.1.1 Composite battery housings in road cars . . . 12
  - 2.1.2 Composite battery enclosures in Formula 1 . . . 13
  - 2.1.3 Composite TSAC in Formula Student . . . 14
- 2.2 Aluminium vs Composite containers . . . 15
- 2.3 Classical Lamination Theory . . . 16
  - 2.3.1 ABD matrices special cases . . . 18
  - 2.3.2 Laminate apparent stiffness . . . 18
- 2.4 Failure criteria . . . 19
  - 2.4.1 Maximum stress criterion . . . 19
  - 2.4.2 Maximum strain criterion . . . 19
  - 2.4.3 Tsai-Hill criterion . . . 20
  - 2.4.4 Tsai-Wu criterion . . . 20
  - 2.4.5 Hashin criteria . . . 20
  - 2.4.6 Other criteria . . . 21
- 2.5 First vs Last ply failure . . . 22
- 2.6 Composites characterisation for battery containers . . . 22
  - 2.6.1 Tensile testing . . . 22
  - 2.6.2 Three-point bending . . . 25
  - 2.6.3 Four-point bending . . . 27
  - 2.6.4 Perimeter shear strength testing . . . 28

3 Targets and constraints **30**
3.1 Weight . . . 30
3.2 Position and dimensions . . . 32
3.3 Contained components . . . 33
3.4 Material . . . 34

4 Numerical implementations **36**
4.1 Three-point bending test . . . 36
4.1.1 User input . . . 36
4.1.2 CLT implementation . . . 38
4.1.3 Failure criteria . . . 38
4.1.4 Stiffness degradation . . . 39
4.1.5 Output . . . 39
4.1.6 Model validation . . . 40
4.2 Container optimisation . . . 42
4.2.1 The process . . . 42
4.2.2 Lid optimisation . . . 43
4.2.3 Container optimisation . . . 58

5 Design validation **81**
5.1 Material selection . . . 81
5.2 Manufacturing . . . 81
5.3 Specimen geometry . . . 84
5.4 Testing . . . 86
5.4.1 Three-point bending . . . 86
5.4.2 Four-point bending . . . 91
5.4.3 Comparison and analysis . . . 93

6 Design for manufacturing **95**
6.1 Lid design . . . 96
6.2 Bottom container design . . . 96
6.2.1 Main structure . . . 96
6.2.2 Transverse internal walls . . . 96
6.2.3 Eletronics stand-off and HV-LV separation plate . . . 97
6.2.4 Chassis mounts . . . 97
6.2.5 Lid mounts . . . 97

7 Conclusions and future work **99**
7.1 Conclusions . . . 99
7.2 Future work . . . 100

References **101**

A Code **104**
A.1 Main code . . . 104
A.2 Functions code . . . 110

B Code validation **119**
B.1 Laminate 1 119
B.2 Laminate 2 121
B.3 Laminate 3 123
B.4 Laminate 4 125

List of Figures

1.1 Manual and DV Skidpad layout. . . . 4
1.2 Points distribution per event. . . . 5
1.3 Tilt test. . . . 6
1.4 Rain test. . . . 6
1.5 FS FEUP with it first car in FSG. . . . 7
1.6 (a) One inboard motor at the rear of the car (configuration a); (b) two outboard or inboard motors at the rear of the car (configuration b); (c) one rear motor and two outboard in-wheel front motors (configuration c); (d) four motors (configuration d). 10

2.1 Composite material battery enclosures from SGL Carbon. . . . 13
2.2 Accumulator container material distribution in FSG 2023. . . . 15
2.3 Laminate cross-section example. . . . 16
2.4 Schematic representation of a tensile test specimen. . . . 23
2.5 Three-point bending case approximation. . . . 26
2.6 4PB test setup representation. . . . 27

3.1 Car weight distribution by team in FSG 2023. . . . 30
3.2 FSFEUP 01 weight distribution. . . . 31
3.3 Weight of the FSFEUP first car accumulator. . . . 32
3.4 Accumulator position in the car. . . . 33
3.5 Cell segment. . . . 34
3.6 Accumulator representation. . . . 34

4.1 Three-point bending model flowchart. . . . 37
4.2 Code validation graphically represented for first laminate: (a) σ_{xx}; (b) σ_{11}; (c) ε_{xx}; (d) ε_{11}. . . . 42
4.3 Lid optimisation geometry. . . . 43
4.4 Lid optimisation initial lay-up. . . . 45
4.5 Boundary condition applied to all nine holes in the lid. . . . 45
4.6 Load applied to the lid. . . . 46
4.7 Geometry around the hole in the lid. . . . 47
4.8 Mesh around the hole in the lid. . . . 47
4.9 Plot of lid mesh convergence study. . . . 48
4.10 Lid mesh convergence displacement field. . . . 48
4.11 Lid mesh convergence: (a) Major principal stress; (b) Minor principal stress; (c) Shear stress; (d) Tsai-Wu failure index. . . . 50
4.12 Lid free-sizing step element thickness. . . . 51

4.13 0-degree CFRP ply reinforcement shapes according to load path after free-sizing: (a) main shape; (b) main reinforcement; (c) second reinforcement shape; (d) small reinforcement shape. . . . 52
4.14 CFRP ply shapes: (a) whole compoenent; (b) reinforcement. . . . 52
4.15 Element thickness after continuous sizing. . . . 53
4.16 Element thickness after discrete sizing. . . . 54
4.17 Lid layup shuffling iterations. . . . 55
4.18 Shuffling lid: (a) displacement field; (b) Tsai-Wu failure index. . . . 56
4.19 Lid layup shuffling Tsai-Wu failure index filtered to values greater than 1. . . . 57
4.20 Final lid simulation: (a) displacement field; (b) Tsai-Wu failure index. . . . 58
4.21 Final lid Tsai-Wu failure index filtered to values greater than 1. . . . 59
4.22 Bottom container geometry: (a) front isometric view; (b) rear isometric view. . . . 59
4.23 Bottom container optimisation boundary conditions. . . . 61
4.24 Bottom container load cases: (a) 40g longitudinal direction 1; (b) 40g longitudinal direction 2; (c) 40g transversal direction 1; (d) 40g transversal direction 2; (e) 20g vertical direction. . . . 62
4.25 Bottom container mesh refinement: (a) around connector holes; (b) around cooling holes. . . . 62
4.26 Bottom container mesh convergence study. . . . 64
4.27 Bottom container free-sizing step element thickness. . . . 65
4.28 0-degree CFRP ply reinforcement shapes according to load path after free-sizing for the bottom container: (a) main shape; (b) main reinforcement; (c) second reinforcement shape; (d) small reinforcement shape. . . . 65
4.29 Bottom container optimisation shapes: (a) External walls; (b) Internal walls. . . . 66
4.30 Bottom container element thickness after continuous sizing. . . . 67
4.31 Bottom container element thickness after discrete sizing. . . . 68
4.32 Bottom layup shuffling iterations. . . . 68
4.33 Shuffling results bottom container . . . 74
4.34 Final results bottom container. . . . 79

5.1 Prepeg nesting and cutting pattern. . . . 82
5.2 Stacked plies, forming the two plates. . . . 82
5.3 Plates inside the vacuum bag. . . . 83
5.4 Stacked plies, forming the two plates. . . . 83
5.5 Manufacturing log: (a) temperature; (b) pressure. . . . 84
5.6 Plates after the curing process. . . . 84
5.7 Three-point test setup. . . . 86
5.8 Three-point bending results. . . . 87
5.9 Damage variable study with different failure criteria: (a) maximum stress; (b) maximum strain; (c) Tsai-Hill; (d) Tsai-Wu. . . . 89
5.10 Shear stress contribution for the adapted Hashin failure criteria. . . . 90
5.11 Experimental results compared to the best-fitted curve for each failure criterion. . . . 91
5.12 Four-point test setup. . . . 92
5.13 Four-point bending results. . . . 94
5.14 Three-point and four-point bending results compilation. . . . 94

6.1 Container final design. . . . 95
6.2 Aluminium placers for the electronics plate. . . . 97
6.3 Aluminium chassis mount. . . . 98

List of Tables

2.1 Dimensions for the specimen in Figure 2.4. . . . 23
2.2 Dimensions for the specimen according to ASTM D7264 recommendations. . . . 25

3.1 Legend for the Histogram in Figure 3.2. . . . 31

4.1 Material elastic properties used for validation. . . . 40
4.2 Material failure properties used for validation. . . . 40
4.3 Material elastic properties and density for lid optimisation. . . . 44
4.4 Material failure properties used for lid optimisation. . . . 44
4.5 Master laminate for lid optimisation. . . . 45
4.6 Results of mesh convergence study. . . . 48
4.7 Lid ply thickness after continuous sizing. . . . 53
4.8 Lid ply thickness after discrete sizing. . . . 54
4.9 Lid layup after shuffling. . . . 55
4.10 Lid layup after reordering. . . . 57
4.11 Master laminate for bottom optimisation. . . . 60
4.12 Mesh convergence study results for 40g longitudinal front to back load case. . . . 63
4.13 Mesh convergence study results for 40g longitudinal back to front load case. . . . 63
4.14 Mesh convergence study results for 40g transversal left to right load case. . . . 63
4.15 Mesh convergence study results for 40g transversal right to left load case. . . . 63
4.16 Mesh convergence study results for 20g vertical downwards load case. . . . 64
4.17 Lid ply thickness after continuous sizing. . . . 67
4.18 Lid ply thickness after discrete sizing. . . . 67
4.19 Lid layup after shuffling. . . . 69
4.20 Bottom container layup after reordering. . . . 69

5.1 Carbon fibre pre-preg Toray E745/IM7 properties. . . . 81
5.2 Specimen dimensions. . . . 85
5.3 Three-point bending testing dimensions. . . . 86
5.4 Three-point bending results. . . . 87
5.5 First ply failure data for every failure criteria. . . . 88
5.6 Four-point bending testing dimensions. . . . 92
5.7 Four-point bending results. . . . 92

Nomenclature and Symbols

Nomenclature

3D	Three-dimensional
3PB	Three-point bending
4PB	Four-point bending
AMS	Accumulator Management System
BCs	Boundary Conditions
CH	Chassis
CLT	Classical Lamination Theory
CFRP	Carbon Fibre reinforced Polymer
CO	Cooling System
CV	Combustion Vehicle
DI	Driver's Interface
DV	Driverless Vehicle
ES	Electric Systems
EVs	Electric Vehicles
FEUP	Faculty of Engineering of the University of Porto
FPF	First Ply Failure
FS	Formula Student
FSG	Formula Student Germany
FS FEUP	Formula Student FEUP
GFRP	Glass Fibre reinforced Polymer
ICEs	Internal Combustion Engine vehicles
IMechE	Institution of Mechanical Engineers
LPF	Last Ply Failure
MGU-H	Motor Generator Unit Heat
MGU-K	Motor Generator Unit Kinetic
PU	Power Unit
SAE	Society of Automotive Engineers
SES	Structural Equivalency Spreadsheet
SMC	Sheet Moulding Compound
SMC-CF	Sheet Moulding Compound - Carbon Fibre
SS	Steering System
TR	Transmission
TS	Tractive System
TSA	Tractive System Accumulator
TSAC	Tractive System Accumulator Container
VB	Vibrations
WA	Wheel Assembly

WB	Wishbones

Symbols

N, N_x, N_y, N_s, M_x, M_y, M_s	External Mechanical Forces per Unit, [N/mm]
σ_1, σ_2, σ_{12}, τ_{12}	Stress in the principal directions, [MPa]
ε_1, ε_2, ε_{12}, γ_{12}	Strain in the principal directions, [-]
Q,	Stiffness Matrix of lamina
E_1, E_2	Young's Moduli, [GPa]
G_{12}, G_{23}	Shear Moduli, [GPa]
ν_{12}, ν_{21}, ν_{23}	Poisson's Ratio, [-]
θ	Ply angle [°]
m, n	cossine and sine of θ
P, A, B, D	Stiffness matices of laminate
z	Lamina height coordinate [mm]
γ^0_{xy}	Midplane Shear Strain
k_{xx}, k_{yy}	Bending Curvutures
k_{xy}	Twisting Curvuture
E_{xx}	Stiffness in the x direction, [MPa]
E_y	Stiffness in the y direction, [GPa]
ν_{xy}	Laminate apparent Poisson's ratio, [-]
t	laminate thickness, [mm]
X_t	Tensile strength in the longitudinal direction, [MPa]
Y_t	Tensile strength in the transverse direction, [MPa]
X_c	Compressive strength in the longitudinal direction, [MPa]
Y_c	Compressive strength in the transverse direction, [MPa]
X'_t	Allowable tensile strain in the longitudinal direction, [-]
Y'_t	Allowable tensile strain in the transverse direction, [-]
X'_c	Allowable compressive strain in the longitudinal direction, [-]
Y'_c	Aallowable compressive strain in the transverse direction, [-]
F	Tsai-Wu factors
d	Degraded factor
E^d_1, E^d_2, G^d_{12}	Degraded properties, [GPa]
L, B, h	Tensile specimen dimension, [mm]
σ_{UTS}	Ultimate Tensile Strength, [MPa]
F_{max}	Tensile maximum load, [N]
A	Specimen transversal area, [mm^2]
ε_U	Ultimate Tensile Strain, [-]
δl	Displacement, [mm]
v_{max}	Maximum displacement on 3PB, [mm]
I	Second moment of area, [mm^4]
P	3PB/4PB load, [N]
l	Support span, [mm]
t	Specimen's thickness, [mm]
σ_f	Flexural Strength, [MPa]
b	3PB/4PB Specimen width, [mm]
m	3PB/4PB Slope of the secant of the force-deflection curve, [-]
ε_{max}	Maximum strain [-]

δ	Mid-span vertical displacement, [mm]
σ_s is the material's shear strength, [MPa]	
P_{max}	Maximum load, [N]
D	Extruder diameter, [mm]
t_1	Upper skin thickness, [mm]
g	Gravitical acceleration, $[m/s^2]$
W	Weight, [kg]
ρ	Density, $[kg/cm^3]$
F_{40g}, F_{20g}	Load from rules load cases, [N]
P_{trans}, P_{long}, P_{vert}	Stress applied from rules load cases, [MPa]

Chapter 1

Introduction

1.1 The evolution of electric cars

Nowadays, there is considerable affluence to electric transportation, with electric car sales breaking records in 2022 and the momentum expected to continue in 2023 (Agency, 2023).

However, the history of electric vehicles dates back to the 19^{th} century. The first electric vehicles (EVs) appeared in the 1830s, with varying claims of who invented the electric car (EVBox, 2021).

During this decade, different concepts of non-rechargeable EVs appeared through the American Thomas Davenport in 1834 or the Scottish Robert Anderson between 1832 and 1839 (EAA, 2021). It is also said that the Hungarian Ányos Jedlik and the Dutch professor Sibrandus Stratingh designed their own electric vehicle (EVBox, 2021). These small vehicles and carriages remained non-chargeable until the 1860s when Gaston Plant invented lead-acid batteries (EAA, 2021).

The improvement of electric batteries came in the late 1800s when France, England, and later Switzerland started manufacturing EVs (Chan, 2013). As the Europeans were evolving and doing better electric cars, it was only in 1895 that the Americans shifted their attention to the EVs (Chan, 2013).

In the last decade of the 19th century, the EVs gained even more momentum. As stated in Chan (2013), in 1897, the London Electrical Cab Company had a fleet of 15 cars, and by the end of 1898, Pope Manufacturing Company had already manufactured 500 EVs.

The first commercial electrical fleet appeared in 1897 in New York with a small fleet of taxis (Warner, 2015). At this time, most automotive cars, powered by steam, electricity, or internal combustion (ICEs), were the property of "fleet owners for use in taxis", as Warner (2015) stated.

With more companies entering the EVs manufacturing business, the commercialization of EVs started growing due to the advantages in relation to the early ICEs. They were quiet, did not induce harsh vibrations, and had no smell, which conquered the consumers (Warner, 2015). One of the problems of EVs was their range. However, this was not a problem since the road network was still small (Warner, 2015).

However, with the automotive evolution, the road network improved over the years. During the 1920s, the United States road network connected large cities, which imposed the need for cars with more range (Chan, 2013). By that time, EVs had approximately a range of 50 to 100 miles (Warner, 2015). Furthermore, the crude discovered in Texas led to cheaper and affordable gasoline (Chan, 2013). Allying that with the quick pace of the ICE evolution, Henry Ford's Model T, and the introduction of Charles Kettering's automatic starter in 1911, the ICEs started to gain popularity over the EVs. By the end of the 1950s, no company manufactured them (Warner, 2015).

Around the 1970s, the interest in EVs rose again because of an oil crisis due to the low efficiency of fuel cars and the awareness of environmental problems. The car companies started investing in research of other types of propulsion, such as electrification or alternative fuels. However, only twenty years later, the first cars started being produced again, in parallel with hybrid cars (Warner, 2015).

Since then, interest in more sustainable vehicles have risen up to the level found nowadays due to battery evolution and sustainable development policies (Tie and Tan, 2013), leading to an inherent increase in research and development in this topic.

1.2 Formula Student

Formula Student (FS) is a worldwide engineering competition that challenges students to design and manufacture a formula-type race car prototype, offering the chance to apply theoretical knowledge learned in the university into practice.

1.2.1 Brief history of Formula Student

The first competition was created in 1980 by the Society of Automotive Engineers (SAE) student branch by Ron Matthews, an Assistant Professor at the University of Texas. After hearing that the SAE's Mini Indy competition had ended, Matthews and three new officers decided to create a new one with different rules: the Formula SAE (Case, 1996). The organisation had grown over the years, becoming a reference for the American and Australian competitions.

The competition reached Europe in 1998 with a showdown with three American and four British teams. During the same year, the Institute of Mechanical Engineers (IMechE) agreed with the SAE to run the event in Europe (IMechE, 2021). Nowadays, IMechE runs a Formula Student event in Silverstone every year.

Later in 2005, the first Formula Student Germany (FSG) event happened with dynamics events only (FSG, 2023b). As the years went by, this competition turned into the best in the world, with most European competitions following its rules book. For this reason, this thesis will focus on the FSG rules.

Currently, three organisations make a ruleset, which other competitions follow. Those are Formula SAE, IMechE, and FSG. There are a total of twenty-six worldwide competitions (FSG, 2023b).

1.2.2 The competition

FSG has three classes: combustion (CV), electric (EV) or hybrid. There is also an extra driverless class (DV). However, with the evolution of the road cars market and technology toward electric and driverless vehicles, the competitions are decreasing the slots for CVs, increasing the ones for EVs and giving more emphasis to DVs. In fact, FSG had already closed the CV competition, making the 2023 edition the last one.

There are two types of events in a competition: Static Events, where the judges evaluate the knowledge of the team about engineering, cost, and manufacturing, and Dynamic Events, where the car performance is what matters to have good score.

1.2.2.1 Static events

There are three Static Events in the competition: Business Plan Presentation Event, Cost and manufacturing Event, and Engineering Design Event (FSG, 2023a).

- **Business Plan Presentation Event:** In this event, the judges act like investors open to new market opportunities. The main product to sell is the team's car, and the team must present a business model with it while describing in detail initial investments to the mass production and investment restoration in different scenarios. It constitutes a total of 75 points.
- **Cost and Manufacturing Event:** In this event, the judges evaluate the understanding of the team of manufacturing processes, its cost, and the overall cost of the car. The team needs to have organised documents such as the Bill of Materials, Detailed Bill of Materials, and Costed Bill of Materials. The team also needs to explain the make-or-buy decisions. This event has a total of 100 points.
- **Engineering Design Event:** In this event, the judges evaluate the good overall engineering knowledge while making design choices and designing the car through the design phase. The team must show good simulations with good validation while exploiting the best of the available resources. The car performance is not evaluated in this event since all that matters is the understanding of the team of its car. It is the most important Static Event, constituting a total of 150 points.

1.2.2.2 Dynamic events

Contrary to the Static Events, the objective of the Dynamic Events is to evaluate the performance of the car in relation to other teams. The Dynamic Events are Skidpad, Driverless Skidpad, Acceleration, Driverless Acceleration, Autocross, Endurance, and Efficiency.

- **Skidpad:** This event evaluates the lateral acceleration of the car. It consists of a track of two circles in an eight shape with an outer diameter of 21.25m and an inner diameter of 15.25m, as shown in Figure 1.1.

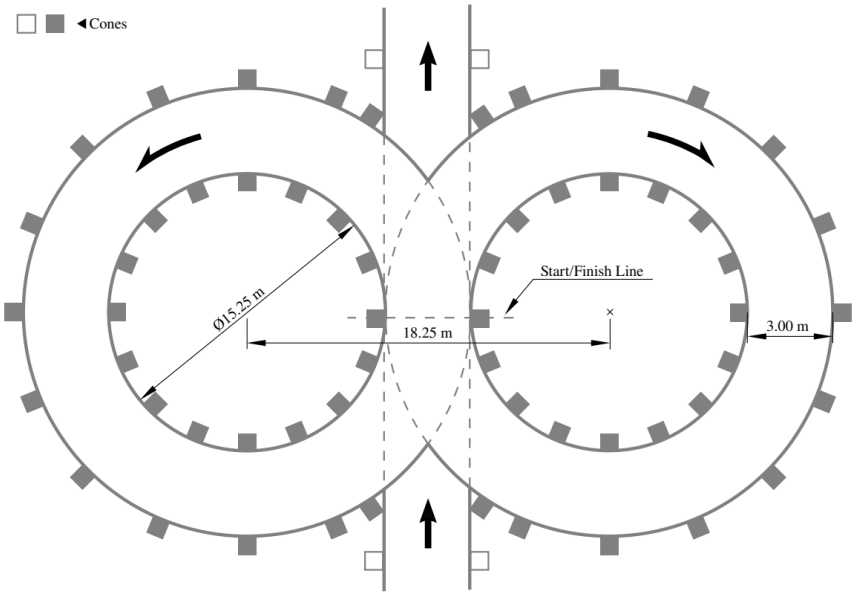

Figure 1.1: Manual and DV Skidpad layout (FSG, 2023a).

The driver must complete two laps in each orientation, and the skidpad time is the average of the best lap for each side. This event has a total of 50 points.

- **DV Skidpad:** Same as Manual Skidpad, but the car runs autonomously. This event constitutes 75 points of the total points.
- **Acceleration:** A 75-meter straight to evaluate the acceleration of the car starting from standstill. The best team is awarded with 50 points.
- **DV Acceleration:** A 75-meter acceleration from a standstill done by the Autonomous System. It awards a total of 75 points.
- **Autocross:** The autocross is a one-lap shootout that serves as an endurance qualifying. The driver does one lap to the endurance circuit, where it is subjected to cornering, straights, and other conditions. It consists of 100 points.
- **Endurance:** During the Endurance Event, the car needs to run a total of twenty-two kilometre divided by two drivers. This is done to test the performance of the car over long runs. Wheel-to-wheel racing is not permitted, making overtaking available only in designated zones. This event awards the most points: a total of 250.
- **Efficiency:** During the Endurance run, the efficiency of the car is also evaluated. The maximum number of points awarded is 75.

1.2.2.3 Points system

There is a total of 1000 points in a competition, distributed around the static and dynamic events. The point distribution is shown in Figure 1.2.

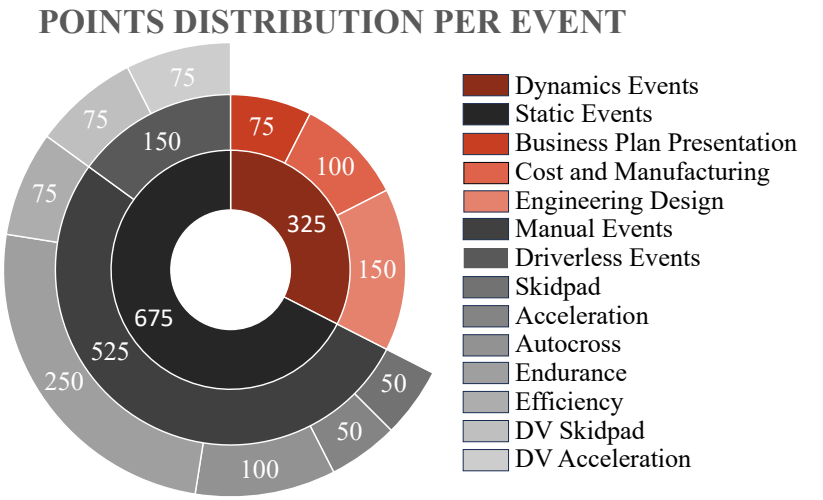

Figure 1.2: Points distribution per event (FSG, 2023a).

1.2.2.4 Technical inspections

In order to compete in the Dynamic Events, there is a list of Technical Inspections that the car must pass. This list is different for CV, EV, and hybrid cars. Since this thesis is for an EV, this part will only focus on EV scrutineering. First, it is necessary to pass through the static scrutineering (FSG, 2023a).

- **Pre-Inspection:** This is the first inspection, and it is where driver's equipment, safety equipment such as fire extinguishers, and rims and tires are checked.
- **Accumulator Inspection:** In this inspection, the scrutineers check if the Tractive System Accumulator (TSA) complies with all specific rules and is safe for everyone involved. The TSA undergoes tests that check if the management systems are correctly operating, such as the Accumulator Management System (AMS), the charging system and the safety components. Also, the Tractive System Accumulator Container (TSAC) is checked to confirm that it is manufactured as stated in the Structural Equivalency Spreadsheet (SES). After passing this inspection, the accumulator is sealed for the rest of the competition, and, in case of the need to open it, the team must go through the inspection sheet again.
- **Electrical Inspection:** In this inspection, the electrical components are all checked. The main objective of this scrutineering is to ensure that the car is electrically safe for all people involved when it is working.
- **Mechanical Inspection:** In this scrutineering, the checks fall on the mechanical systems of the car, mainly on the chassis but also on the suspension and transmission, ensuring that it is safe to run and drive.

After passing the static scrutineering, the car still need to pass the dynamic ones to be able to compete. In these scrutineering, the order is sequential and cannot be changed.

- **Tilt Test:** The first dynamic technical inspection consists of inclining the car up to 60º with the tallest driver in the car, as shown in Figure 1.3. To pass the test, no fluid can leak, and the vehicle must withstand its weight at the initial table position.

Figure 1.3: Tilt test.

- **Vehicle Weighing:** Just to annotate the vehicle weight.

- **Rain Test:** In this test, the car is subjected to a rain simulation to ensure that it remains safe in the event of rain. The car is subjected to a two-minute period of rain followed by a two-minute period without waterfall and needs to remain turned on during the process. To successfully pass the test, it is necessary to create a controlled short circuit in the car, and it needs to be capable of safely turning off. Figure 1.4 shows an example of rain test.

Figure 1.4: Rain test.

- **Brake Test:** The objective of this inspection is to verify if the car can safely stop in case of emergency. The driver needs to accelerate in a straight line from a standstill to reach at least 40km/h and must brake within the designated area of 10 meter. The car must remain in a straight line and must lock all wheels to pass the test.

1.2.3 Formula Student FEUP

Formula Student FEUP (FS FEUP) was created in July 2021 to represent both the University of Porto and the Faculty of Engineering of the University of Porto (FEUP) in the Formula Student competitions.

During the first two years of existence, the team managed to design and manufacture its prototype. It was a two-year project, the first design and the later manufacture. The team competed in 2022 in Formula Student UK Concept Class and Formula SAE® Italy Class 3. Later in 2023, the team managed to compete with the prototype in three competitions: Formula Student UK, Formula Student Portugal, and Formula Student Germany.

Figure 1.5: FS FEUP with it first car in FSG.

For its second car, the team is currently in a two-year project again, with the major objective of competing in Formula Student Germany in 2025. For 2024, the team goal is to compete in Formula Student UK Concept Class and in Formula Student Portugal Class 2, where only static events are evaluated.

1.3 Powertrain of an electric vehicle

When talking about an electric powertrain, there are different components associated:

- **Battery pack:** Responsible for the vehicle energy storage through electrochemical cells;
- **Inverter:** Responsible for the power conversion;

- **Controller:** Responsible for controlling the motor;
- **Motor:** Responsible for the power and torque generation;
- **Transmission:** Responsible for the power and torque transmission to the wheels.

For the scope of this thesis, this topic will be divided into road cars and Formula Student cars.

1.3.1 Road car electric powertrain

When talking about road cars, there are six main powertrain concepts, with only three preferably used by manufacturers due to efficiency (Tie and Tan, 2013).

- **Configuration a)** A configuration that is directly corresponds to the one in an ICE vehicle. This is mainly done when an ICE car is turned into an EV, maintaining the clutch and gearbox, only changing the engine for a battery, inverter and motor (Tie and Tan, 2013);
- **Configuration b)** The clutch is removed, and the gearbox becomes a fixed gear, reducing size and weight in comparison to configuration a) (Tie and Tan, 2013);
- **Configuration c)**This configuration is an improvement from the previous one as it includes the fixed gearing and the differential in the same structure at the car rear(Tie and Tan, 2013);
- **Configuration d)** This configuration uses two motors to improve the power and torque of the vehicle, with a fixed gearing. In this configuration, the differential is removed (Tie and Tan, 2013);
- **Configuration e)** An improvement from the previous configuration as drive-shafts are removed and with the torque and power applied directly in the wheel (Tie and Tan, 2013);
- **Configuration f)** Finally, the last configuration is similar to the previous ones, but the motors are in-wheel, making the packaging more compact (Tie and Tan, 2013).

1.3.2 Formula Student car electric powertrain

The electric powertrain configuration on a FS car depends on the rules, available space, the number of motors, and whether those motors are outboard or inboard.

The front of the car has a small space for a larger inboard motor due to the driver's legs, pedal box, and steering system. This means the only front-wheel drive options available are those with outboard motors.

In terms of rear-wheel drive, both outboard and inboard could be used. Hence, there are four main possible configurations for a Formula Student car:

- **Configuration a)** One inboard motor at the rear of the car. The transmission can be via chain, belt, or gears, with a fixed gear ratio. There is a need for a differential and half-shafts;

- **Configuration b)** Two outboard or inboard motors at the car rear. There is no need for a differential since the two motors can rotate at different speeds during cornering via control. However, it is necessary to have a fixed gear ratio to multiply the torque;
- **Configuration c)** One rear motor and two outboard in-wheel front motors. There is a need for a differential and half-shafts at the rear, and every motor must have a fixed gear ratio;
- **Configuration d)** Four motors, one in each wheel, with a fixed and high gear ratio. This configuration is the better one in performance, although it is challenging to implement the torque vectoring.

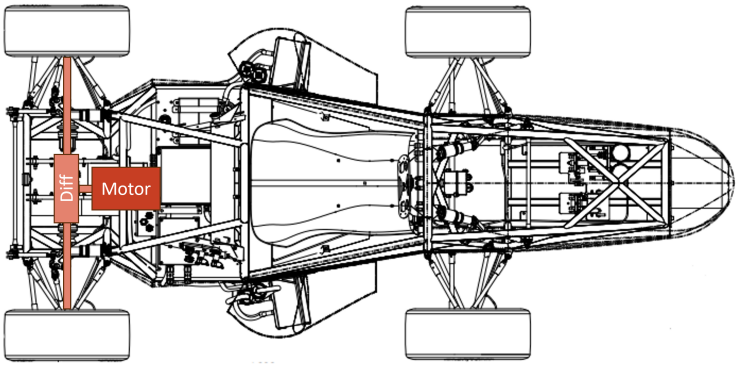

(a)

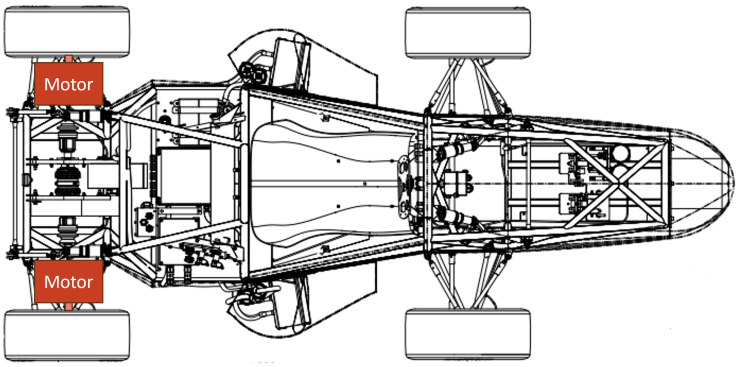

(b)

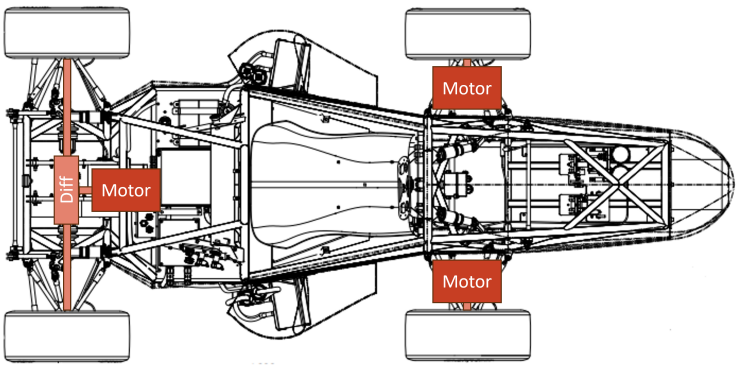

(c)

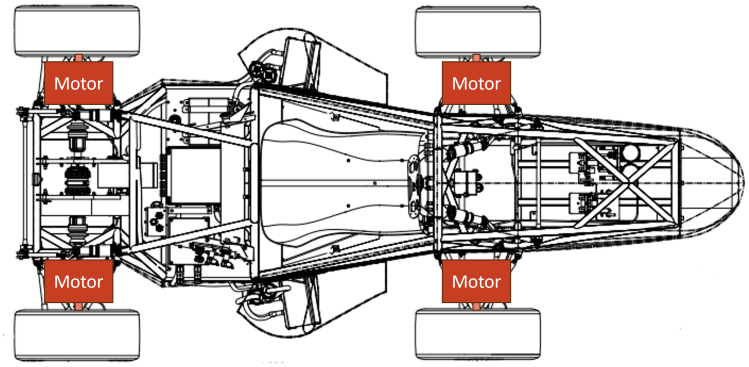

(d)

Figure 1.6: (a) One inboard motor at the rear of the car (configuration a); (b) two outboard or inboard motors at the rear of the car (configuration b); (c) one rear motor and two outboard in-wheel front motors (configuration c); (d) four motors (configuration d).

1.4 Motivation

This thesis as part of the framework of the FS project, with the objective of designing and manufacturing an electric racing car. The battery is the heart of the car, and its assembly is subjected to intense regulation concerning safety and mechanical integrity. Allying this with the need for performance and reduced weight, the objective is to design and manufacture a Tractive System Accumulator Container in composite material to replace the aluminium one present in the first car of the team.

The knowledge acquired in this thesis can also be transposed for road cars and general motorsport, where electrification is becoming increasingly more present. This comes with the need to decrease weight and improve performance and efficiency. Thus, the market is moving towards composite materials instead of traditional steel and aluminium.

1.5 Thesis structure

In this section, the outline of this thesis will be explained, by providing a summary of each chapter.

Chapter 2 consists of a literature review on the state of the art of the area. First, it describes the concept of battery housings and its use both in road cars as well as in motorsport and Formula Student. Then, a small introduction to composite concepts that will be used is done. Finally, a brief explanation of the experimental tests performed and their standards is presented.

In Chapter 3 the weight target is set based on a study done on the FSFEUP 01 car weight distribution, starting with the overall weight and then entering into the the accumulator assembly.

Furthermore, all the constraints whether they are imposed by the components inside the container or the position of it in the chassis are listed.

Chapter 4 presents all the numerical implementations of this work. It starts by presenting the numerical implementation of classical composite theories to a three-point bending test and then it presents all the Finite Element Analysis required for the design of the container, according to the imposed load cases.

Chapter 5 consists of a description of the manufacturing of composite specimens to test and validate the previous numerical implementations. Then, an analysis of the experimental tests and a comparison between the numerical model and the testing results are conducted. Finally, the material properties are also retrieved from the testing data.

In Chapter 6, the container is finally designed having in mind its manufacturability. In this chapter, all the divisions and parts of the container are explained in detail, as well as a brief summary of its manufacturing process.

Finally, Chapter 7 presents the conclusions that can be retrieved from this work and some next steps for the future.

Chapter 2

Literature review

2.1 Battery housings

One of the challenges of EV cars is their autonomy. There are different ways of improving it: increasing the energy capacity or increasing the efficiency of the vehicle. However, doing so would significantly affect the car weight. The other possibility is improving overall efficiency, reducing consumption (Schludi and Joos, 2019).

Reducing the weight can lower the vehicle resistance. All components of the car can lose mass if the design considers the proper materials. The battery housing is not an exception, and composite materials can save weight.

The battery container is a component that protects the electronics and battery cells from outside conditions, like physical impacts, temperature and electromagnetic interferences (Höhne et al., 2023). Furthermore, the housings are responsible for the placement and mounting of the electric battery in the vehicle.

Thus, as stated in Schludi and Joos (2019), lightweight design is insufficient since safety and reliability are also crucial parameters. For this reason, it is necessary to include elements with good "fire safety, rigidity, integrity, thermal management, electromagnetic compatibility and anti-corrosion properties (Schludi and Joos, 2019).

Overall, the market of battery containers is growing. Research and Markets (2021) state that the EV battery housing market generated 0.87 billion dollars, while the expected value for 2025 is 4.47 and a demand of 1167.3 thousand tonnes (Research and Markets, 2021).

2.1.1 Composite battery housings in road cars

With the current demand for high-performance and lightweight automotive parts, the use of composite materials is increasing. Furthermore, the need for flame-retardant and a competitive cost for EV vehicle materials opens the door to substitute metals by structural composites (Mohanty et al., 2023), in alliance with their possible weight-saving potential, corrosion resistance and thermal insulation (Höhne et al., 2023).

Nowadays, the automated moulding process using rapid cure thermoset resins (Schludi and Joos, 2019) ensures the high quality of the fibre components.

The material commonly used is a sandwich structure (Schludi and Joos, 2019), although Sheet moulding compound (SMC) and carbon-fibre SMC (SMC-CF) are also especially suitable for battery housings, as they combine good weight-specific mechanical properties, as well as design freedom (Höhne et al., 2023).

Likewise, composite materials have also a good insulation effect, meaning less energy is needed for thermal regulation, lowering the power consumption and increasing efficiency (Schludi and Joos, 2019).

Furthermore, by using these materials, there is an increase in fire safety. The battery housing materials must be fire retardant according to UL94 V-0 and UL94 5VB. The composite can have additives to boost its fire resistance and comply with this rule (Schludi and Joos, 2019).

CFRP materials have higher stiffness and low weight, which results in "good damping properties" (Schludi and Joos, 2019) and a reduction of noise and vibration.

Different examples of battery enclosures made in composite material are shown in Figure 2.1.

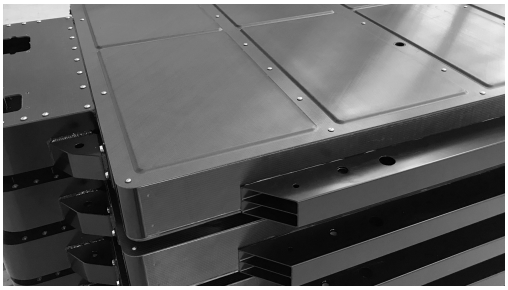

Figure 2.1: Composite material battery enclosures from SGL Carbon (Schludi and Joos, 2019).

2.1.2 Composite battery enclosures in Formula 1

Motorsport is used to develop and test new features and technologies that can improve the daily mobility overall efficiency and performance since racing cars push technology forwards. For these reasons, electrification and composite battery enclosures have already reached the top steps of Motorsport.

Since 2014, Formula 1 has been using a hybrid system composed of a turbocharge internal combustion engine allied with an energy recovery system (Bold Valuable Tech). This system uses two components to generate and store energy in a battery: the Motor Generator Unit Kinetic (MGU-K) and the Motor Generator Unit Heat (MGU-H) (Bold Valuable Tech).

This battery is part of the power unit (PU) and must comply with a considerable set of regulations. It must be inside the monocoque structure and under the fuel tank. In addition, it must weigh between 20 and 25 kg (Bold Valuable Tech).

An inert gas surrounds the cells to avoid water condensation and its subsequent electronic damage, which means the container must be sealed and leak-proof (Bold Valuable Tech).

To comply with the regulations, it is common to use carbon fibre and epoxy prepregs with some electrical insulation layers in between. In addition, it is also important to develop a Faraday cage effect to prevent electromagnetic interference caused by the inverter commutation (Bold Valuable Tech). As part of the PU, the battery enclosure constitutes a structural part of the car.

2.1.3 Composite TSAC in Formula Student

The TSAC in a Formula Student car is an essential security component. It is crucial to have a structure that secures the accumulator in the car during normal functioning and protects it in case of an accident. Thus, the main properties that these containers must have are:

- **Mechanical properties:** The container must withstand accelerations of 40g in the longitudinal and transversal directions and 20g in the vertical one (FSG, 2023a). Thus, it is necessary to have a material with high mechanical properties;
- **Fire resistance:** To contain any fire that starts in the accumulator, all the materials used in the container and structural parts must be fire retardant according to UL94 V-0 or FAR 25.853(a)(1)(i) (FSG, 2023a);
- **Electric conductivity:** As the battery is a dangerous component due to the high voltage and current, the container must be non-conductive to protect everyone involved in the car;
- **Grounding layer:** The rules specify that if conductive materials are used, it is necessary to have an aluminium or better conductive material layer of at least 0.5 mm;
- **Impact resistance:** In the event of an accident, the container must protect the cells from the impact. Thus, it is necessary for the material used to present a good impact resistance.

Choosing a material for the accumulator container is the first crucial step in the overall accumulator concept, as this will impact the structural, cooling and overall packaging size of the whole container. Three materials can be used: steel, aluminium, and composite.

The rules specify the minimum requirements for aluminium and steel, stated in FSG (2023a):

> - *The bottom of the TSAC must be at least 1.25 mm thick if made from steel or 3.2 mm if made from aluminium.*
> - *The internal and external vertical walls, covers, and lids must be at least 0.9 mm thick if made from steel or 2.3 mm if made from aluminium.*
>
> *Alternative materials are allowed with proof of equivalency per T3.3 or for composite materials per EV5.5.5. This must be documented in the SES. When alternative materials are used, test samples must be presented at technical inspection.*

Over the years, the use of composite materials has been rising, as it offers advantages over the use of aluminium and steel. As seen in Figure 2.2, in the last year, more than half the teams used composite materials in the TSAC in FSG.

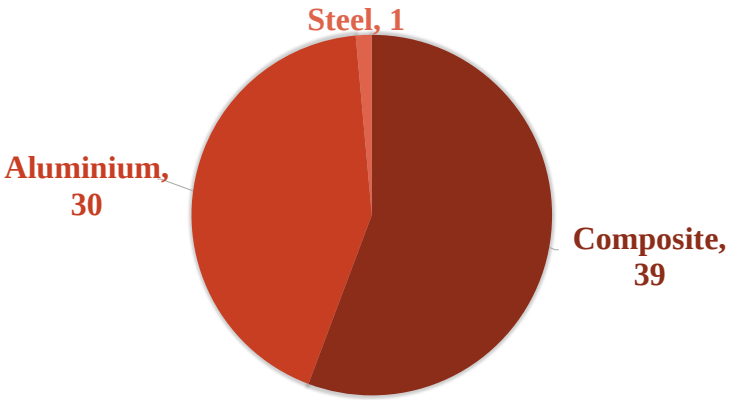

Figure 2.2: Accumulator container material distribution in FSG 2023.

2.2 Aluminium vs Composite containers

Nowadays, metals and metal alloys are still the most used materials. However, with the market evolution, the metal components are being replaced by composite materials that provide cost, performance and manufacturing advantages (Mohanty et al., 2023). In fact, composite materials can reduce the weight of the battery housing by up to 40% compared to aluminium (Schludi and Joos, 2019), while having other advantages.

CFRP components can substitute aluminium without changing the container volume and geometry (Schludi and Joos, 2019). In addition, composite materials have a low thermal conductivity, which is 200 times lower than the aluminium one (Schludi and Joos, 2019), meaning that composite materials housings offer improved protection against outside conditions, a necessary aspect since the lithium-ion cells have an ideal working temperature of 10 to 40°C (Schludi and Joos, 2019).

Schludi and Joos (2019) have tested steel and composite materials to compare the evolution of a surface temperature while exposing the opposite one to a Bunsen burner with a temperature of around 800°C.

The steel reaches approximately 750°C after 30 seconds, the standard thermoset resin epoxy composite reaches 550°C after 60 seconds, and the sandwich structure reaches around 350°C after 180 seconds. Aluminium was not tested since its melting temperature is around 660°C (Schludi and Joos, 2019).

In general, composite housings have the following benefits (Schludi and Joos, 2019): weight saving, increased design freedom, improved fire safety, and corrosion resistance.

Metals show a higher shielding efficiency than composites due to its conductivity and permeability (Höhne et al., 2023). It is possible to produce polymer composites with good shielding by using conductive polymers, a conductive coating or a magnetic filler to bulk up the polymer (S. Kumar et al., 2021). In particular, carbon-based fillers are appropriate for this application since they have good mechanical properties and good conductivity (Höhne et al., 2023).

2.3 Classical Lamination Theory

Jones (1999) defines a laminate as a bonded stack of laminae with various orientations of principal material directions in the laminae. A laminate cross-section example is shown in Figure 2.3.

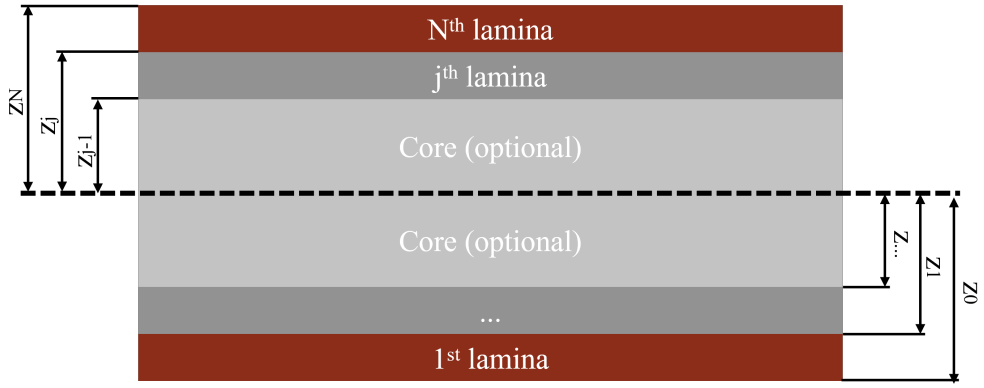

Figure 2.3: Laminate cross-section example.

The Classical Lamination Theory (CLT) is an approach to analytically determine the stress and strain of each ply due to mechanical loads. It assumes the following conditions (Jones, 1999):

- Plane stress state ($\sigma_3 = \tau_{23} = \tau_{31} = 0, \sigma_1 \neq 0, \sigma_2 \neq 0, \tau_{12} \neq 0$);
- Each lamina is orthotropic, homogeneous and elastic;
- The displacements are continuous and small;
- There is no delamination between each lamina.

The external mechanical loads per unit width imposed to the laminate are defined as:

$$[N] = \begin{bmatrix} N_x & N_y & N_s & M_x & M_y & M_s \end{bmatrix}^T \tag{2.1}$$

The stress-strain relation is given by (Jones, 1999):

$$\begin{bmatrix} \sigma_1 \\ \sigma_2 \\ \sigma_3 \end{bmatrix} = \begin{bmatrix} Q_{11} & Q_{12} & 0 \\ Q_{12} & Q_{22} & 0 \\ 0 & 0 & Q_{66} \end{bmatrix} \begin{bmatrix} \varepsilon_1 \\ \varepsilon_2 \\ \gamma_{12} \end{bmatrix} \tag{2.2}$$

where the lamina stiffness matrix components are defined as:

$$
\begin{aligned}
Q_{11} &= \frac{E_1}{1-\nu_{21}\nu 12} \\
Q_{12} &= \frac{\nu_{12}E_2}{1-\nu_{21}\nu 12} \\
Q_{22} &= \frac{E_2}{1-\nu_{21}\nu 12} \\
Q_{66} &= G_{12}
\end{aligned}
\tag{2.3}
$$

where E_1 represents the Young's modulus in the longitudinal direction, [Pa],
E_2 represents the Young's modulus in the transverse direction, [Pa],
G_{12} represents the in-plane shear modulus, [Pa], and
ν_{12} and ν_{21} represent the in-plane Poisson's ratios, [-].

However, the formulae above only provide values for unidirectional plies. Thus, it is necessary to apply a transformation matrix for misaligned plies.

Considering the $m = \cos\theta$ and $n = \sin\theta$, the Q matrix for off-axis plies is determined as (Jones, 1999):

$$
\begin{aligned}
\overline{Q}_{xx} &= Q_{11}m^4 + Q_{22}n^4 + 2(Q_{12} + 2Q_{66})m^2n^2 \\
\overline{Q}_{xy} &= (Q_{11} + Q_{22} - 4Q_{66})m^2n^2 + Q_{12}(m^4 + n^4) \\
\overline{Q}_{yy} &= Q_{11})n^4 + Q_{22}m^4 + 2(Q_{12} + 2Q_{66})m^2n^2 \\
\overline{Q}_{xs} &= (Q_{11} - Q_{12} - 2Q_{66})m^3n - (Q_{22} - Q12 - 2Q_{66})mn^3 \\
\overline{Q}_{ys} &= (Q_{11} - Q_{12} - 2Q_{66})mn^3 - (Q_{22} - Q12 - 2Q_{66})m^3n \\
\overline{Q}_{ss} &= (Q_{11} + Q_{22} - 2Q_{12} - Q_{66})m^2n^2 + Q_{66}(n^4 + m^4)
\end{aligned}
\tag{2.4}
$$

Then, it is necessary to compute the laminate stiffness matrix, **P** (Mallick, 2007):

$$
[P] = \begin{bmatrix} A & B \\ B & D \end{bmatrix}
\tag{2.5}
$$

Where **A**, **B** and **D** are determined as follows (Mallick, 2007):

$$
\begin{aligned}
A_{i,j} &= \sum_{k=1}^{n} \overline{Q}_{i,j}^{(k)} \times (z_k - z_{k-1}) \\
B_{i,j} &= \frac{1}{2}\sum_{k=1}^{n} \overline{Q}_{i,j}^{(k)} \times (z_k^2 - z_{k-1}^2) \\
D_{i,j} &= \frac{1}{3}\sum_{k=1}^{n} \overline{Q}_{i,j}^{(k)} \times (z_k^3 - z_{k-1}^3)
\end{aligned}
\tag{2.6}
$$

Lastly, the deformations can be determined as follows (Mallick, 2007):

$$[\varepsilon] = [P]^{-1}[N] = \begin{bmatrix} \varepsilon_{xx^0} & \varepsilon_{yy^0} & \gamma^0_{xy} & k_{xx} & k_{yy} & k_{xy} \end{bmatrix}^T \tag{2.7}$$

where ε_{xx^0} and ε^0_{yy} are the midplane normal strains,
γ^0_{xy} is the midplane shear strain,
k_{xx} and k_{yy} are the bending curvutures and
k_{xy} is the twisting curvuture.

It should be noted that ε only represents the strain in the laminate midplane. To compute the strain field in each specific lamina, the following equations are used (Mallick, 2007):

$$\begin{aligned} \varepsilon_{xx} &= \varepsilon^0_{xx} + zk_{xx} \\ \varepsilon_{yy} &= \varepsilon^0_{yy} + zk_{yy} \\ \gamma_{xy} &= \gamma^0_{xy} + zk_{xy} \end{aligned} \tag{2.8}$$

where z represents the distance from the midplane in the thickness direction.

Finally, using Equation (2.2), the stresses for each lamina can be computed.

2.3.1 ABD matrices special cases

There are a few special cases with specific laminate lay-ups, such as (Mallick, 2007):

- **Symmetric layups:** B=0;
- **Balanced layups:** $A_{16} = A_{26} = 0$;
- **Anti-Symmetric layups:** $D_{16} = D_{26} = 0$.

2.3.2 Laminate apparent stiffness

The laminate apparent stiffness is the material stiffness when subjected to uniaxial stress. These values and the Poisson's ratio can be determined using the previously defined laminate stiffness matrix (Mallick, 2007).

$$\begin{aligned} E_{xx} &= \frac{A_{11}A_{22} - A_{12}^2}{tA_{22}} \\ E_{yy} &= \frac{A_{11}A_{22} - A_{12}^2}{tA_{11}} \\ \nu_{xy} &= \frac{A_{12}}{A_{22}} \end{aligned} \tag{2.9}$$

where E_{xx} represents the stiffness in the x direction, [Pa],
E_{yy} represents the stiffness in the y direction, [Pa],
ν_{xy} represents the laminate apparent Poisson's ratio, [-], and
t represents the laminate thickness, [mm].

2.4 Failure criteria

With the increasing usage of composite materials, researchers have put their effort into trying to predict their failure. There are many failure criteria based on theoretical and experimental analysis. Some of the classical criteria covered in this work are maximum stress, maximum strain, Tsai-Hill and Tsai-Wu. Note that all these criteria evaluate the composite behaviour at the ply level.

2.4.1 Maximum stress criterion

The maximum stress criterion considers that a lamina fails if its stress is higher than the allowable ones, being it tensile, compression or shear (Jones, 1999). That is, if any of the following inequalities fails to be satisfied, it is consider that the ply also fails.

$$\begin{array}{lll} \sigma_1 < X_t & \sigma_2 < Y_t & \text{(Tensile)} \\ |\sigma_1| < X_c & |\sigma_2| < Y_c & \text{(Compression)} \\ & |\tau_{12}| < S_{12} & \text{(Shear)} \end{array} \tag{2.10}$$

where X_t is the tensile strength in the longitudinal direction, [MPa],
Y_t is the tensile strength in the transverse direction, [MPa],
X_c is the compressive strength in the longitudinal direction, [MPa], and
Y_c is the compressive strength in the transverse direction, [MPa].

2.4.2 Maximum strain criterion

The maximum strain criterion is quite similar to the maximum stress criteria. If the ply strain is higher than the allowable strain value, the ply fails. Thus, the inequalities that constitute this criterion are (Jones, 1999):

$$\begin{array}{lll} \varepsilon_1 < X_t' & \varepsilon_2 < Y_t' & \text{(Tensile)} \\ |\varepsilon_1| < X_c' & |\varepsilon_2| < Y_c' & \text{(Compression)} \\ & |\gamma_{12}| < S_{12}' & \text{(Shear)} \end{array} \tag{2.11}$$

where X_t' is the allowable tensile strain in the longitudinal direction, [-],
Y_t' is the allowable tensile strain in the transverse direction, [-],
X_c' is the allowable compressive strain in the longitudinal direction, [-], and
Y_c' is the allowable compressive strain in the transverse direction, [-].

Assuming linear-elastic behaviour until failure, the maximum allowable strains can be determined by knowing the other material properties, with (Jones, 1999):

$$X_t' = \frac{X_t}{E_1} \qquad Y_t' = \frac{Y_t}{E_2} \qquad X_c' = \frac{X_c}{E_1} \qquad Y_t' = \frac{Y_t}{E_2} \qquad S_{12}' = \frac{S_{12}}{G_{12}} \tag{2.12}$$

2.4.3 Tsai-Hill criterion

One can note that the previous criteria does not consider interaction between modes of failure. Thus, Hill proposed an extension to the Von Mises criterion that was later adapted by Tsai for a lamina, the Tsai-Hill criterion (Jones, 1999).

For an unidirectional lamina in plane stress, the criterion can be defined as (Jones, 1999):

$$\frac{\sigma_1^2}{X^2} - \frac{2\sigma_1\sigma_2}{X^2} + \frac{\sigma_2^2}{Y^2} + \frac{\tau_{12}^2}{S^2} \tag{2.13}$$

where X, Y, and S are equal to the relevant value of X_t, X_c, Y_t, Y_c, and S, respectively, depending on the sign of the in-plane normal stresses.

Although this criterion already accounts for interaction between the failure modes, it was found that it lacked correlation between predicted and experimental values (Jones, 1999).

2.4.4 Tsai-Wu criterion

To overcome the previous problem, Tsai and Wu proposed a solution with additional parameters based on a tensorial form (Jones, 1999):

$$F_i\sigma_i + F_{ij}\sigma_i\sigma_j = 1 \qquad \text{i,j = 1, ..., 6} \tag{2.14}$$

For an orthotropic lamina in plane stress state, Equation (2.14) simplifies to (Jones, 1999):

$$F_1\sigma_1 + F_2\sigma_2 + F_6\sigma_6 + F_{11}\sigma_1^2 + F_{22}\sigma_2^2 + F_{66}\sigma_6^2 + 2F_{12}\sigma_1\sigma_2 = 1 \tag{2.15}$$

where (Jones, 1999):

$$\begin{gathered} F_1 = \frac{1}{X_t} - \frac{1}{X_c} \qquad F_2 = \frac{1}{Y_t} - \frac{1}{Y_c} \qquad F_{12} = -\frac{1}{2}\sqrt{\frac{1}{X_tX_c}\frac{1}{Y_tY_c}} \\ F_{11} = \frac{1}{X_tX_c} \qquad F_{22} = \frac{1}{Y_tY_c} \\ F_6 = \frac{1}{S_{12_t}} - \frac{1}{S_{12_c}} \qquad F_{66} = \frac{1}{S_{12_t}S_{12_c}} \end{gathered} \tag{2.16}$$

2.4.5 Hashin criteria

The Hashin failure criteria, proposed by Hashin in 1980, is valid for unidirectional laminae. It identifies four failure modes: tensile and compressive fibre failure and tensile and compressive matrix failure, as follows:

$$
\begin{gathered}
\text{If } \sigma_{11} > 0 \text{ (Tensile fibre mode)} \\
\left(\frac{\sigma_{11}}{X_t}\right)^2 + \alpha \left(\frac{\tau_{12}}{S_{12}}\right)^2 \geq 1 \\
\text{If } \sigma_{11} < 0 \text{ (Compressive fibre mode)} \\
\left(\frac{\sigma_{11}}{X_c}\right)^2 \geq 1 \\
\text{If } \sigma_{22} > 0 \text{ (Tensile matrix mode)} \\
\left(\frac{\sigma_{22}}{Y_t}\right)^2 + \alpha \left(\frac{\tau_{12}}{S_{12}}\right)^2 \geq 1 \\
\text{If } \sigma_{22} < 0 \text{ (Compressive matrix mode)} \\
\left(\frac{\sigma_{22}}{2S_{23}}\right)^2 + \left(\frac{Y_t}{2S_{23}}\right)^2 - \frac{\sigma_{22}}{Y_c} + \left(\frac{\tau_{12}}{S_{12}}\right)^2 \geq 1
\end{gathered}
\tag{2.17}
$$

2.4.6 Other criteria

Although the classical failure criteria offer a simple and fast way to verify and predict composite failure, it is known that they fail to fully represent what happens in real composite behaviour. Therefore, alternative failure criteria, such as Puck and more recent three-dimensional (3D) criteria, are often used for more detailed design stages.

The Puck failure criterion separates the failure mechanisms into two domains - inter-fibre failure and fibre failure. Inter-fibre failure can then be divided into 3 modes, transverse tensile stress (mode A), low transverse compressive and high shear stress (mode B) and low shear stress (mode C). Inter-fibre failure is matrix dominated. On the other hand, fibre failure occurs in the reinforcement fibres (Puck and Schürmann, 2002). This failure criteria have per basis for the matrix transverse cracking a modified Mohr/Coloumb theory for brittle transversely-isotropic materials.

This model incorporates the same material strength parameters as the classical ones, such as longitudinal tensile and compressive strengths, transverse tensile and compressive strengths, and shear strengths. This failure criterion provides a thorough approach to understanding composite failure, taking into account the different material behaviours, while being possible to identify failure modes.

Recently, Catalanotti et al. (2013) proposed an improved 3D failure criteria derived from Puck criterion, in order to account for general stress states more consistently. This model predicts not only the onset of ply damage, but also information regarding the type of failure and the fracture plane orientation under general 3D stress states.

In recent works, Camanho et al. (2015) proposed a 3D failure criteria with a quadratic formulation based on structural tensors. By doing so, the anisotropy is not modelled by using symmetry conditions but by the structural tensors, leading to a coordinate system-free formulation. These criteria were thoroughly validated with recourse to experimental data and computational micromechanics.

2.5 First vs Last ply failure

There are different ways to consider that a laminate failed. One can consider that the laminate fails when the first ply fails - first ply failure (FPF) - or only when the last ply fails - last ply failure (LPF). While the first option leads to conservative models, as this does not happen in reality, the latter induces complexity in the model, by adding damage algorithms to the models. There are different ways to introduce damage into the models, tested experimentally. In most of them, the damage introduction is achieved by degrading the ply-level properties of the failed lamina. While some models degrade both stiffness and Poisson's ratio, other models only consider degradation of the ply stiffness, as follows (Melo et al., 2011):

$$\begin{aligned} E_1^d &= d_1 E_1 \\ E_2^d &= d_2 E_2 \\ G_{12}^d &= d_6 G_{12} \end{aligned} \tag{2.18}$$

where the superscript d identifies the degraded properties.

Different models have different degrading constants. A simpler analysis considers that the failed ply does not contribute to the laminate stiffness ($d_1 = d_2 = d_6 = 0$). However, it was found that the results fell short of reality and constituted a conservative model (Melo et al., 2011).

There are also different ways of considering residual stiffness, such as simpler analysis as considering $d_1 = d_2 = d_6$ and equal to a constant such as 0.1 or more complex models that consider the different modes of failure of the ply. For the latter, the degrading constants were defined experimentally as (Melo et al., 2011):

$$d_1^T = 0.07 \quad d_2^T = d_6^T = 0.2 \quad d_2^C = 0.14 \quad d_2^C = d_6^C = 0.4 \tag{2.19}$$

Using the Hashin failure criterion, the stiffness degradation can be done as (Melo et al., 2011):

$$\begin{gathered} \text{Fibre tensile fracture: } E_1^d = d_1^T E_1 \\ \text{Fibre compressive fracture: } E_1^d = d_1^C E_1 \\ \text{Matrix tensile or shear cracking: } E_2^d = d_2^T E_2 \; ; \; G_{12}^d = d_6^T G_{12} \\ \text{Matrix compressive or shear cracking: } E_2^d = d_2^C E_2 \; ; \; G_{12}^d = d_6^C G_{12} \end{gathered} \tag{2.20}$$

2.6 Composites characterisation for battery containers

2.6.1 Tensile testing

When it comes to tensile testing, the main objectives are to measure the material ultimate tensile strength, ultimate tensile strain, tensile chord modulus of elasticity, Poisson's ratio, and transition strain (ASTM International, 2008). There are four main standards for tensile tests of composite materials: ASTM D3039, ISO 527, BS 2782 and CRAG 300-302. Typically, the ASTM D3039

standard is the most used to characterise the material, as Beigpour et al. (2021) used to characterise a biodegradable hybrid composite and Sulardjaka et al. (2022) for the characterisation of an unidirectional composite.

2.6.1.1 Specimen geometry

The ASTM D3039 standard specifies the specimen geometry and dimensions for unidirectional (0° or 90° plies) and multidirectional composites. The specimen geometry is shown in Figure 2.4, while Table 2.1 contains its dimensions for multidirectional specimens.

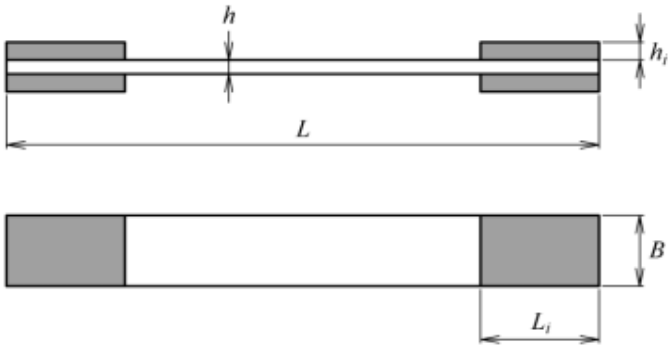

Figure 2.4: Schematic representation of a tensile test specimen.

Table 2.1: Dimensions for the specimen in Figure 2.4.

Dimension	Value [mm]
L	250
B	25
h	2.5
L_i	-
h_i	-

By doing this test, one wants to obtain the material ultimate tensile strength, ultimate tensile strain, modulus of elasticity, Poisson's ratio and tensile failure mode.

2.6.1.2 Ultimate tensile strength

The material tensile stress, σ, during the test is equal to the quotient between the force applied, F, and the average specimen area, A, as shown in Equation (2.21).

$$\sigma = \frac{F}{A} \tag{2.21}$$

The maximum stress the specimen suffers during the test is defined as the ultimate tensile strength, σ_{UTS}, and occurs when the specimen fails. Thus, this strength can be computed as follows:

$$\sigma_{UTS} = \frac{F_{max}}{A} \tag{2.22}$$

2.6.1.3 Ultimate tensile strain

On the other hand, the material also suffers a tensile strain until it fails. During the test, the strain, ε, is equal to the ratio between the displacement, Δl and the initial gauge length of the specimen, l_0.

$$\varepsilon_U = \frac{\Delta_l}{l_0} \tag{2.23}$$

The ultimate tensile strain, ε_U is the strain value at material failure.

2.6.1.4 Tensile Modulus

The tensile modulus is equal the chord slope over a strain range of 0.1 to 0.3%, defined as:

$$E = \frac{\sigma_{0.3} - \sigma_{0.1}}{\varepsilon_{0.3} - \varepsilon_{0.1}} \tag{2.24}$$

2.6.1.5 Poisson's ratio

The Poisson's ratio is the relation between the transverse strain, ε_T, and the axial strain, ε_L.

$$\nu = -\frac{\varepsilon_t}{\varepsilon_L} \tag{2.25}$$

2.6.1.6 Failure mode

In tensile tests, the specimen can fail following different failure modes. ASTM D3039 describes these modes as follows (ASTM International, 2007):

- Inside grip/tab (LIT);
- Tab debonding (GAT);
- At grip/tab (LAT);
- Free edge delamination (DGM);
- Gauge failure (LGM);
- Longitudinal splitting (SGM);
- Angled gauge failure (AGM) (1);
- Angled gauge failure (AGM) (2);
- Explosive (XGM).

2.6.2 Three-point bending

As stated in Section 2.1.3, it is necessary to prove the equivalency of the composite material to the steel and aluminium baseline via three-point bending.

The three-point bending (3PB) test defines the flexural stiffness and strength properties of polymer matrix composites (ASTM International, 2015). There are several standards for different beams, but the most common for long ones is ASTM D7264, as used by Hu et al. (2023) to determine the thickness effect of the specimen on its flexural strength.

2.6.2.1 Specimen geometry

The specimen geometry, in this case, depends on two different things: the standard and the FSG rules.

The standard recommends the following dimensions (ASTM International, 2015):

Table 2.2: Dimensions for the specimen according to ASTM D7264 recommendations (ASTM International, 2015).

Dimension	**Value [mm]**
Span-to-thickness ratio	32:1
Thickness	4
Width	13
Length	20% longer than the span

However, in some tests, these recommendations are not possible to follow. Thus, the standard also has alternate dimensions to considering these cases. The material thickness can be different from 4 mm, but one should try to maintain the span-to-thickness ratio, if possible (ASTM International, 2015). Nonetheless, there are other optimal ratios given by ASTM D7264, such as 16:1, 20:1, and 60:1 (ASTM International, 2015).

As for FSG rules, it is mandatory that the panel measures 150 mm x 275 mm (FSG, 2023a).

2.6.2.2 Test setup

The test setup consists of two simple supports under the specimen at equal pre-determined lengths from the specimen centre while a third roll induces the force. Note that all the rolls have a radius of 3 mm.

2.6.2.3 Force vs displacement curves

To better comprehend the three-point bending, let's consider the following case:

For this scenario, the maximum displacement, v_{max} will occur at the centre of the beam and it is equal to (Fenner and Reddy, 2012):

$$v_{max} = -\frac{FL^3}{48EI} \tag{2.26}$$

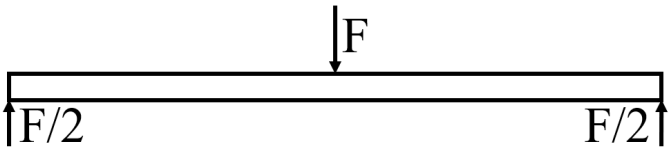

Figure 2.5: Three-point bending case approximation.

where $EI = E_{xx}I$.

To properly show the material equivalency to the rules baseline, it is necessary to determine the flexural strength and flexural modulus. Besides that, it is also possible to retrieve the maximum strain at failure (ASTM International, 2015).

2.6.2.4 Ultimate flexural strength

The flexural stress, σ_f in MPa, the material supports is a function of the load, support span, and the specimen geometry and can be determined as:

$$\sigma_f = \frac{Plt}{8I} \tag{2.27}$$

where P is the load [N],
l is the support span [mm]
t is the specimen thickness [mm], and
I is the specimen second moment of area [mm^4].

Since I can be determined as $I = \frac{bt^3}{12}$, where b is the specimen width in mm, the stress formula come as (ASTM International, 2015):

$$\sigma_f = \frac{3Pl}{2bt^2} \tag{2.28}$$

The ultimate flexural strength is equal to the stress when the maxiumum load, P_{max}, is applied.

2.6.2.5 Flexural modulus

The flexural secant modulus of Elasticity corresponds to the stress-strain ratio in the elastic zone. It can be determined as (ASTM International, 2015):

$$E = \frac{l^3 m}{48I} = \frac{l^3 m}{4bt^3} \tag{2.29}$$

where E is the flexural modulus [MPa],
l is the support span dimension [mm]
t is the specimen thickness [mm],
I is the specimen second moment of area [mm^4],
b is the specimen width, [mm], and
m is the slope of the secant of the force-deflection curve, [-].

2.6.2.6 Maximum strain at failure

The standard considers that the maximum strain at the outer surface occurs in the mid-span and can be determined as (ASTM International, 2015):

$$\varepsilon_{max} = \frac{6\delta t}{l^2} \tag{2.30}$$

where ε_{max} is the maximum strain [-],
l is the support span dimension [mm]
t is the specimen thickness [mm], and
δ is the mid-span vertical displacement [mm].

2.6.3 Four-point bending

In addition to the three-point bending, the four-point bending (4PB) test also allows one to determine the material flexural modulus and strength (ASTM International, 2015). This test also follows ASTM D7264.

2.6.3.1 Specimen geometry

The standard specimen geometry for the four-point bending test is equal to the one previously defined for the three-point bending, in Subsection 2.6.2.1 (ASTM International, 2015). Note that, as the FSG rules do not demand four-point bending testing, there are no contraints imposed by it.

2.6.3.2 Test setup

A representation of the test is shown in Figure 2.6. Note that instead of applying the force at the mid-span, the force is distributed by 2 rolls. Again, all the rolls have a radius of 3 mm.

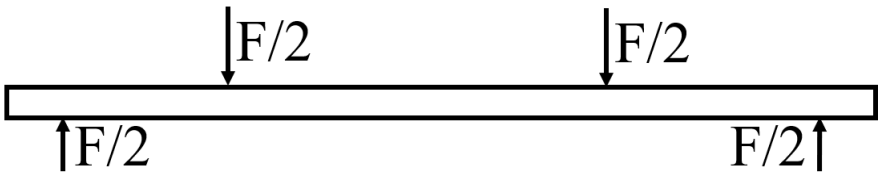

Figure 2.6: 4PB test setup representation.

2.6.3.3 Ultimate flexural strength

The flexural stress, σ_f in MPa, of the material supports is a function of the load, support span, and the specimen geometry and can be determined as:

$$\sigma_f = \frac{Pl}{bt^2} \tag{2.31}$$

where P is the load applied [N],

l is the support span dimension [mm]
t is the specimen thickness [mm], and
b is the specimen width [mm].

The ultimate flexural strength is equal to the stress when the maxiumum load, P_{max}, is applied.

2.6.3.4 Flexural modulus

The flexural secant modulus of Elasticity corresponds to the stress-strain ratio in the elastic zone. It can be determined, for four-point bending, as (ASTM International, 2015):

$$E = \frac{0.17l^3m}{bt^3} \tag{2.32}$$

2.6.3.5 Maximum strain at failure

The standard considers that the maximum strain at the outer surface occurs also in the mid-span and can be determined as (ASTM International, 2015):

$$\varepsilon_{max} = \frac{4.36\delta t}{l^2} \tag{2.33}$$

where ε_{max} is the maximum strain [-],
l is the support span dimension [mm]
t is the specimen thickness [mm], and
δ is the mid-span vertical displacement [mm].

2.6.4 Perimeter shear strength testing

Besides the three-point bending test, the FSG rules also demand a perimeter shear test to show the equivalency of the composite material. This test determines the material shear strength by punching a hole through the specimen. The followed standard is ASTM D732, as used by (Formisano et al., 2017) to define the out-of-plane shear behaviour of GFRP composites.

2.6.4.1 Specimen geometry

As in three-point bending, the specimen geometry and dimensions are influenced by the standard and FSG rules.

Following the standard, the specimen consists of a 50 mm square or 50 mm diameter plate with a thickness between 1.27 mm and 12.7 mm. Furthermore, the plate must have a centre hole of approximately 11 mm (ASTM International, 2017).

According to the FSG rules for material proof of equivalency, the specimen must be a minimum of 100 $\times$ 100 mm (FSG, 2023a).

2.6.4.2 Shear strength

The perimeter shear strength test allows the definition of the material shear strength using the following equation:

$$\sigma_s = \frac{P_max}{\pi D t_1} \tag{2.34}$$

where σ_s is the material shear strength [MPa],
P_{max} is the maximum load [N],
D is the extruder diameter [mm], and
t_1 is the upper skin thickness [mm].

Chapter 3

Targets and constraints

To design a component for a race car, the targets and constraints, such as performance or packaging, should be properly defined. It is crucial to keep in mind that one change in the TSAC to improve its design can have consequences for the rest of the car. Thus, in this chapter, the targets and constraints that apply to the TSAC design will be explained.

3.1 Weight

Weight heavily affects the performance of race cars. As said before, the weight directly affects its energy consumption. In Formula Student, the maximum distance that a car competes in one run is 22 km, meaning that the accumulator energy should match it. This condition opens a loophole that if the weight increases, the energy available must be increased. To boost the available energy, more cells are required, thus increasing the weight.

All teams focus on reducing the weight of the car to the minimum. Figure 3.1 shows the weight distribution per team in FSG 2023.

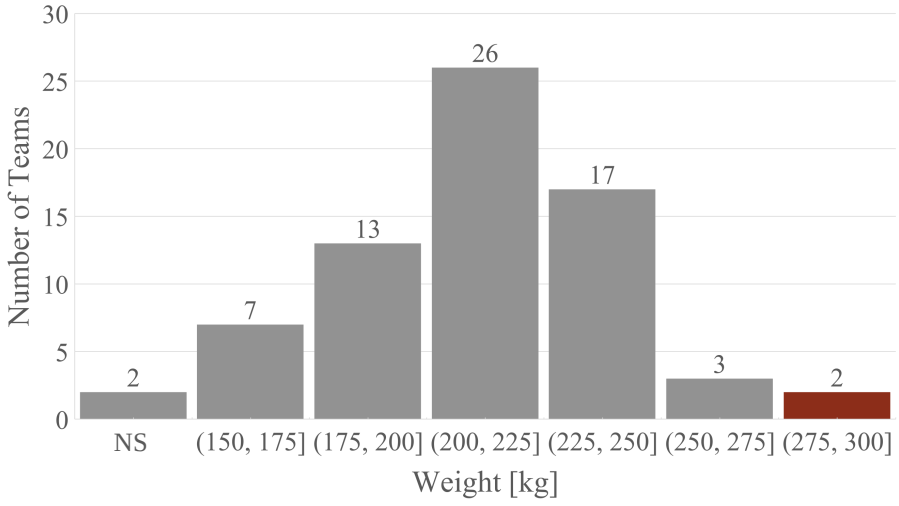

Figure 3.1: Car weight distribution by team in FSG 2023.

According to Figure 3.1, most cars weighed between 200 and 250 kg, with an average weight of 212.9 kg. This average is significantly lower than the weight of the FS FEUP 01 car, which is 277.5 kg. Furthermore, the team first prototype was the second heavier car in the competition. The minimum weight was 162 kg.

Given these results, the team set the objective of decreasing the safety factors used, therefore lowering the weight. The first car was heavier than usual since it was the team first prototype, and the main objective was to make it rule-compliant and reliable, resulting in inflated safety factors due to a lack of confidence and experimental tests on the components. Thus, some components were overly dimensioned and heavy. The weight distribution is shown in Figure 3.2.

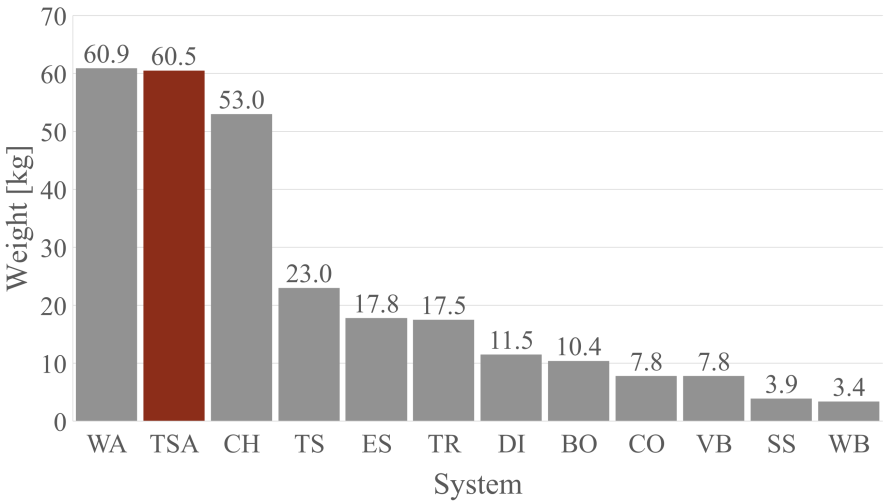

Figure 3.2: FSFEUP 01 weight distribution.

The acronyms used in the graph in Figure 3.2. are listed in Table 3.1.

Table 3.1: Legend for the Histogram in Figure 3.2.

Acronym	**Subsystem**
WA	Wheel Assembly
TSA	Tractive System Accumulator
CH	Chassis
TS	Tractive System
ES	Electric Systems
TR	Transmission
DI	Driver's Interface
CO	Cooling System
VB	Vibrations
SS	Steering System
WB	Wishbones

As seen, the Tractive System Accumulator constitutes a heavy component of the car, and must be reduced. It is necessary to break down the weight per component to define the weight target for

the TSAC, as shown in Figure 3.3.

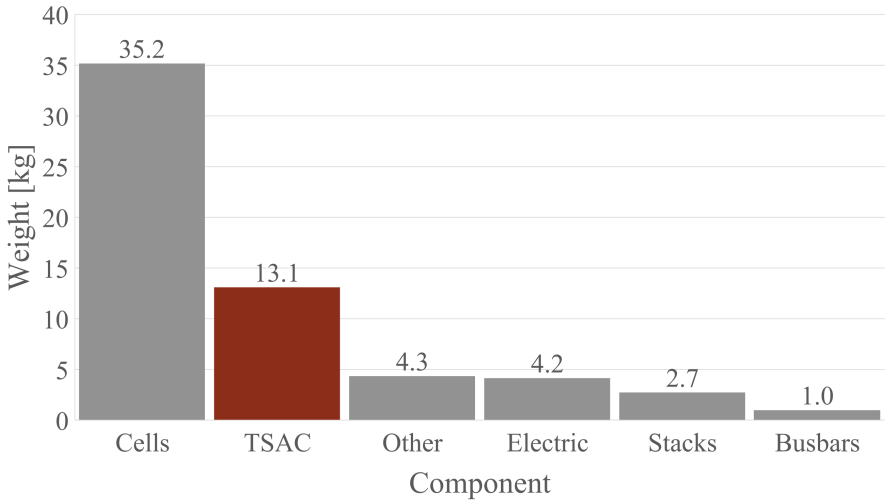

Figure 3.3: Weight of the FSFEUP first car accumulator.

In "Other", it is considered components that by themselves do not represent a considerable weight of the TSA but, when combined, represent a significant one. This division contains 3D-printed components, cables, aluminium placers for other parts, fans for cooling and some electric cable connectors.

Apart from the cells, the TSAC is the heaviest component and where one can reduce most weight. Having per basis that a composite container can reduce the weight up to 40%, the weight objective of the TSAC is set to 7.5 kg.

3.2 Position and dimensions

During the car design, it is essential to consider parameters such as front/rear weight distribution and centre of gravity height. Being one of the most heavy components, the position of the TSA in the car has a significant impact on the prototype dynamic behaviour.

The objective for the team second prototype is to achieve a weight distribution of 45% on the front and 55% on the rear. In terms of the centre of gravity, the objective was set to between 230 mm and 240 mm.

Furthermore, the TSA position should have good accessibility, not only when inside the car but also to remove it from the car. During testing and competitions, it is necessary to remove the TSA from the prototype numerous times, whether for scrutineering, charging or debugging. Thus, it is crucial to have an easy and accessible way to disconnect the accumulator from the rest of the car and extract it.

For these reasons, one can think about placing the TSA under the floor as a commercial vehicle, but that would result in a higher position for the driver. Since the driver is most likely heavier than the TSA, this position is not suitable. Thus, the most appropriate position is the car rear. However,

the transmission components occupied this region of the prototype. Thus, the accumulator is between the driver and the transmission components, as shown in Figure 3.4.

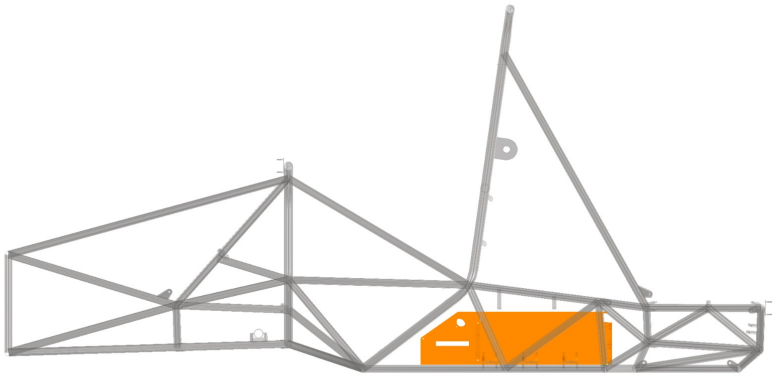

Figure 3.4: Accumulator position in the car.

In terms of dimensions, the Chassis department of the FS FEUP team imposed a maximum width of 550 mm. Although the length and height are not specified, one should consider the constraints discussed previously and try to keep every dimension to the minimum possible.

3.3 Contained components

Besides the energy storage cells, some control and safety electrical components must be placed inside the TSAC.

The cells are divided into six segments that protect and place the cells inside TSAC. In addition, these segments contain all the voltage taps and temperature sensors for voltage and temperature readings, respectively, and the printed circuit board that collects and transmit the information. Figure 3.5 shows a representation of one segment.

Besides the cells, different components must be placed inside the TSAC, separated from the segments referred to above, such as:

- One fuse;
- Two accumulator isolation relays;
- One battery management system;
- One insulation measurement device;
- Four control PCBs.

Figure 3.6 shows an accumulator representation.

Note that there are two different connectors placed in the side walls. These connectors are off-the-shelf components that allow low and high-voltage connections while guaranteeing water-tightness.

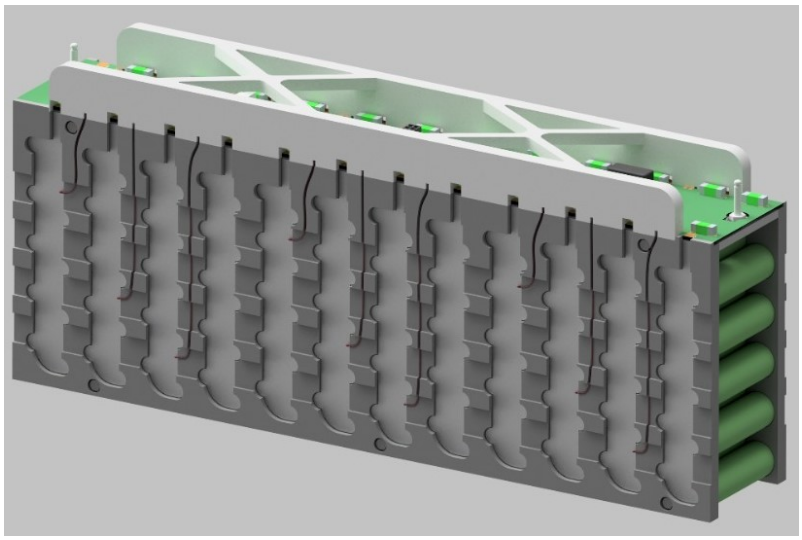

Figure 3.5: Cell segment.

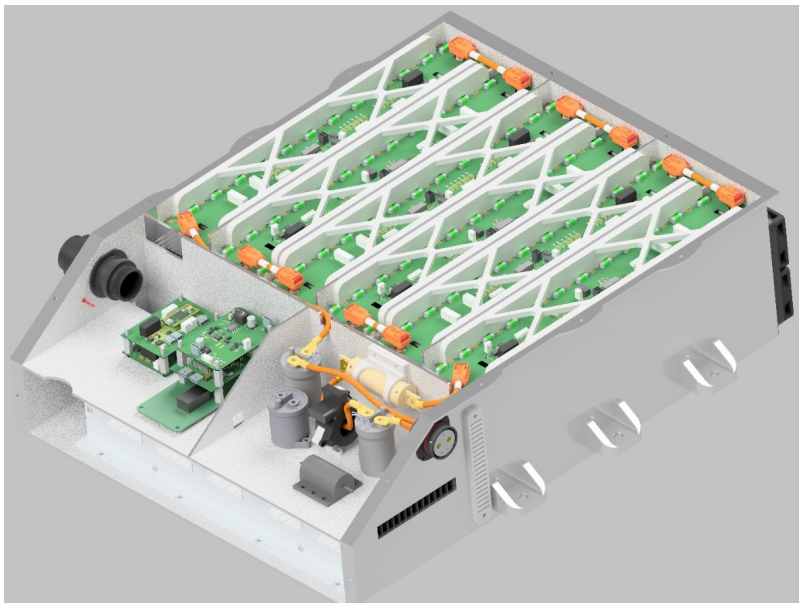

Figure 3.6: Accumulator representation.

3.4 Material

The material choice must consider the constraints and objectives of the component. There are three major properties to comply with structural, grounding, and electrical insulation, keeping in mind its fire compliance. The possible candidates are carbon fibre (CFRP), kevlar fibre, or glass fibre reinforced polymers (GFRP).

CFRP offers the best strength-to-weight ratio of the three, although it induces more complexity in the design. Although carbon fibre has some conductive properties, it is not good enough to be considered a conductive material by the rules. However, its conductivity is not small enough to be considered an insulation material.

Using kevlar or glass fibre solves this problem, as both are electrical insulators. However, kevlar leads to difficulties in manufacturing and the strength-to-weight of GFRP is very low.

Thus, a CFRP pre-preg from Toray was chosen to comply with the structural requirements of the container. To comply with the grounding rule, the outside of the container is covered with 0.5 mm-thicked aluminium. For the inside electrical insulation, both kevlar and GFRP can be used. This material should also be pre-preg and the resin should be the same as the CFRP. After a market search, it was concluded that it was difficult to have a kevlar epoxy pre-preg that comply with the fire retardancy rules. Thus, the insulation material chosen was a GFRP pre-preg with UL94 V-0 certification.

Chapter 4

Numerical implementations

To better choose the optimum laminate layups to test, numerical models having per basis the classical understanding of composite materials were done to simulate and model the experimental tests to realise. This allows one to save time and money when preparing the tests. It is important to note that there are two main material models of whether the composite laminate exhibits a honeycomb core or not.

This chapter will explain the models and their validation in detail. All the codes used are presented in the Appendix A.

4.1 Three-point bending test

It was done a fully analytical model using Python to simulate the three-point bending test using displacement control due to its load case simplicity and simplifications that can be assumed. The validation process used the Altair software ESAcomp.

The model consists of an iterative loop that controls the displacement and analysis of the stresses and strains in the specimen middle through its thickness. To evaluate the laminate failure, different failure criteria were used until all plies failed. An LPF model is used by degrading the plies that have failed. The model flowchart is shown in Figure 4.1.

4.1.1 User input

The model is fully automated to test different laminates without the user changing the properties individually. The entry variables of the model must be stored in text files, one for each laminate, with the following information:

- Plies number;
- Plies orientation;
- Plies thickness;
- Ply elastic properties (E_1, E_2, G_{12} and ν_{12});

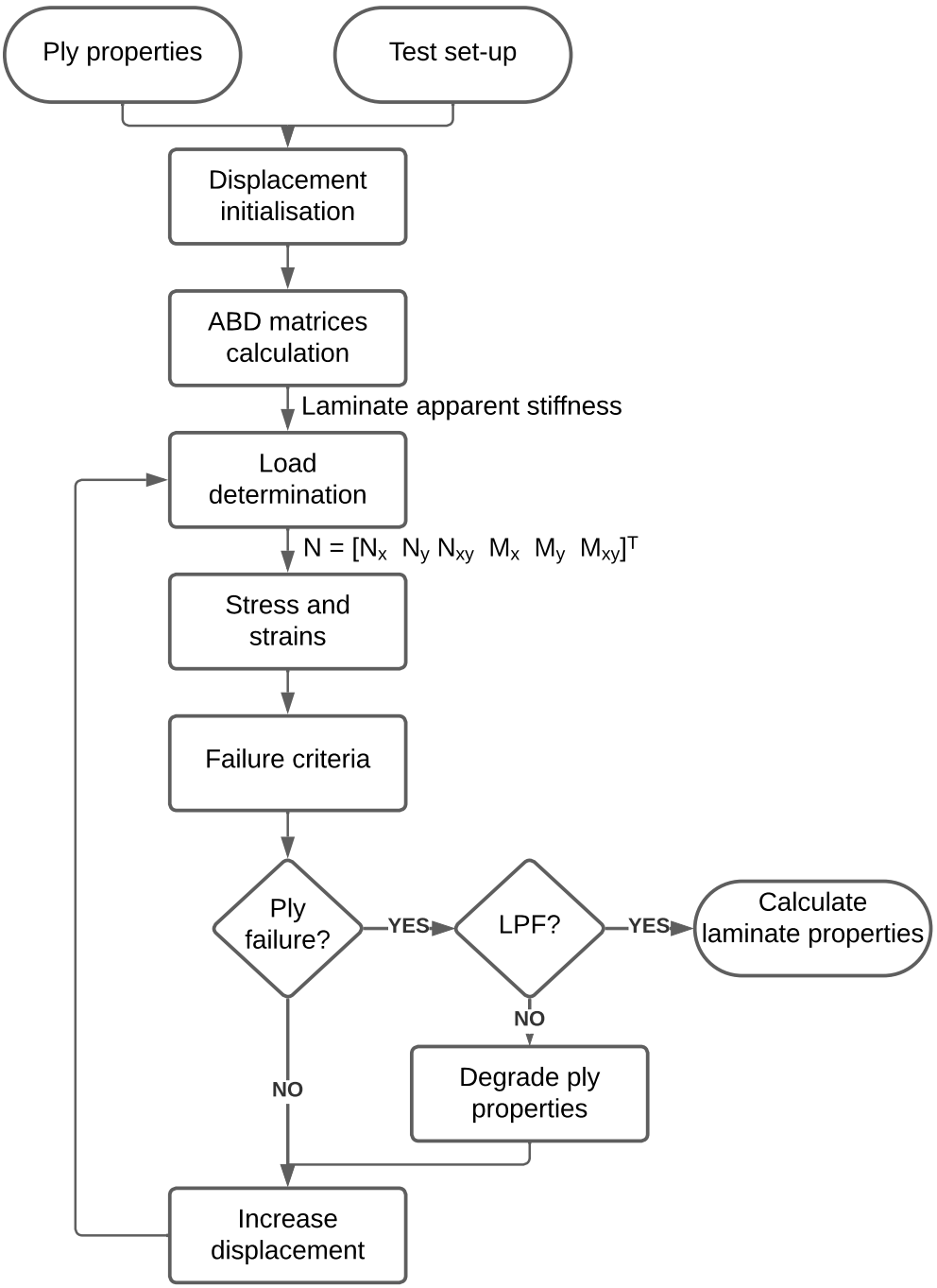

Figure 4.1: Three-point bending model flowchart.

- Ply first ply failure properties (X_t, X_c, Y_t, Y_c, S_{12});
- Test set-up dimensions (span, L, and specimen width, b).

Note that to use laminates with two or more different materials, the ply thickness and properties must be given ply-by-ply. The code determines the laminate thickness and the maximum allowable strain automatically.

4.1.2 CLT implementation

The first step of the analysis of any displacement is to apply the CLT to obtain the stress and strains at the ply level.

The first step is to calculate the laminate stiffness matrices A, B, and D, as explained in Section 2.3. Then, the apparent laminate stiffness is computed using Equation (2.9) to determine the equivalent load, P, associated with the imposed displacement. By re-arraging Equation (2.26), P can be determined as:

$$P = -\frac{48 E_{xx} I v_{max}}{L^3} \tag{4.1}$$

Then, it is necessary to compute the external loads per unit width, N/mm. In a three-point bending situation, the midplane is only subjected to bending loads, that can be determined resorting to beam analysis. Thus:

$$\begin{gathered} N_x = N_y = N_{xy} = M_y = M_{xy} = 0 \\ M_x = \frac{PL}{4b} \end{gathered} \tag{4.2}$$

Determining the loads, it is then possible to apply Equations (2.7) and (2.8) to calculate the ply strains. After that, it is possible to compute the stress field at the ply level for all plies, using Equation (2.2).

4.1.3 Failure criteria

After applying the CLT, the user can choose between the maximum stress, maximum strain, Tsai-Hill, Tsai-Wu and an adapted version of Hashin failure criteria to predict composite failure. The implemented code is an LPF model, and the code will run until all plies have failed.

Since the pre-preg used for the validation and manufacturing of the container is woven, the Hashin criterion could not be used directly. Instead, an adapted version of the criteria was used. A woven has fibres in 1 and 2 directions, thus, rather than considering matrix cracking when talking about the stresses and strains in direction 2, one considered the following four cases:

$$\begin{gathered}
\text{If } \sigma_{11} > 0 \text{ (Tensile fibre failure in direction 1 fibres)} \\
\left(\frac{\sigma_{11}}{X_t}\right)^2 + \alpha_t \left(\frac{\tau_{12}}{S_{12}}\right)^2 \geq 1 \\
\text{If } \sigma_{11} < 0 \text{ (Compressive fibre failure in direction 1 fibres)} \\
\left(\frac{\sigma_{11}}{X_c}\right)^2 + \alpha_c \left(\frac{\tau_{12}}{S_{12}}\right)^2 \geq 1 \\
\text{If } \sigma_{22} > 0 \text{ (Tensile fibre failure in direction 2 fibres)} \\
\left(\frac{\sigma_{22}}{Y_t}\right)^2 + \alpha_t \left(\frac{\tau_{12}}{S_{12}}\right)^2 \geq 1 \\
\text{If } \sigma_{22} < 0 \text{ (Compressive fibre failure in direction 2 fibres)} \\
\left(\frac{\sigma_{22}}{Y_c}\right)^2 + \alpha_c \left(\frac{\tau_{12}}{S_{12}}\right)^2 \geq 1
\end{gathered} \tag{4.3}$$

Note that the contribution of the shear loading can also be changed for tensile and compression cases.

4.1.4 Stiffness degradation

For the last ply failure, it was necessary to use a stiffness degradation model. However, due to the nature of the failure criteria used, the more complex model cannot be used across all the code. For example, for the maximum stress and maximum strain, Tsai-Hill and Tsai-Wu criteria, it is not possible to identify the mode of failure. Thus, it is only possible to apply a constant degradation model. However, for the adapted Hashin criterion, it is possible to identify in which direction the lamina failed and if it was tensile or compression failure.

Thus, for the first case:

$$E_1^d = dE_1 \; ; \; E_2^d = dE_2 \; ; \; G_{12}^d = dG_{12} \tag{4.4}$$

For the latter:

$$\begin{gathered}
\text{Tensile fibre failure in direction 1 fibres: } E_1^d = d_1^T E_1 \\
\text{Compressive fibre failure in direction 1 fibres : } E_1^d = d_1^C E_1 \\
\text{Tensile fibre failure in direction 2 fibres : } E_2^d = d_2^T E_2 \; ; \; G_{12}^d = d_6^T G_{12} \\
\text{Compressive fibre failure in direction 2 fibres: } E_2^d = d_2^C E_2 \; ; \; G_{12}^d = d_6^C G_{12}
\end{gathered} \tag{4.5}$$

These parameters will be further studied in the Validation chapter.

4.1.5 Output

The model automatically returns the laminate ultimate flexural strength and flexural modulus, resorting to Equations (2.28) and (2.29), respectively.

In addition, the force-displacement curves for all specimens tested are stored both in images and text files.

4.1.6 Model validation

Four laminates were tested to validate the code, part by part: two symmetric laminates, one with the same material (S1) and one with two different materials (S2), one balanced (S3) and one anti-symmetric (S4), with the following layups and properties:

- **S1:** $[0/45/-45/90]_S$
- **S2:** $[0a/0b/90b/90a]_S$
- **S3:** [-45/45/0/0]
- **S4:** [0/-45/45/0]

Table 4.1: Material elastic properties used for validation.

Material	**Ply thickness [mm]**	**E_1 [GPa]**	**E_2 [GPa]**	**G_{12} [GPa]**	ν_{12} **[-]**
A	0.207	74.30	73.20	4.40	0.04
B	0.203	115.50	105.70	4.42	0.01

Table 4.2: Material failure properties used for validation.

Material	**X_t [MPa]**	**Y_t [MPa]**	**X_c [MPa]**	**Y_c [MPa]**	**S_{12} [MPa]**
A	1096	1082	889	878	149
B	659	614	582	521	99

The first validation step is to confirm that the CLT is being applied correctly. To assess it, one can compare the stiffness matrices A, B and D obtained from the model and calculated in ESAcomp software. The results obtained were:

	Model	**ESAcomp**
	Specimen 1	
$[A]$	$\begin{bmatrix} 96.60e+6 & 30.58e+6 & 0 \\ 30.58e+6 & 96.60e+6 & 0 \\ 0 & 0 & 33.01e+6 \end{bmatrix}$	$\begin{bmatrix} 96.60e+6 & 30.58e+6 & 0 \\ 30.58e+6 & 96.60e+6 & 0 \\ 0 & 0 & 33.01e+6 \end{bmatrix}$
$[B]$	$\begin{bmatrix} 0 & 0 & 0 \\ 0 & 0 & 0 \\ 0 & 0 & 0 \end{bmatrix}$	$\begin{bmatrix} 0 & 0 & 0 \\ 0 & 0 & 0 \\ 0 & 0 & 0 \end{bmatrix}$
$[D]$	$\begin{bmatrix} 23.30 & 5.886 & 0.020 \\ 5.886 & 23.06 & 0.020 \\ 0.020 & 0.020 & 6.441 \end{bmatrix}$	$\begin{bmatrix} 23.30 & 5.886 & 0.020 \\ 5.886 & 23.06 & 0.020 \\ 0.020 & 0.020 & 6.441 \end{bmatrix}$

Specimen 2

$$[A] \quad \begin{bmatrix} 15.10e+7 & 3.286e+6 & 0 \\ 3.286e+6 & 15.10e+7 & 0 \\ 0 & 0 & 7.232e+7 \end{bmatrix} \quad \begin{bmatrix} 15.10e+7 & 3.286e+6 & 0 \\ 3.286e+6 & 15.10e+7 & 0 \\ 0 & 0 & 7.232e+7 \end{bmatrix}$$

$$[B] \quad \begin{bmatrix} 0 & 0 & 0 \\ 0 & 0 & 0 \\ 0 & 0 & 0 \end{bmatrix} \quad \begin{bmatrix} 0 & 0 & 0 \\ 0 & 0 & 0 \\ 0 & 0 & 0 \end{bmatrix}$$

$$[D] \quad \begin{bmatrix} 33.02 & 0.801 & 0 \\ 0.801 & 32.13 & 0 \\ 0 & 0 & 1.620 \end{bmatrix} \quad \begin{bmatrix} 33.02 & 0.801 & 0 \\ 0.801 & 32.13 & 0 \\ 0 & 0 & 1.620 \end{bmatrix}$$

Specimen 3

$$[A] \quad \begin{bmatrix} 48.53e+6 & 15.30e+6 & 0 \\ 15.30e+6 & 48.53e+6 & 0 \\ 0 & 0 & 16.50e+6 \end{bmatrix} \quad \begin{bmatrix} 48.53e+6 & 15.30e+6 & 0 \\ 15.30e+6 & 48.07e+6 & 0 \\ 0 & 0 & 16.50e+6 \end{bmatrix}$$

$$[B] \quad \begin{bmatrix} 2709 & -2662 & 11.80 \\ -2662 & 2615 & 11.80 \\ 11.80 & 11.80 & -2662 \end{bmatrix} \quad \begin{bmatrix} 2709 & -2662 & 11.80 \\ -2662 & 2615 & 11.80 \\ 11.80 & 11.80 & -2662 \end{bmatrix}$$

$$[D] \quad \begin{bmatrix} 2.772 & 0.874 & -0.005 \\ 0.874 & 2.746 & -0.005 \\ -0.005 & -0.005 & 0.943 \end{bmatrix} \quad \begin{bmatrix} 2.772 & 0.874 & -0.005 \\ 0.874 & 2.746 & -0.005 \\ -0.005 & -0.005 & 0.943 \end{bmatrix}$$

Specimen 4

$$[A] \quad \begin{bmatrix} 48.53e+6 & 15.29e+6 & 0 \\ 15.29e+6 & 48.07e+6 & 0 \\ 0 & 0 & 16.50e+6 \end{bmatrix} \quad \begin{bmatrix} 48.53e+6 & 15.29e+6 & 0 \\ 15.29e+6 & 48.07e+6 & 0 \\ 0 & 0 & 16.50e+6 \end{bmatrix}$$

$$[B] \quad \begin{bmatrix} 2710 & -2662 & 11.80 \\ -2662 & 2615 & 11.80 \\ 11.80 & 11.80 & -2662 \end{bmatrix} \quad \begin{bmatrix} 2710 & -2662 & 11.80 \\ -2662 & 2615 & 11.80 \\ 11.80 & 11.80 & -2662 \end{bmatrix}$$

$$[D] \quad \begin{bmatrix} 2.772 & 0.874 & -0.005 \\ 0.874 & 2.746 & -0.005 \\ -0.005 & -0.005 & 0.943 \end{bmatrix} \quad \begin{bmatrix} 2.772 & 0.874 & -0.005 \\ 0.874 & 2.746 & -0.005 \\ -0.005 & -0.005 & 0.943 \end{bmatrix}$$

As seen, the values given by the model and by the ESAcomp software are equal, meaning that the model is calculating the stiffness matrices in the correct way.

In addition, for symmetric layups S1 and S2, the B matrices are null, as expected. For the S3 layup, a balanced one, it is shown that $A_{16} = A26 = 0$. In the case of the anti-symmetric S4 layup,

D_{16} and D_{26} should be equal to zero, which they are not. However, their values are near zero and negligible.

The next step to validate the model is to confirm the stress and strains through the thickness in the critical point and the first ply failure criterion. These two stages can be done simultaneously by retrieving the critical load and inputting its value in the ESAcomp software. Then, the results were graphically compared. For means of example, in this section, only the stress and strain both of the xx and fibre direction for the first laminate are shown in Figure 4.2. The rest is shown in the Appendix B.

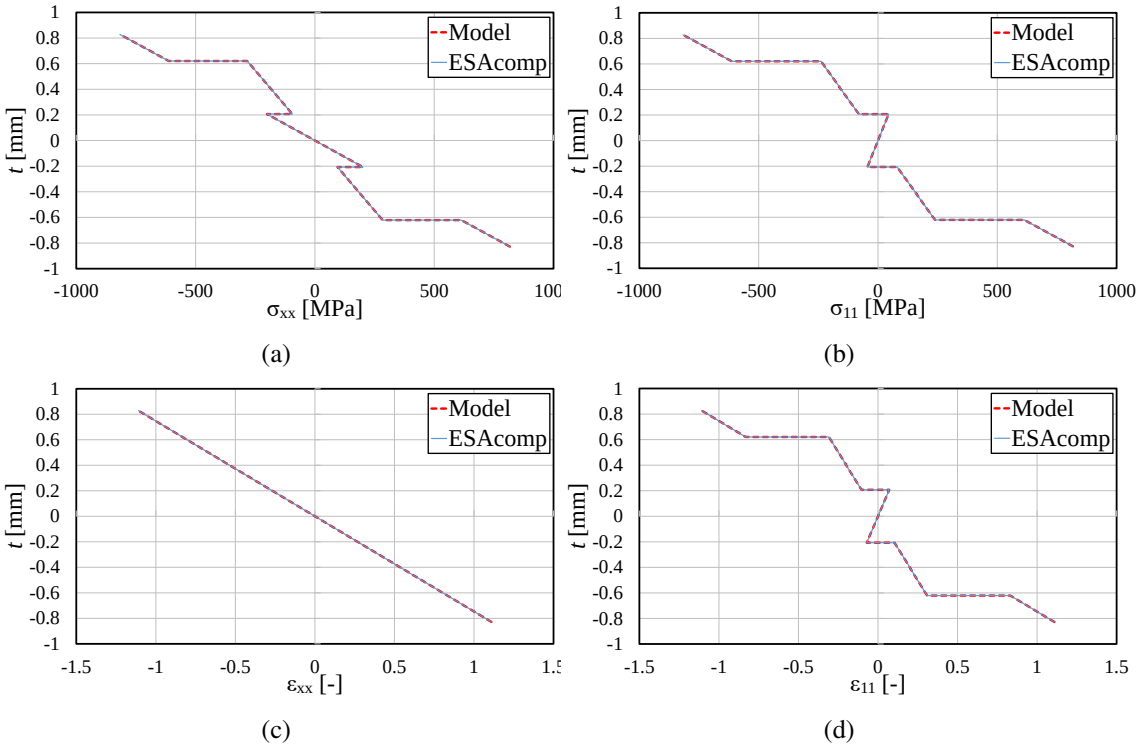

Figure 4.2: Code validation graphically represented for first laminate: (a) σ_{xx}; (b) σ_{11}; (c) ε_{xx}; (d) ε_{11}.

4.2 Container optimisation

To design and choose the composite container while ensuring structural integrity and decreasing weight, Hypermesh was used in optimisation mode. The process was used for both the lid and bottom container.

4.2.1 The process

The process of composite optimisation using Altair Hypermesh is divided into four major parts: geometry modelling, free sizing, continuous and discrete sizing, and shuffling.

In this first phase, one models the component and prepares it for analysis. This includes the geometry, material, material orientations and references, shapes, loads and boundary conditions (BCs), mesh and mesh convergence.

Then, it is necessary to prepare the model for the free sizing step. The first step was to define the design variable, which, in this case, was the composite layup. Then, the optimisation responses (mass and compliance weight) were set for later constraints and objectives. The objective of the optimisation is to minimize the load case compliance weight while constraining the maximum component mass. The last step before the first simulation was to set the controls. The maximum iteration number was set to 200 and the convergence criteria to 0.05%.

The output of the free-sizing phase was the plies initial shape and thickness required to best respond to the load case. However, the geometries must be adjusted to make possible later manufacturability of the component. In addition, one can input the maximum ply thickness for each ply and define more optimisation constraints. In this analysis, another constraint was created, regarding the major stress of the element. This step is called continuous sizing.

After this second simulation, one must give the software the manufacturable thickness of each ply. After running another simulation, the software outputs the required number of plies of each orientation.

The last step is shuffling, where the plies are ordered to optimise the optimisation objective while complying with its constraints.

4.2.2 Lid optimisation

4.2.2.1 Geometry

The lid is a simple component that closes the container. It constitutes a simple panel with an angled surface to reduce the space occupied and allow the accumulator closer to the firewall, as shown in Figure 4.3.

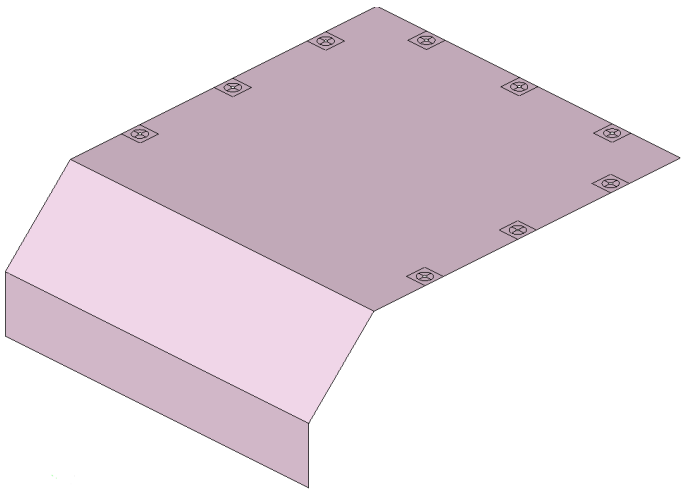

Figure 4.3: Lid optimisation geometry.

The main dimensions are:

- **Width:** 490 mm;
- **Length:** 600 mm;
- **Height:** 190 mm;

4.2.2.2 Material

There are three materials used in the lid: aluminium, CFRP and GFRP, with elastic properties and density listed in Table 4.3 (Toray)(Composites).

Table 4.3: Material elastic properties and density for lid optimisation.

Material	E_1 [GPa]	E_2 [GPa]	G_{12} [GPa]	ν_{12} [-]	Density g/cm^3
Aluminium	70.00	-	25.00	0.33	2.700
CFRP	62.20	64.20	3.86	0.02	1.5892
GFRP	24.25	24.25	0.1	4.30	2.000

In addition, the failure properties of the CFRP were known and defined as in Table 4.4 (Toray):

Table 4.4: Material failure properties used for lid optimisation.

Material	X_t [MPa]	Y_t [MPa]	X_c [MPa]	Y_c [MPa]	S_{12} [MPa]
CFRP	768	776	731	836	123

4.2.2.3 Laminate creation

In this phase, it was only necessary to create the master plies, meaning that only one ply with increased thickness was created for each orientation. Thus, a laminate with a total of 6 plies:

- **Aluminium:** Although the aluminium plate is not a composite, to input it in the software one can assign a ply with the correspondent plate thickness;
- **CFRP:** 4 plies, one in each direction;
- **GFRP:** 1 ply for isolation.

The final laminate had the characteristics listed in Table 4.5:

Note that while the CFRP plies are over-dimensioned, the aluminium and GFRP ones are not. This comes because these plies only exist to rules compliance and electrical safety. Thus, only one ply for each is necessary. Since at this phase one cannot tell how many plies for each orientation would be necessary, an increased thickness of 1 mm was given for the total orientation thickness.

After creating the laminate, a PCOMPP property was created and assigned to the entire lid, as shown in Figure 4.4.

Table 4.5: Master laminate for lid optimisation.

Ply number	Material	Orientation[°]	Thickness [mm]
1	Aluminium	0	0.5
2	CFRP	0	1.0
3	CFRP	45	1.0
4	CFRP	-45	1.0
5	CFRP	90	1.0
6	GFRP	0	0.5

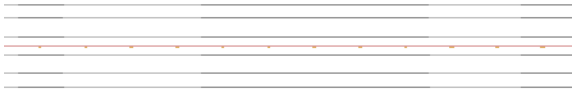

Figure 4.4: Lid optimisation initial lay-up.

4.2.2.4 Boundary conditions

The lid bolts to the bottom container through nine M4 bolts on the top surface. To evenly distribute the force over a larger area, backing plates of 20 mm diameter will be placed between the bolt head and the composite component. One can assume that the connection restricts the component displacement in every direction over this 20 mm diameter surface around the hole while allowing rotation. Thus, a boundary condition that restricts U1, U2 and U3 is applied as seen in Figure 4.5.

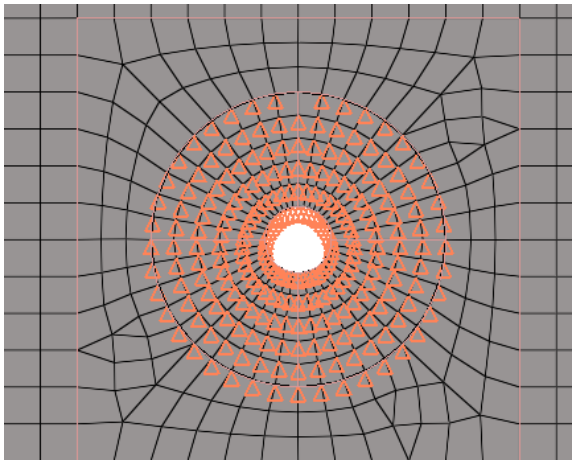

Figure 4.5: Boundary condition applied to all nine holes in the lid.

4.2.2.5 Loads

The load is caused by a vertical acceleration of 20g. The lid supports the cell stacks, meaning that the force will be twenty times its weight, which is 38.138 kilograms. Thus, the force applied to this plate is equal to:

$$F = 20 \cdot g \cdot W = 20 \cdot 9.81[m/s^2] \cdot 38.138[kg] = 7482.28[N] \tag{4.6}$$

The load is considered to be uniformly distributed by a specific zone of the plate. The load is applied in a zone of 390x450 mm. Therefore, the pressure applied is calculated as follows:

$$P = \frac{7482.28[N]}{390[mm] \cdot 450[mm]} = 0.043[MPa] \tag{4.7}$$

The pressure was then applied to the lid as shown in Figure 4.6.

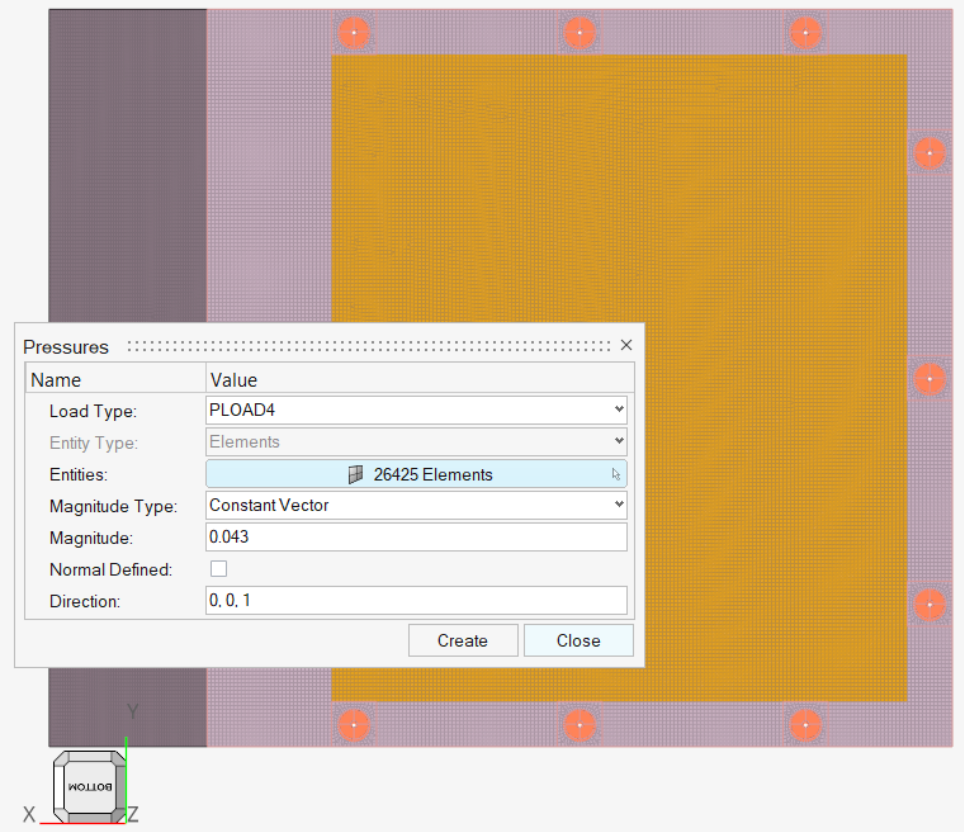

Figure 4.6: Load applied to the lid.

4.2.2.6 Mesh and mesh convergence

Before starting the optimisation process, it was necessary to conduct a mesh convergence study. The lid is a relatively simple geometry to mesh, so the main goal was to maintain a structured quad-element mesh. However, the holes for bolts induce discontinuities that cause a mesh quality loss. Thus, this non-structured mesh must be contained so that it does not affect the rest of the mesh.

With this in mind, the geometry shown in Figure 4.7 was created.

The small hole of 4.5 mm diameter constitutes the through-hole for the bolt. The outside circle of 20 mm diameter represents the backing plate area and will be used for mesh refinement around

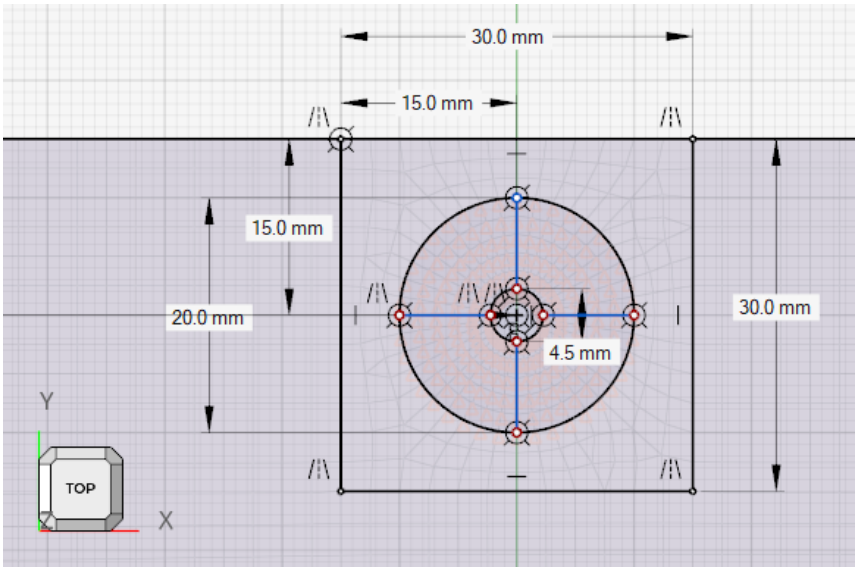

Figure 4.7: Geometry around the hole in the lid.

the hole. In addition, two vertical and two horizontal lines were added for further mesh refinement. Then, one can observe a square of 30 mm, created to contain the non-structured mesh and make the transition from the local to the general mesh smoother.

Figure 4.8 shows an example of the mesh around the hole.

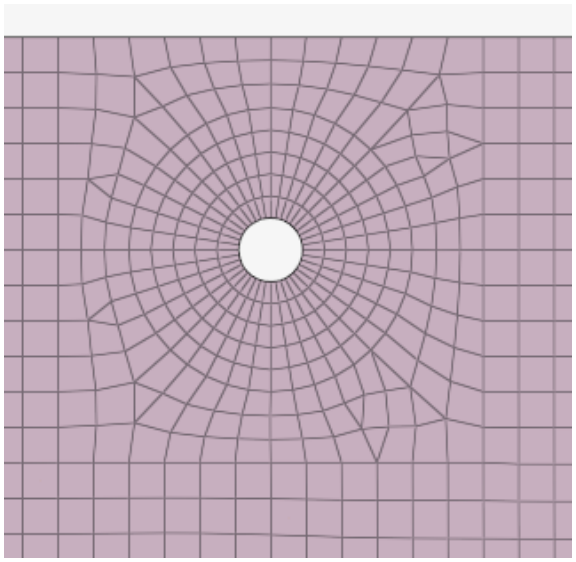

Figure 4.8: Mesh around the hole in the lid.

Then, one started the mesh convergence study, by starting with a 12 mm element size and successively reducing it until convergence is observed. To make this study, the laminate used, for simplicity, consisted of an outer aluminium layer, one GFRP inner ply and a $(0/45/-45/90)_S$ CFRP layup. The results for the different simulations are shown in Table 4.6 and Figure 4.9 shows their graphically representation.

Table 4.6: Results of mesh convergence study.

Size [mm]	**Nodes [-]**	**Elements [-]**	σ_1 **[MPa]**	σ_2 **[MPa]**	σ_{12} **[MPa]**
12.0	5916	5769	1277 (-)	551.4 (-)	687.6 (-)
7.5	8790	8531	1306 (2.27%)	524.9 (-8.96%)	474.2 (-31.04%)
5.0	16966	16613	1369 (4.82%)	524.9 (4.56%)	473.5 (-0.14%)
2.5	59300	58696	1405 (2.63%)	525.1 (0.04%)	471.8 (-0.36%)
2.0	91217	90491	1410 (0.36%)	525.3 (0.04%)	470.8 (-0.32%)

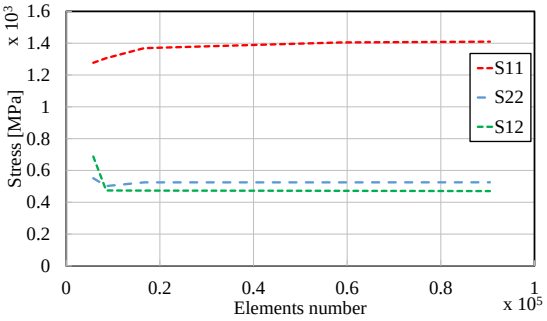

Figure 4.9: Plot of lid mesh convergence study.

Since the last iteration only gives a maximum error of 0.36%, the mesh with 2.5 mm was used to reduce computational time, while giving accurate results.

The results of this simulation are shown in Figure 4.10 and Figure 4.11.

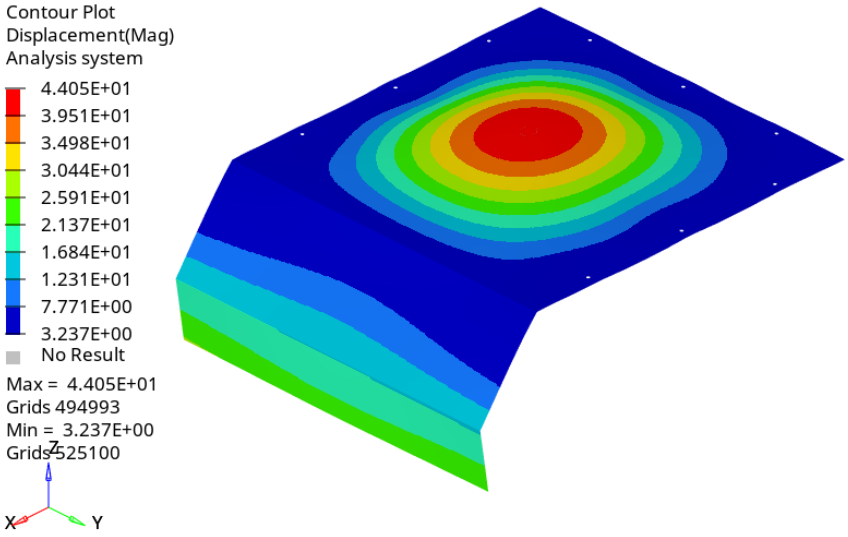

Figure 4.10: Lid mesh convergence displacement field.

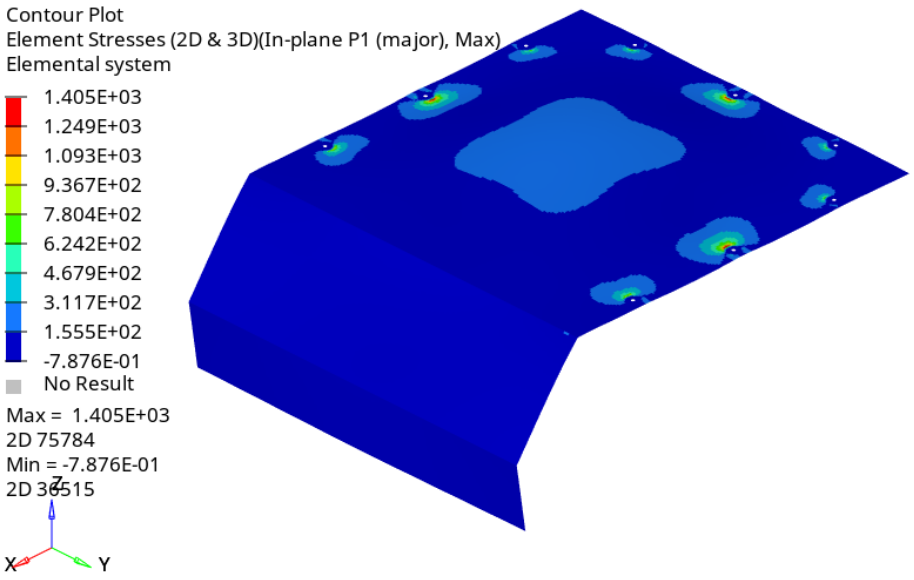
Contour Plot
Element Stresses (2D & 3D)(In-plane P1 (major), Max)
Elemental system
1.405E+03
1.249E+03
1.093E+03
9.367E+02
7.804E+02
6.242E+02
4.679E+02
3.117E+02
1.555E+02
-7.876E-01
No Result
Max = 1.405E+03
2D 75784
Min = -7.876E-01
2D 36515
Z
X
Y

(a)

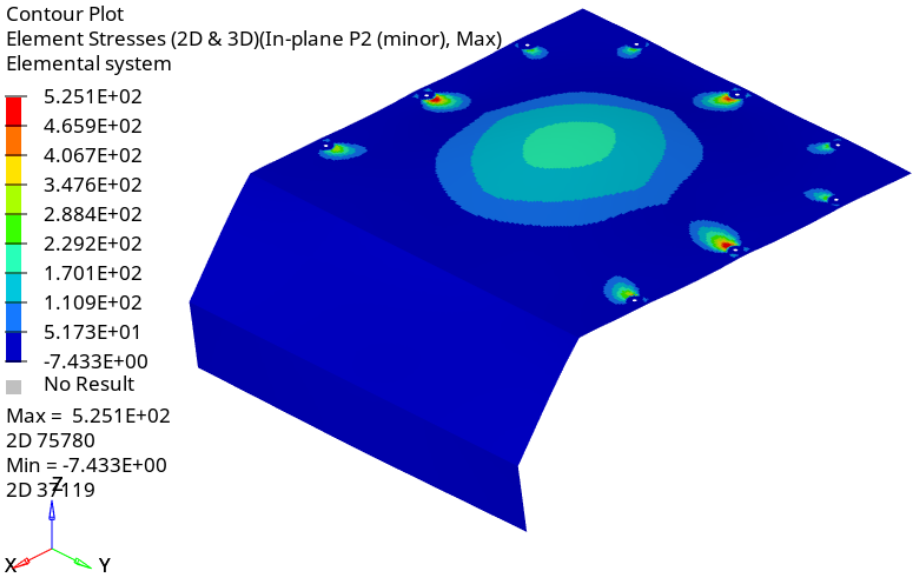
Contour Plot
Element Stresses (2D & 3D)(In-plane P2 (minor), Max)
Elemental system
5.251E+02
4.659E+02
4.067E+02
3.476E+02
2.884E+02
2.292E+02
1.701E+02
1.109E+02
5.173E+01
-7.433E+00
No Result
Max = 5.251E+02
2D 75780
Min = -7.433E+00
2D 37119
Z
X
Y

(b)

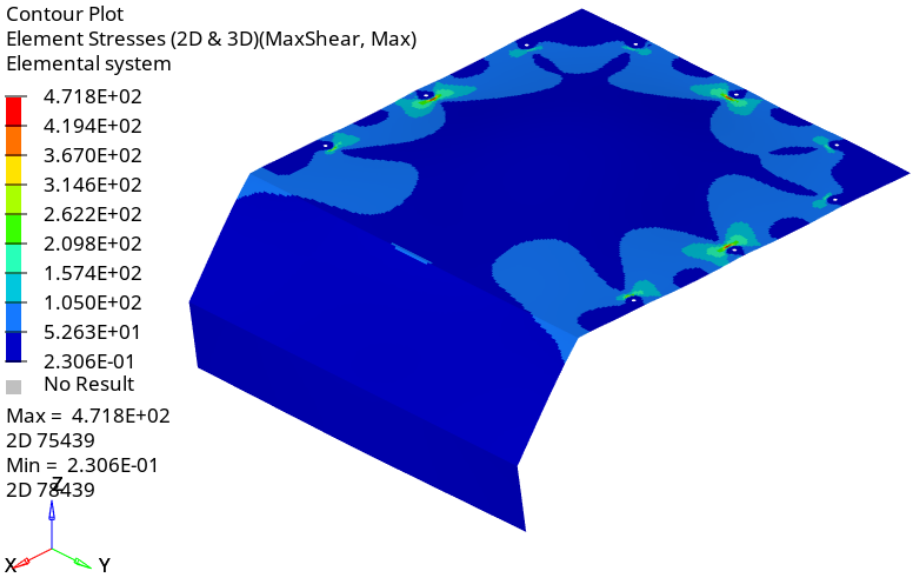

(c)

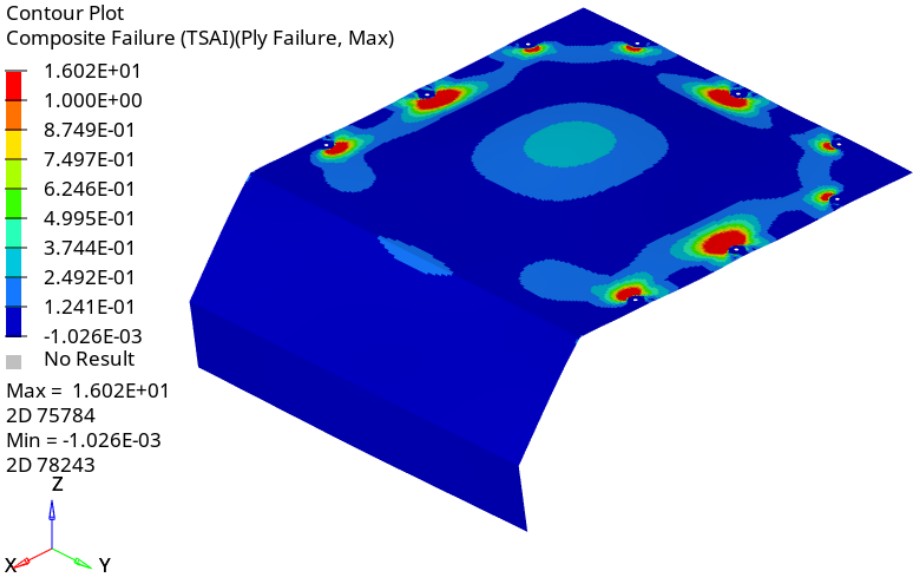

(d)

Figure 4.11: Lid mesh convergence: (a) Major principal stress; (b) Minor principal stress; (c) Shear stress; (d) Tsai-Wu failure index.

Although the TSAI failure index is large, meaning that the layup is sub-dimensioned, one can conclude that there is a high concentration factor around the bolted holes and there will be the need to reinforce this zone.

4.2.2.7 Free-sizing

After the mesh convergence study, the optimisation itself can begin. As explained before, the first step is a free-sizing simulation. The design variable was set to the composite layup, with the maximum mass constraint of 2.10 kg and the objective to minimise load weight compliance. The maximum laminate thickness was also constrained to a maximum of 3.5 mm. The initial lid weight is 3.12 kg.

Convergence was achieved after 129 iterations with the following laminate thickness distribution and a total weight of 2.25 kg, which is above the 2.10 kg limit:

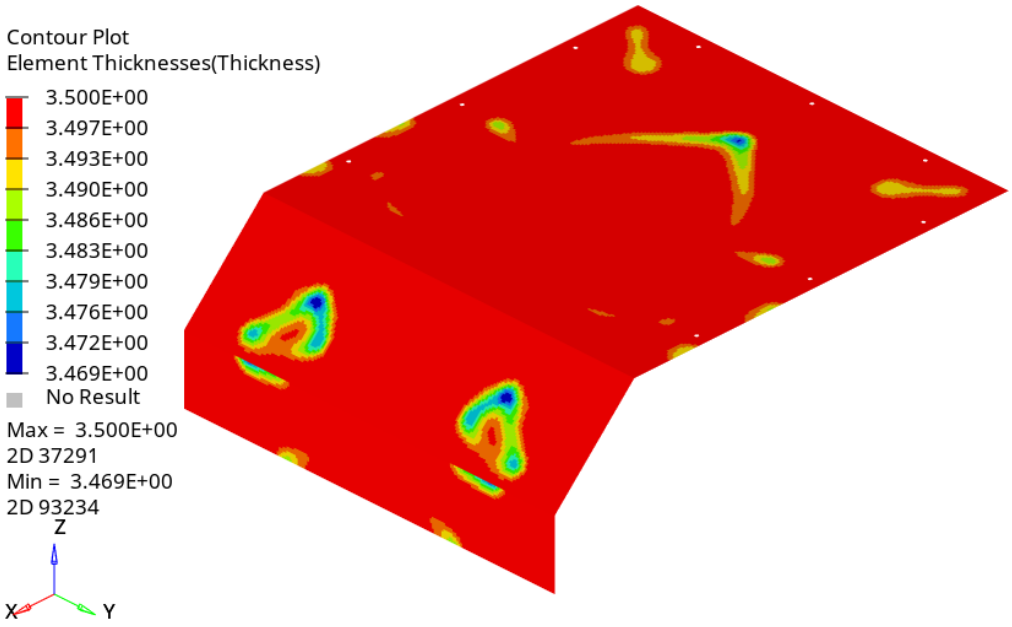

Figure 4.12: Lid free-sizing step element thickness.

For means of example, the four shapes suggested by this simulation for the 0-degree CFRP ply are shown in Figure 4.13.

4.2.2.8 Continuous sizing

The first step in preparing this phase was to change the shapes to manufacturable ones, by adding or subtracting elements. In addition, it is here that some design constraints came into place. For example, the aluminium and GFRP plies will not have reinforcement plies, meaning that the three last shapes were deleted. As seen before in the mesh convergence study, the main zone that needs reinforcement is the holes. For this reason, two different shapes were maintained for CFRP: one for the whole component and one for the reinforcement, both shown in Figure 4.14.

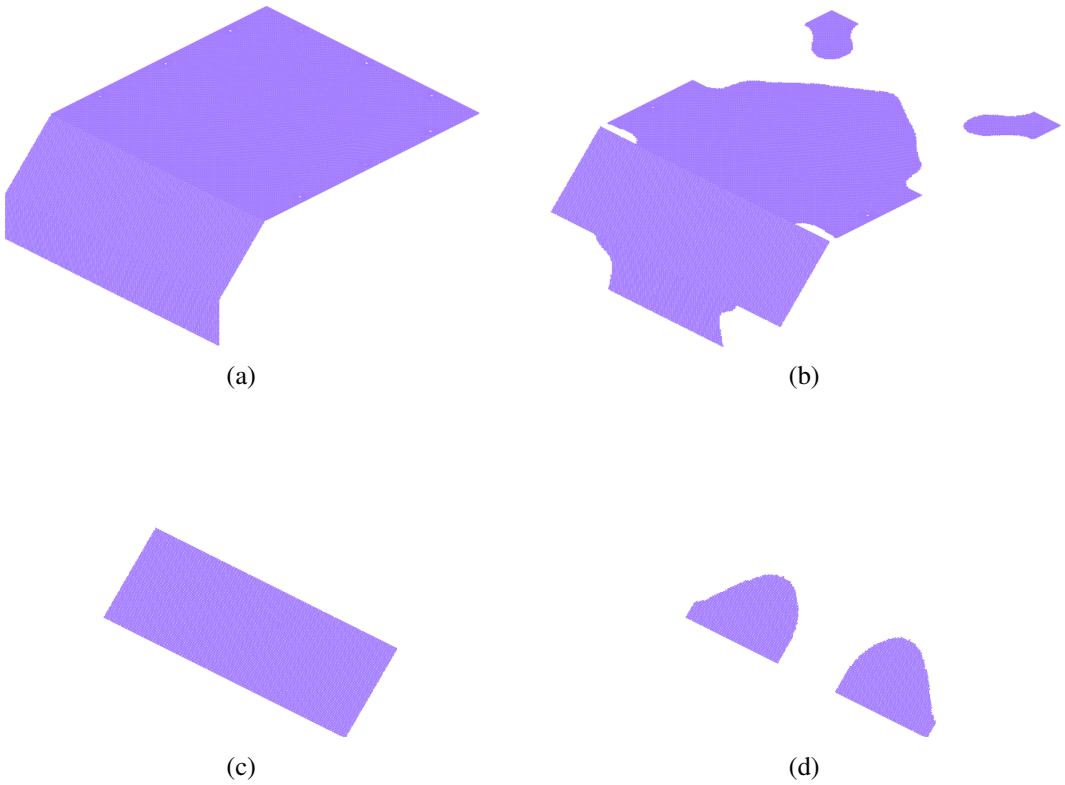

(a) (b)

(c) (d)

Figure 4.13: 0-degree CFRP ply reinforcement shapes according to load path after free-sizing: (a) main shape; (b) main reinforcement; (c) second reinforcement shape; (d) small reinforcement shape.

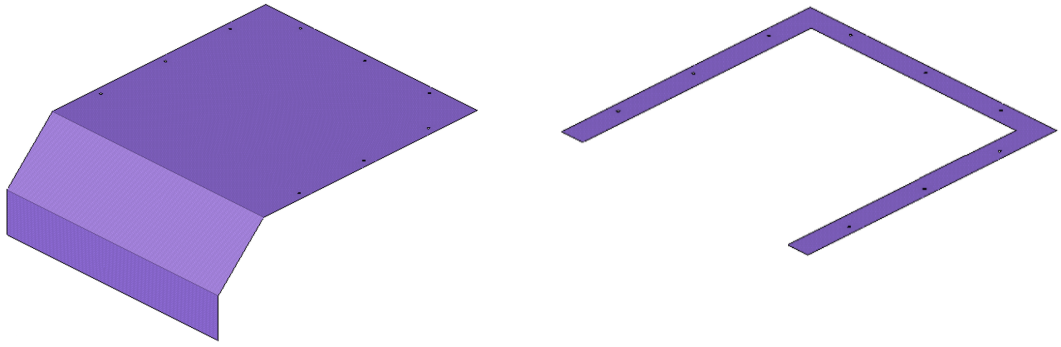

(a) (b)

Figure 4.14: CFRP ply shapes: (a) whole compoenent; (b) reinforcement.

Then, it was necessary to constrain the maximum shape thickness for each orientation:

- **Aluminium:** 0.5 mm - only one ply;
- **CFRP base:** 0.422 mm - maximum two plies;
- **CFRP reinforce:** 0.211 mm - maximum one ply;
- **GFRP:** 0.5 mm - only one ply.

In addition, a new constraint of major stress was created to ensure that the ply major stress would stay between -750 MPa and 750 MPa.

The second simulation achieved convergence after 24 iterations, with laminate thickness as shown in Figure 4.15.

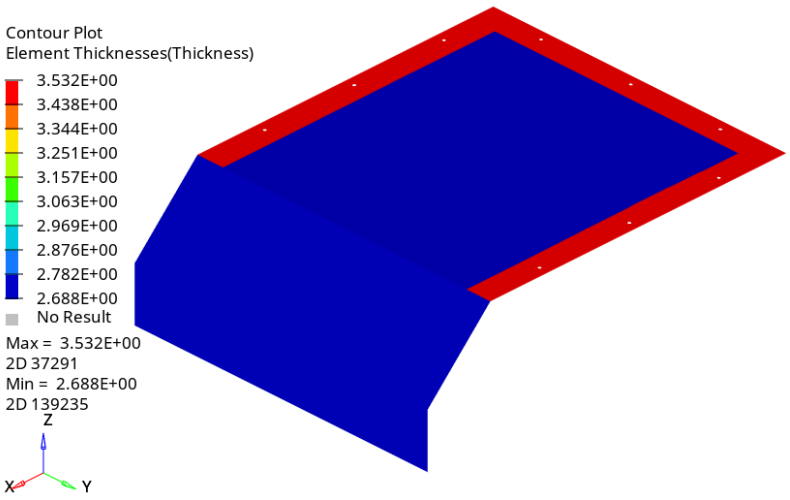

Figure 4.15: Element thickness after continuous sizing.

Table 4.7 shows the ply thickeness for each orientation and shape.

Table 4.7: Lid ply thickness after continuous sizing.

Material	Orientation [°]	Shape	Thickness [mm]
Aluminium	0	Base	0.380
CFRP	0	Base	0.400
CFRP	0	Reinforcement	0.100
CFRP	45	Base	0.400
CFRP	45	Reinforcement	0.100
CFRP	-45	Base	0.400
CFRP	-45	Reinforcement	0.100
CFRP	90	Base	0.400
CFRP	90	Reinforcement	0.100
GFRP	0	Base	0.218

4.2.2.9 Discrete sizing

The continuous sizing was done first to avoid convergence problems due to imposed manufacturing ply thicknesses. Thus, after knowing the necessary ply thickness for each orientation, the next step was to make this thickness discrete with manufacturable ply thicknesses.

- **Aluminium:** 0.5 mm;
- **CFRP base:** 0.211 mm;

- **CFRP reinforce:** 0.211mm;
- **GFRP:** 0.5 mm.

After the third simulation, which converged after four iterations, the laminate weight was 1.90 kg and had the plies shown in Table 4.8.

Table 4.8: Lid ply thickness after discrete sizing.

Ply	**Material**	**Orientation** [°]	**Shape**	**Thickness [mm]**
1	**Aluminium**	0	Base	0.5
2	**CFRP**	0	Base	0.211
3	**CFRP**	0	Base	0.211
4	**CFRP**	0	Reinforcement	0.211
5	**CFRP**	45	Base	0.211
6	**CFRP**	45	Base	0.211
7	**CFRP**	45	Reinforcement	0.211
8	**CFRP**	-45	Base	0.211
9	**CFRP**	-45	Base	0.211
10	**CFRP**	-45	Reinforcement	0.211
11	**CFRP**	90	Base	0.211
12	**CFRP**	90	Base	0.211
13	**CFRP**	90	Reinforcement	0.211
14	**GFRP**	0	Base	0.5

The element thickness is shown in Figure 4.16.

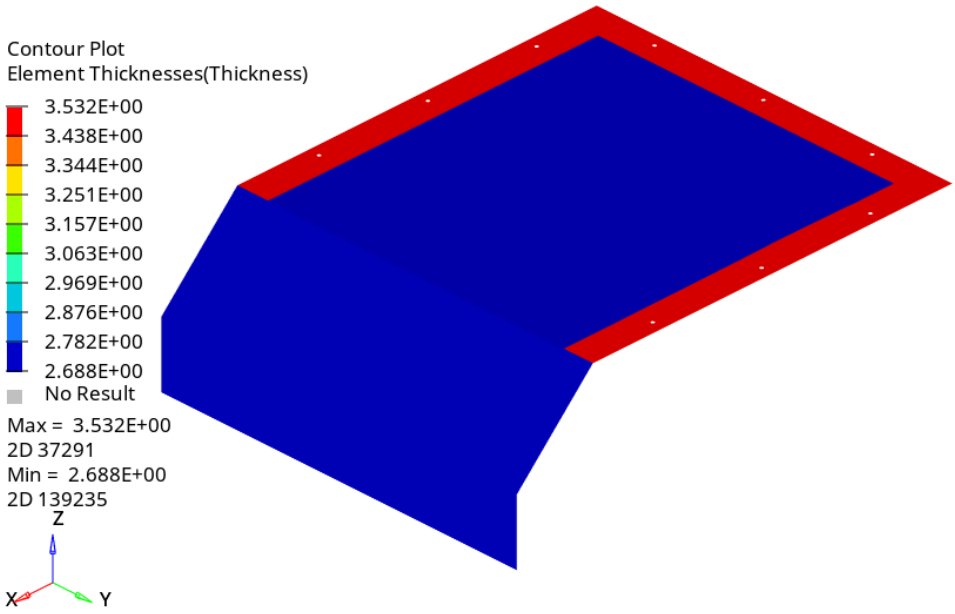

Figure 4.16: Element thickness after discrete sizing.

4.2.2.10 Shuffling

After having the necessary plies for each orientation, it is necessary to shuffle them to find the optimum layup possible for this specific load case. This is done by a shuffling simulation that tries different layups as seen in Figure 4.17. Note that there are two plies with orientations 40° and 30°. These orientations were given to GFRP and aluminium, respectively, to make it possible for the software to identify them and place them at the top and bottom of the laminate.

Stacking sequence for STACK 1

Iteration 0	Iteration 1	Iteration 2	Iteration 3	Iteration 4
1101	6101	6101	6101	6101
2101	3101	2201	2201	2201
2102	4101	2101	5201	5201
2201	2101	5201	3101	3101
3101	5101	5101	4101	4101
3102	3102	3101	2101	2101
3201	4102	4101	2102	2102
4101	2102	3102	5102	5102
4102	5102	4102	3201	3201
4201	3201	2102	4201	4201
5101	4201	5102	5101	5101
5102	2201	3201	3102	3102
5201	5201	4201	4102	4102
6101	1101	1101	1101	1101

Legend
40.0 degrees
90.0 degrees
-45.0 degrees
45.0 degrees
0.0 degrees
30.0 degrees

Figure 4.17: Lid layup shuffling iterations.

After 4 iterations, it was possible to observe the results of the optimisation. Table 4.9 shows the proposed lay-up.

Table 4.9: Lid layup after shuffling.

Ply	**Material**	**Orientation** [°]	**Shape**	**Thickness [mm]**
1	**GFRP**	0	Base	0.5
2	**CFRP**	0	Reinforcement	0.211
3	**CFRP**	90	Reinforcement	0.211
4	**CFRP**	45	Base	0.211
5	**CFRP**	-45	Base	0.211
6	**CFRP**	0	Base	0.211
7	**CFRP**	0	Base	0.211
8	**CFRP**	90	Base	0.211
9	**CFRP**	45	Reinforcement	0.211
10	**CFRP**	-45	Reinforcement	0.211
11	**CFRP**	90	Base	0.211
12	**CFRP**	45	Base	0.211
13	**CFRP**	-45	Base	0.211
14	**Aluminium**	0	Base	0.5

The displacement and Tsai-Wu index are shown in Figure 4.18

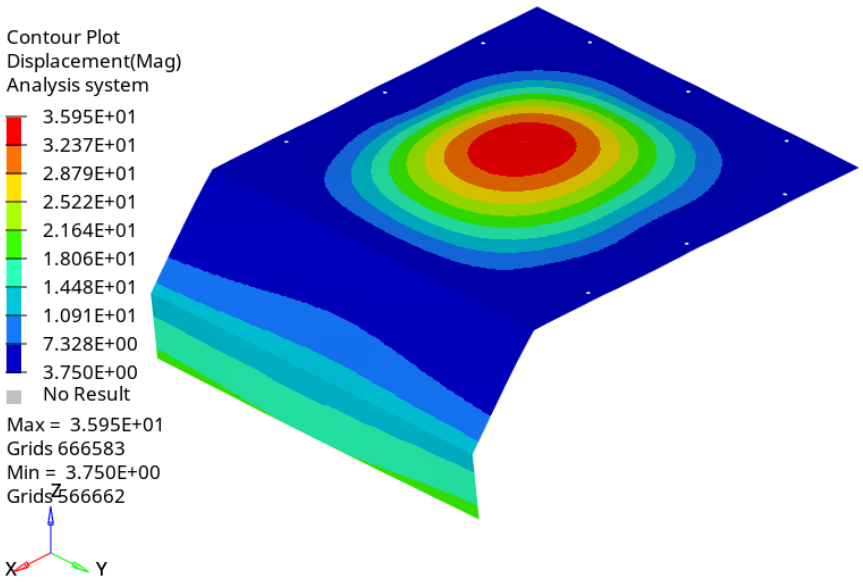

(a)

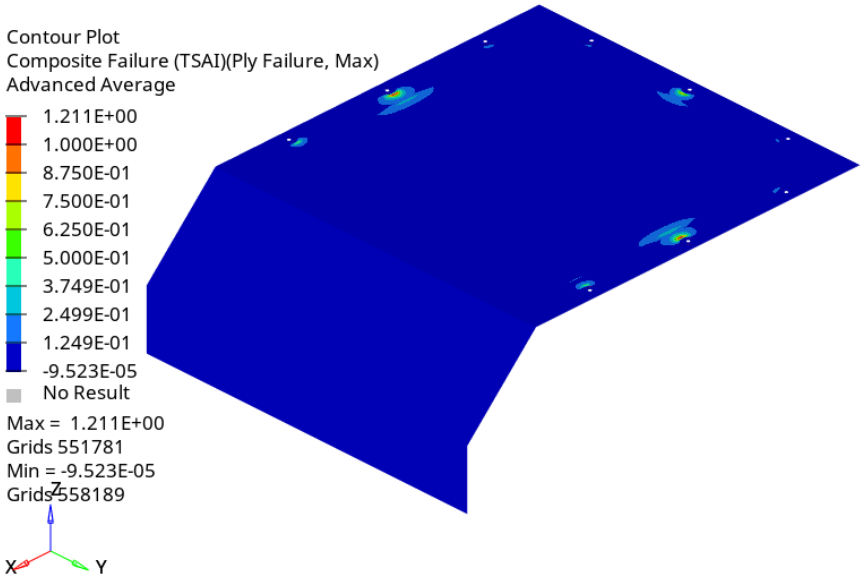

(b)

Figure 4.18: Shuffling lid: (a) displacement field; (b) Tsai-Wu failure index.

4.2.2.11 Analysis

However, one can note some problems with this design, starting with the failure index. As seen, the maximum index is 1.211, although it is only in a few elements around the central hole, as Figure 4.19 shows.

In addition, the CFRP inner part is not symmetric. Although the overall laminate would not be symmetric due to aluminium and GFRP outer layers, it is still a good practice to maintain the

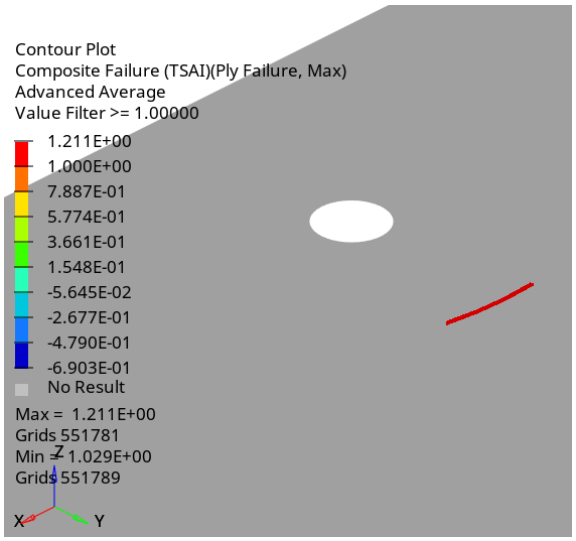

Figure 4.19: Lid layup shuffling Tsai-Wu failure index filtered to values greater than 1.

inner CFRP symmetric. However, having only one reinforcement of 45° and -45°, the layup would never be symmetric. Thus, it was decided to add a 90° ply and remove these two plies. Then, the plies were also reordered as Table 4.10 shows. Figure 4.20 show the respective displacement and Tsai-Wu failure index. The final weight is 1.87 kg.

Table 4.10: Lid layup after reordering.

Ply	**Material**	**Orientation** [°]	**Shape**	**Thickness [mm]**
1	**GFRP**	0	Base	0.5
2	**CFRP**	0	Base	0.211
3	**CFRP**	0	Reinforcement	0.211
4	**CFRP**	45	Base	0.21
5	**CFRP**	-45	Base	0.211
6	**CFRP**	90	Base	0.211
7	**CFRP**	90	Reinforcement	0.211
8	**CFRP**	90	Reinforcement	0.211
9	**CFRP**	90	Base	0.211
10	**CFRP**	-45	Base	0.211
11	**CFRP**	45	Base	0.211
12	**CFRP**	0	Reinforcement	0.211
13	**CFRP**	0	Base	0.211
14	**Aluminium**	0	Base	0.5

Note that the maximum Tsai-Wu failure index decreased to 1.108 and the maximum displacement to 36.14 mm. The value of 1.108 is due to local concentration factors and it is not significative, as seen in Figure 4.21.

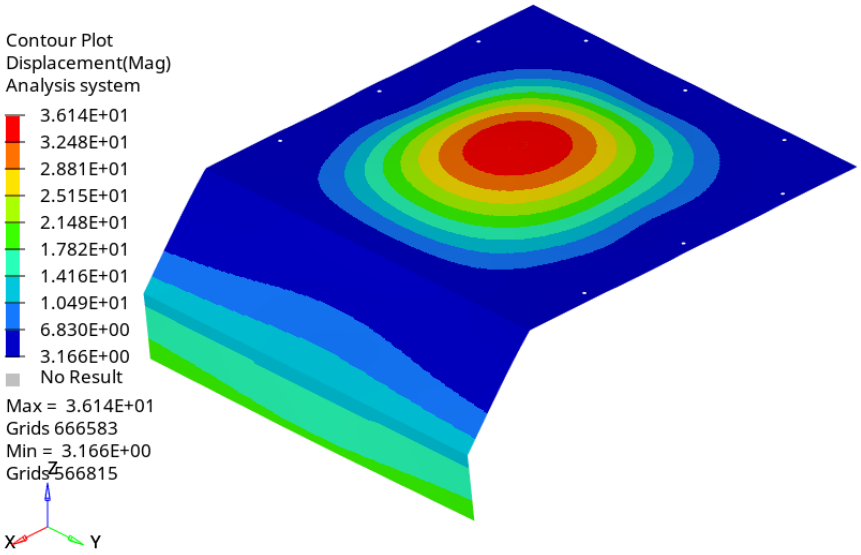

(a)

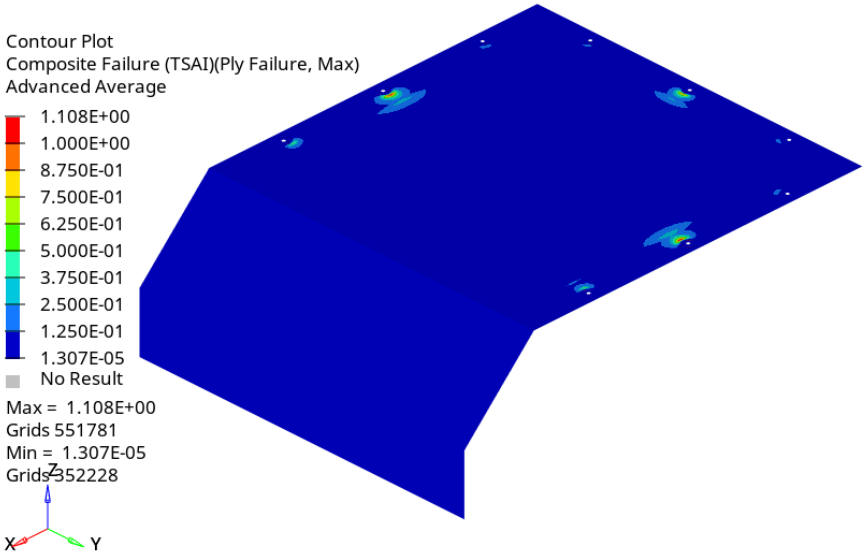

(b)

Figure 4.20: Final lid simulation: (a) displacement field; (b) Tsai-Wu failure index.

4.2.3 Container optimisation

4.2.3.1 Geometry

The container geometry is also simple. It must contain internal walls of the height of at least 75% of the total TSAC height to separate the different segments and electrical components referred to in section 3.3. Figure 4.22 shows its geometry.

Note that the surfaces are partitioned only to allow a better mesh refinement and loads and boundary conditions definition in later sections.

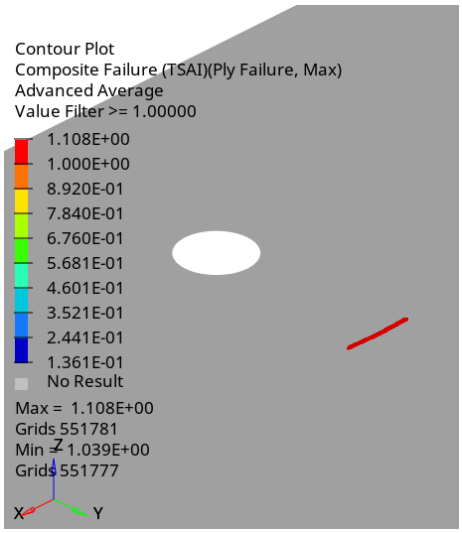

Figure 4.21: Final lid Tsai-Wu failure index filtered to values greater than 1.

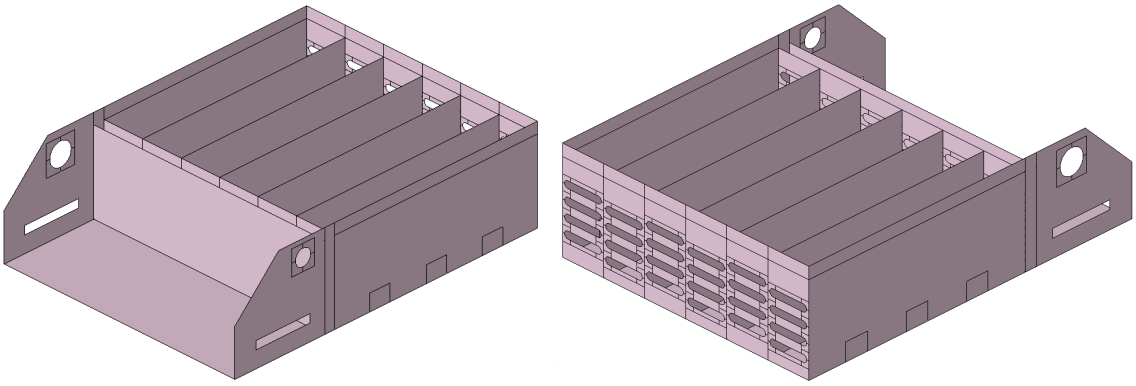

(a) (b)

Figure 4.22: Bottom container geometry: (a) front isometric view; (b) rear isometric view.

There are a few elements that are worth discussing. The circular front lateral holes are for the high and low-voltage connectors, while the rectangular ones are for cooling the battery management system only when the battery is charging. This component heats a lot when charging the cells. Then, the oval holes in the rear external and internal walls allow air to flow through the cells when charging or discharging to cool them. Since the electrical components must be physically separated from the segments, it was necessary to create another inside wall that did not have any holes.

The main dimensions used for this simulation were:

- **Length:** 595 mm;
- **Width:** 450 mm;
- **Height:** 170 mm;
- **Segment slot length:** 390 mm;

- **Segment slot width:** 75 mm;
- **Internal walls height** 150 mm;
- **Air slot between two intenal walls:** 20 mm;

4.2.3.2 Material

The materials used are the same as the ones used in the lid optimisation, defined in Tables 4.3 and 4.4.

4.2.3.3 Laminate creation

However, the laminate is different from the one used in the lid. One can separate the container into two parts: the bottom and external walls, and the internal walls. The bottom and external walls, like the lid, must have an aluminium layer outside and a GRFP ply inside. On the other side, the internal walls must be covered by GFRP plies on both sides. Table 4.11 shows the initial plys definition for both cases.

Table 4.11: Master laminate for bottom optimisation.

Ply number	**Material**	**Orientation**[°]	**Thickness [mm]**
1	Aluminium/GFRP	0	0.5
2	CFRP	0	1.0
3	CFRP	45	1.0
4	CFRP	-45	1.0
5	CFRP	90	1.0
6	GFRP	0	0.5

Note that the same strategy of over-dimensioning only the CFRP plies as in the lid optimisation was used. Then, the process of assigning the laminate was the same.

4.2.3.4 Boundary conditions

The container is mounted to the car by six mounting points that are inserted into its structure. Thus, one can assume that the zone where these inserts are have restricted movement. Thus, one can restrict every degree of freedom, as shown in Figure 4.23.

4.2.3.5 Loads

The bottom container must withstand more load cases than the lid: besides the 20g acceleration on the floor, it also has to resist 40g accelerations both in longitudinal and transversal directions.

Considering that each face will only support the weight of the segment directly related to it, the forces are:

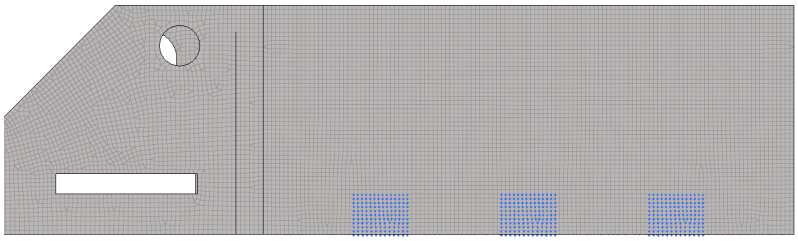

Figure 4.23: Bottom container optimisation boundary conditions.

$$\begin{aligned} F_{40g} &= 40 \times g \times W = 40 \times 9.81[m/s^2] \times 6.356[kg] = 2494.09[\text{N}] \\ F_{20g} &= 20 \times g \times W = 20 \times 9.81[m/s^2] \times 6.356[kg] = 1247.04[\text{N}] \end{aligned} \tag{4.8}$$

Considering the load uniformly distributed:

$$\begin{aligned} P_{long} &= \frac{2494.09[N]}{75[mm] \times 150[mm]} = 0.22[\text{MPa}] \\ P_{trans} &= \frac{2494.09[N]}{390[mm] \times 150[mm]} = 0.04[\text{MPa}] \\ P_{vert} &= \frac{1247.04[N]}{390[mm] \times 75[mm]} = 0.04[\text{MPa}] \end{aligned} \tag{4.9}$$

The different load cases are shown in Figure 4.24.

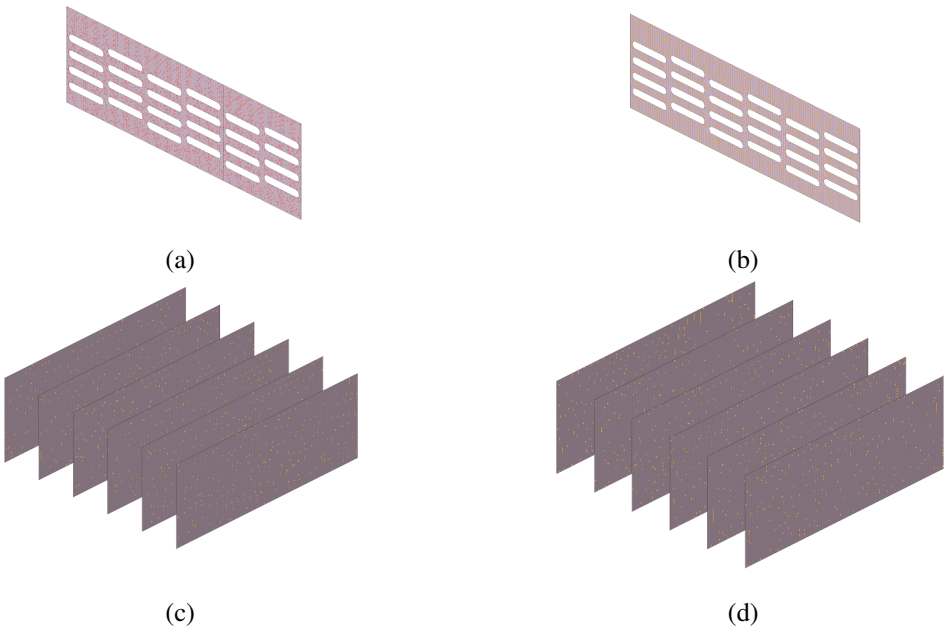

(a) (b)

(c) (d)

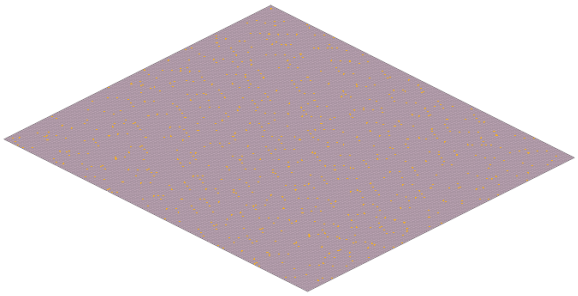

(e)

Figure 4.24: Bottom container load cases: (a) 40g longitudinal direction 1; (b) 40g longitudinal direction 2; (c) 40g transversal direction 1; (d) 40g transversal direction 2; (e) 20g vertical direction.

4.2.3.6 Mesh and mesh convergence

The mesh creation followed the principle of maintaining the mesh in the most structured possible. There are a few geometric components that induce discontinuities in the mesh and disturb it, such as the cooling and connector holes.

For the connector holes, one has done a square to contain the non-structured mesh and to improve the mesh quality around the hole, as seen in Figure 4.25 (a). For the cooling holes, it was necessary to make a geometric structure to improve the overall mesh quality, as seen in Figure 4.25 (b).

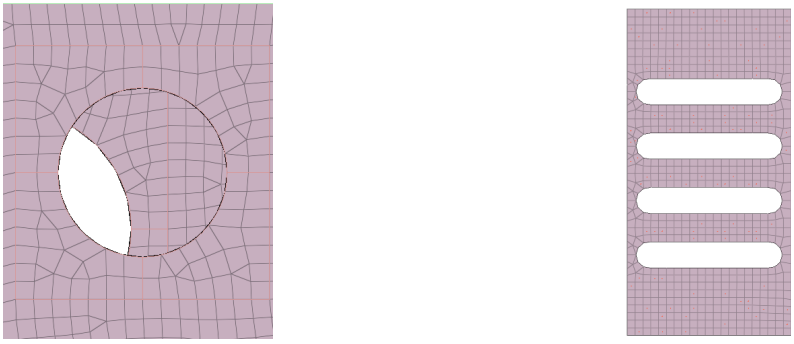

(a) (b)

Figure 4.25: Bottom container mesh refinement: (a) around connector holes; (b) around cooling holes.

Similarly to the lid optimisation mesh convergence study, the laminate used consisted of an outer aluminium layer, one GFRP inner ply and a $(0/45/-45/90)_S$ CFRP layup. The results for the different load cases are shown from Table 4.12 to Table 4.16.

Note that the load cases are related to separated walls. For this reason, it was possible to do the mesh convergence study separately for all the load cases. One could give an equal element

Table 4.12: Mesh convergence study results for 40g longitudinal front to back load case.

Element size [mm]	**Nodes [-]**	**Elements [-]**	σ_1 **[MPa]**	σ_2 **[MPa]**	σ_{12} **[MPa]**
7.50	17759	17325	67.10 (-)	20.57 (-)	36.56 (-)
5.00	39286	38726	142.0 (111.6%)	37.33 (81.48%)	104.2 (185.01%)
4.00	59302	58183	144.2 (1.550%)	39.35 (5.410%)	93.68 (-10.10%)
3.50	73727	72786	143.3 (-0.620%)	39.27 (-0.200%)	94.55 (0.930%)
3.25	78249	77273	143.3 (0.000%)	39.26 (-0.030%)	94.60 (0.050%)
3.15	79797	78835	143.2 (-0.070%)	39.27 (0.030%)	94.61 (0.010%)

Table 4.13: Mesh convergence study results for 40g longitudinal back to front load case.

Element size [mm]	**Nodes [-]**	**Elements [-]**	σ_1 **[MPa]**	σ_2 **[MPa]**	σ_{12} **[MPa]**
7.50	17759	17325	59.32 (-)	17.40 (-)	29.45 (-)
5.00	39286	38726	127.4 (114.8%)	35.86 (106.1%)	64.58 (119.3%)
4.00	59302	58183	140.6 (10.36%)	40.00 (11.54%)	67.97 (5.250%)
3.50	73727	72786	145.7 (3.630%)	41.07 (2.68%)	75.72 (11.40%)
3.25	78249	77273	145.7 (0.000%)	41.32 (0.61%)	75.74 (0.030%)
3.15	79797	78835	145.7 (0.000%)	41.34 (0.05%)	75.75 (0.010%)

Table 4.14: Mesh convergence study results for 40g transversal left to right load case.

Element size [mm]	**Nodes [-]**	**Elements [-]**	σ_1 **[MPa]**	σ_2 **[MPa]**	σ_{12} **[MPa]**
7.50	17759	17325	241.0 (-)	87.91 (-)	102.1 (-)
5.00	39286	38726	262.7 (9.000%)	113.6 (29.22%)	120.5 (10.19%)
4.00	59302	58183	283.0 (7.730%)	130.5 (14.88%)	116.4 (3.470%)
3.50	73727	72786	300.0 (6.010%)	136.9 (4.900%)	118.7 (1.980%)
3.25	78249	77273	303.4 (1.130%)	143.4 (4.750%)	119.7 (0.840%)
3.15	79797	78835	306.6 (1.050%)	146.7 (2.300%)	119.9 (0.170%)

Table 4.15: Mesh convergence study results for 40g transversal right to left load case.

Element size [mm]	**Nodes [-]**	**Elements [-]**	σ_1 **[MPa]**	σ_2 **[MPa]**	σ_{12} **[MPa]**
7.50	17759	17325	241.2 (-)	87.72 (-)	101.9 (-)
5.00	39286	38726	262.3 (8.750%)	113.2 (29.05%)	120.2 (10.11%)
4.00	59302	58183	281.4 (7.280%)	129.9 (14.75%)	116.1 (3.480%)
3.50	73727	72786	298.0 (5.900%)	139.3 (7.010%)	118.4 (1.980%)
3.25	78249	77273	303.2 (1.740%)	142.2 (2.370%)	119.5 (0.930%)
3.15	79797	78835	307.4 (1.390%)	141.5 (-0.560%)	119.6 (0.080%)

Table 4.16: Mesh convergence study results for 20g vertical downwards load case.

Element size [mm]	**Nodes [-]**	**Elements [-]**	σ_1 **[MPa]**	σ_2 **[MPa]**	σ_{12} **[MPa]**
7.50	17759	17325	74.4 (-)	24.83 (-)	34.09 (-)
5.00	39286	38726	102.7 (37.96%)	28.06 (13.01%)	49.41 (24.60%)
4.00	59302	58183	97.7 (-4.840%)	30.51 (8.730%)	46.12 (-6.660%)
3.50	73727	72786	130.5 (33.53%)	31.44 (3.050%)	67.61 (46.60)%)
3.25	78249	77273	130.5 (0.000%)	31.40 (-0.130%)	67.64 (0.040%)
3.15	79797	78835	130.6 (0.080%)	31.40 (0.000%)	67.65 (0.010%)

size to every wall until the last load case has converged. However, due to the large dimension of the container, that would mean a significant increase in element number and computational time. Thus, the mesh refinement was divided into three parts.

In the first one, all the walls had the same element size until the first load case converged, which occurred in the transition to the 3.5 mm element size for the longitudinal load cases.

Then, the element size was only refined in the long walls and the floor. As seen, the vertical load case has also converged doing this. Finally, the long walls were refined by last, having started to converge. Since more refinement meant surpassing the 100000 nodes limited by the student version, the simulation proceeded with the maximum error of 2.30%.

Figure 4.26 illustrates the data shown in the previous tables.

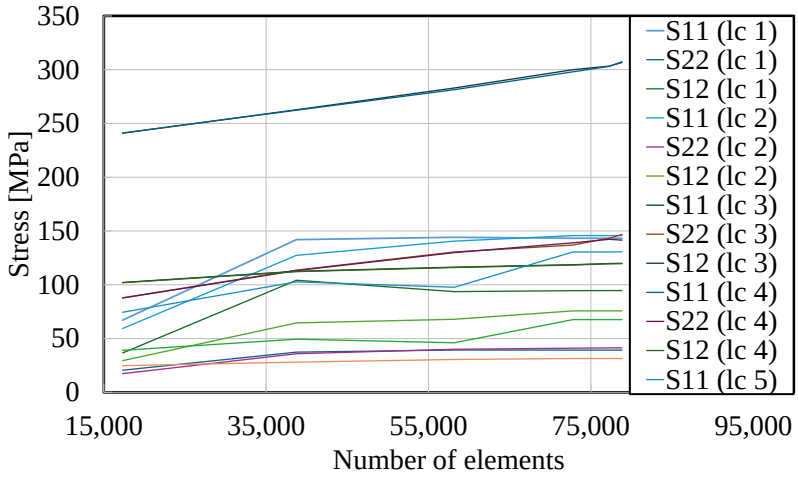

Figure 4.26: Bottom container mesh convergence study.

4.2.3.7 Free sizing

Starting the optimisation itself, the free sizing step converged after 42 iterations and reduced the weight from 7.91 kg to 5.43 kg, with element thickness as shown in Figure 4.27 and a maximum of 4 mm.

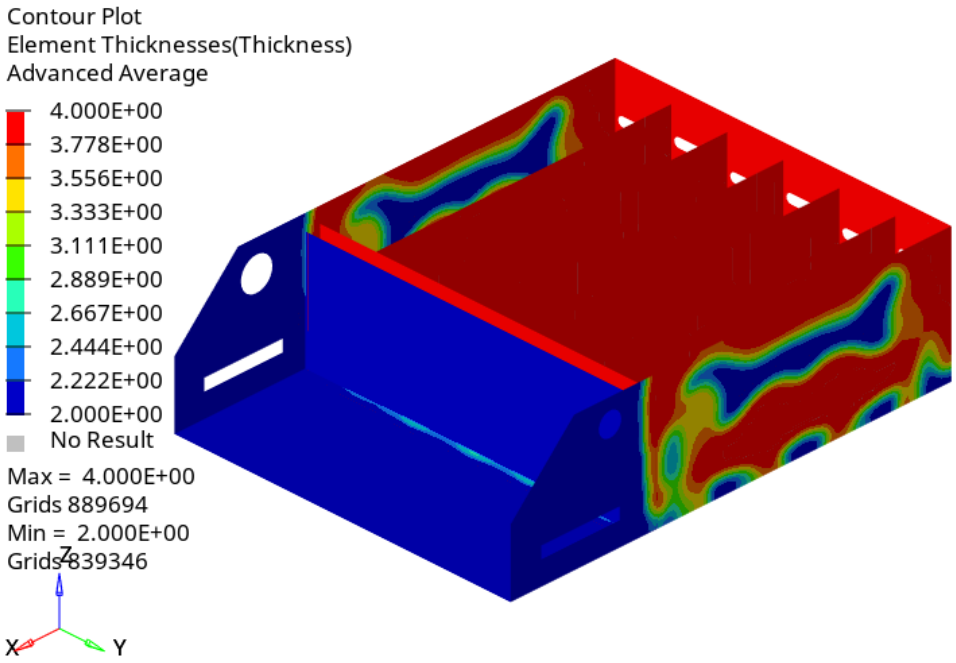

Figure 4.27: Bottom container free-sizing step element thickness.

Again, for example, the four shapes suggested for the 0-degree CFRP ply are shown in Figure 4.28.

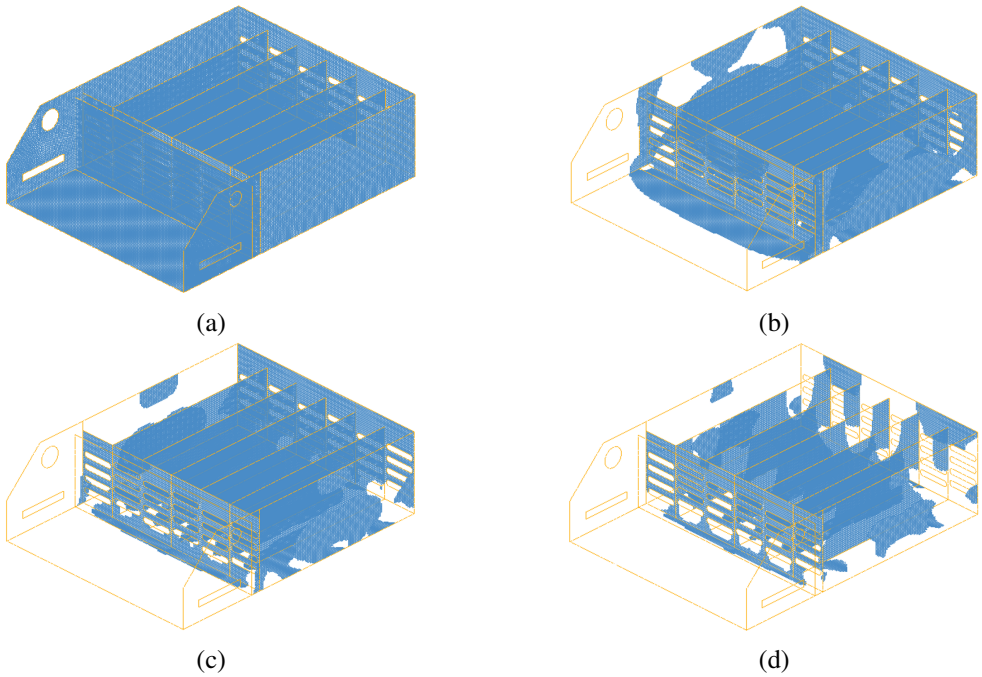

Figure 4.28: 0-degree CFRP ply reinforcement shapes according to load path after free-sizing for the bottom container: (a) main shape; (b) main reinforcement; (c) second reinforcement shape; (d) small reinforcement shape.

4.2.3.8 Continuous sizing

The process started again with adapting the shapes for manufacturable ones. One can use the simulations done for the mesh study and conclude that the used layup withstands the load cases pretty well. One could reduce the ply number but that would reduce the laminate thickness too much. Thus, one opted to maintain only two shapes: the laminate for the external walls and the laminate for the internal walls, due to isolation constraints. The two shapes are shown in Figure 4.29.

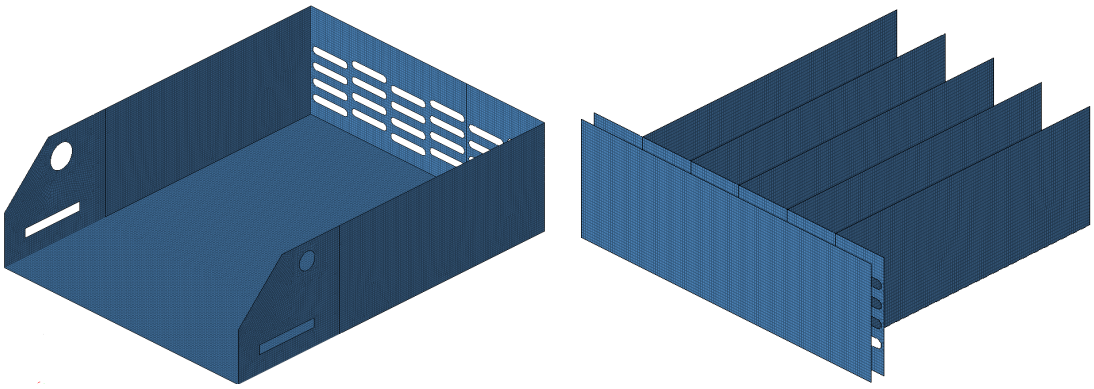

(a) (b)

Figure 4.29: Bottom container optimisation shapes: (a) External walls; (b) Internal walls.

As before, constraining the maximum ply thickness:

- **Aluminium:** 0.5 mm - only one ply;
- **CFRP base:** 0.422 mm - maximum two plies;
- **GFRP:** 0.5 mm - only one ply.

The major stress was also contrained to -750 MPa and 750 MPa to be in accordance with the material properties.

This phase converged after 2 iterations, with laminate thickness as shown in Figure 4.30. Note that although the laminate is different, the thickness is the same since the GFRP ply and the aluminium sheet have the same thickness.

The ply thickeness for each orientation and shape are shown in Table 4.17.

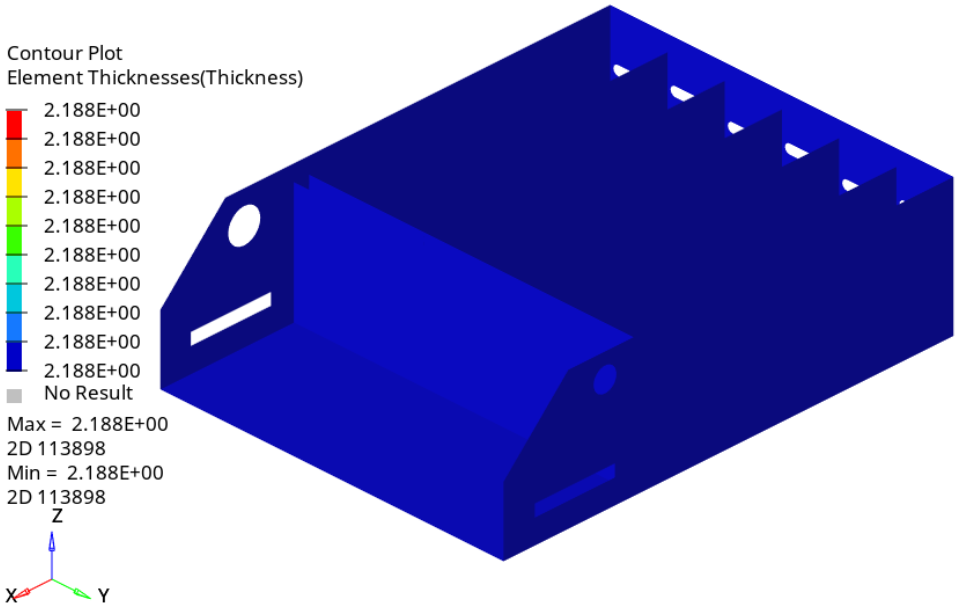

Figure 4.30: Bottom container element thickness after continuous sizing.

Table 4.17: Lid ply thickness after continuous sizing.

Material	**Orientation** [°]	**Shape**	**Thickness [mm]**
Aluminium	0	External walls	0.500
GFRP	0	Internal walls	0.500
CFRP	0	Whole model	0.422
CFRP	45	Whole model	0.422
CFRP	-45	Whole model	0.422
CFRP	90	Whole model	0.400
GFRP	0	Whole model	0.000

Table 4.18: Lid ply thickness after discrete sizing.

Ply	**Material**	**Orientation** [°]	**Shape**	**Thickness [mm]**
1	**Aluminium**	0	External walls	0.5
2	**GFRP**	0	Internal walls	0.5
3	**CFRP**	0	Whole model	0.211
4	**CFRP**	0	Whole model	0.211
5	**CFRP**	45	Whole model	0.211
6	**CFRP**	45	Whole model	0.211
7	**CFRP**	-45	Whole model	0.211
8	**CFRP**	-45	Whole model	0.211
9	**CFRP**	90	Whole model	0.211
10	**CFRP**	90	Whole model	0.211

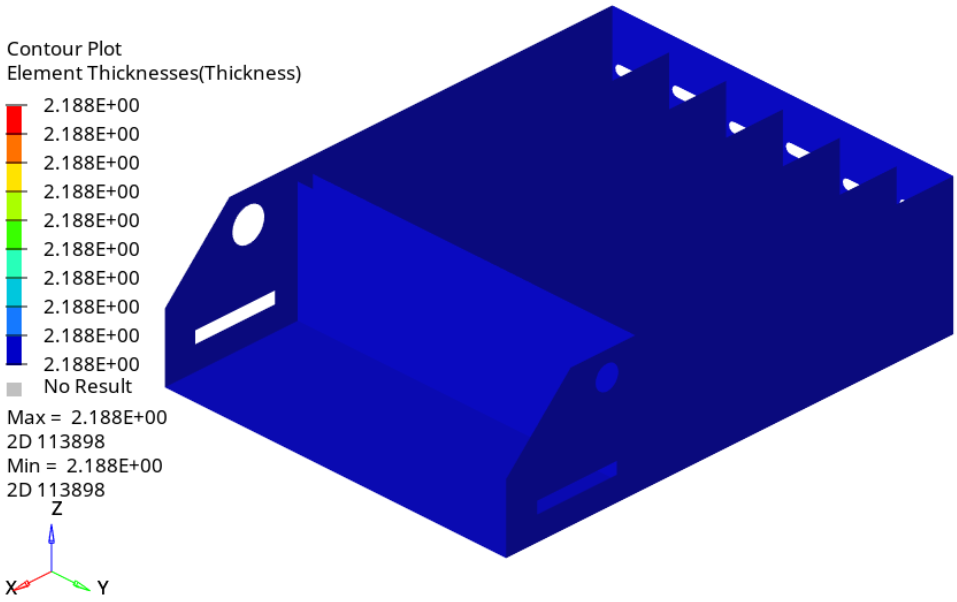

Figure 4.31: Bottom container element thickness after discrete sizing.

4.2.3.9 Discrete sizing

By applying the same ply thicknesses as for the lid, it was possible to do the discrete sizing simulation, which converged after 2 iterations and resulted in the plies defined in Table 4.18.

The element thickness is shown in Figure 4.31.

Note that the internal GFRP ply was suppressed during these phases since it is not significant to the laminate mechanical properties. However, this ply is crucial for the electrical isolation of the laminate. Thus, the ply was manually added again before the shuffling phase.

4.2.3.10 Shuffling

The same procedure as the lid shuffling was followed. After 4 iterations the simulation converged and gave the layup shown in Figure 4.32.

Iteration 0	Iteration 1	Iteration 2	Iteration 3	Iteration 4
6101	6101	6101	6101	6101
2101	3101	5102	2101	3101
2102	4101	2101	5101	4101
3101	2101	5101	3101	2101
3102	5101	3101	4101	5101
4101	8101	4101	8101	8101
4102	3102	8101	2102	3102
5101	4102	2102	5102	4102
5102	2102	3102	3102	2102
8101	5102	4102	4102	5102
1101	1101	1101	1101	1101

Legend
30.0 degrees
90.0 degrees
-45.0 degrees
45.0 degrees
0.0 degrees
40.0 degrees

Figure 4.32: Bottom layup shuffling iterations.

The layup suggestion is summarised in Table 4.19.

Table 4.19: Lid layup after shuffling.

Ply	Material	Orientation [°]	Shape	Thickness [mm]
1	**GFRP**	0	Whole model	0.500
2	**CFRP**	45	Whole model	0.211
3	**CFRP**	-45	Whole model	0.211
4	**CFRP**	0	Whole model	0.211
5	**CFRP**	90	Whole model	0.211
6	**GFRP**	0	Internal walls	0.500
7	**CFRP**	45	Whole model	0.211
8	**CFRP**	-45	Whole model	0.211
9	**CFRP**	0	Whole model	0.211
10	**CFRP**	90	Whole model	0.211
11	**Aluminium**	0	External walls	0.500

The displacement and Tsai-Wu index are shown in Figure 4.33.

4.2.3.11 Analysis

Note that although both the displacement and Tsai-Wu failure index are not high, there are a few problems. First, the inner laminate is not symmetric but a repetition. Then, the GFRP ply is placed in the middle of the laminate instead of its top. Thus, it is necessary to re-order the laminate, as shown in Table 4.20.

Table 4.20: Bottom container layup after reordering.

Ply	Material	Orientation [°]	Shape	Thickness [mm]
1	**GFRP**	0	Whole model	0.500
2	**CFRP**	0	Whole model	0.211
3	**CFRP**	45	Whole model	0.211
4	**CFRP**	-45	Whole model	0.211
5	**CFRP**	90	Whole model	0.211
6	**CFRP**	90	Whole model	0.211
7	**CFRP**	-45	Whole model	0.211
8	**CFRP**	45	Whole model	0.211
9	**CFRP**	0	Whole model	0.211
11	**GFRP**	0	Internal walls	0.500
11	**Aluminium**	0	External walls	0.500

The new results are shown in Figure 4.34, with a final weight of 4.51 kg.

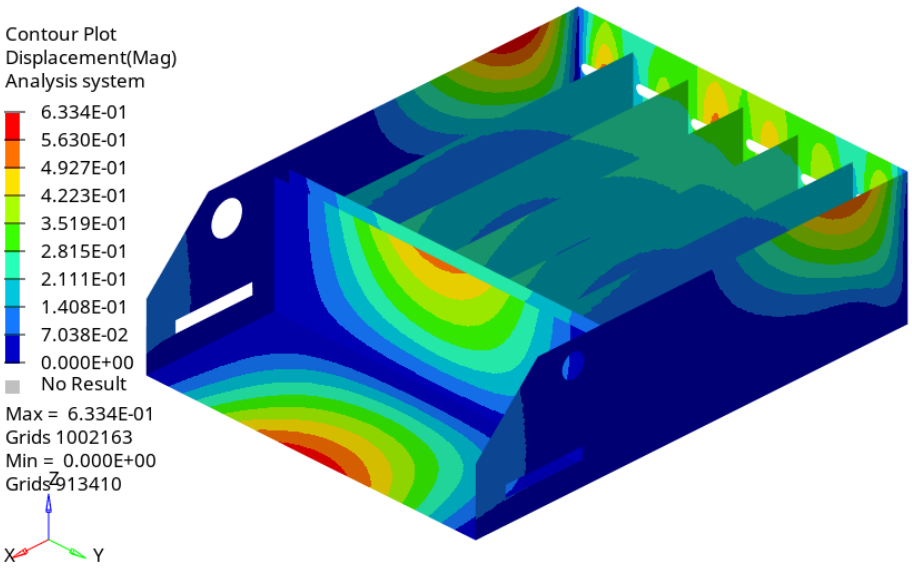

(a) displacement field for a 40g front-to-back longitudinal acceleration;

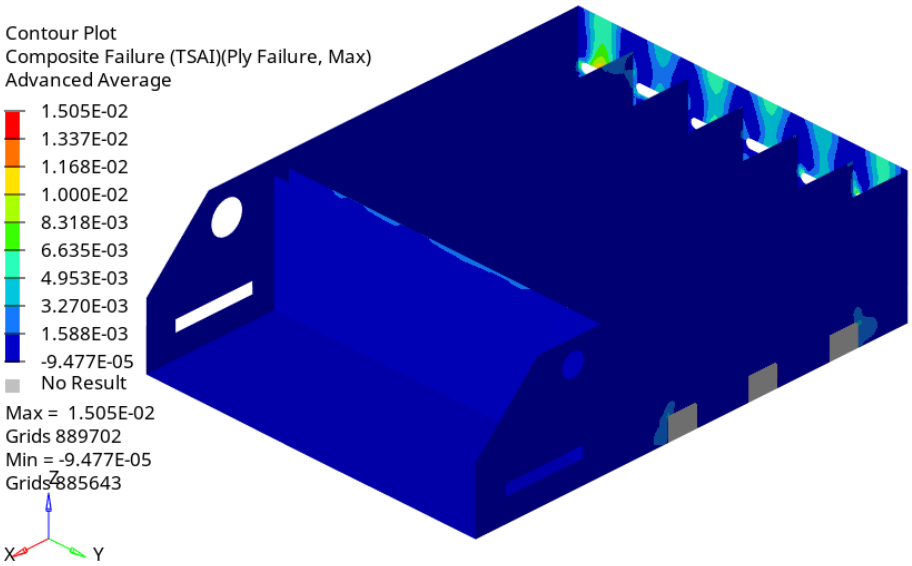

(b) Tsai-Wu failure index for a 40g front-to-back longitudinal acceleration;

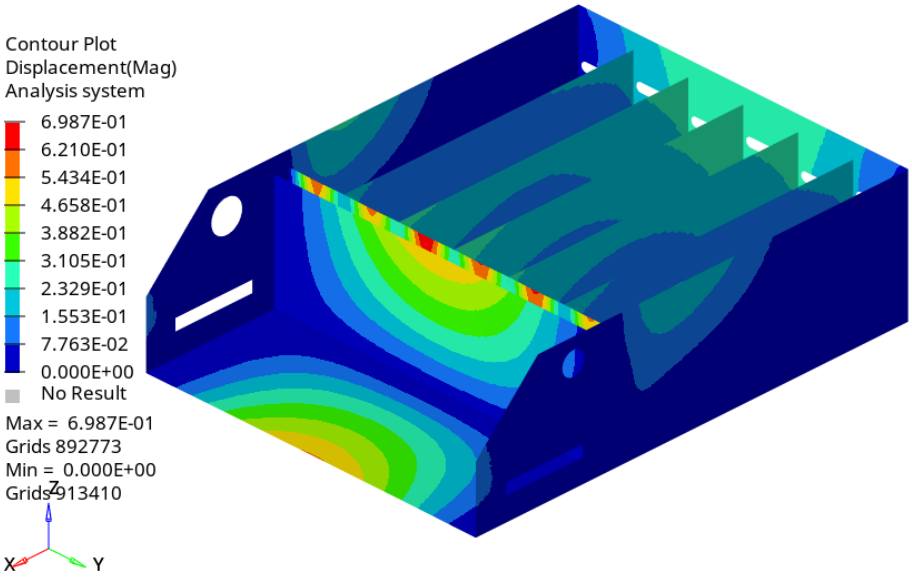

(c) displacement field for a 40g back-to-front longitudinal acceleration;

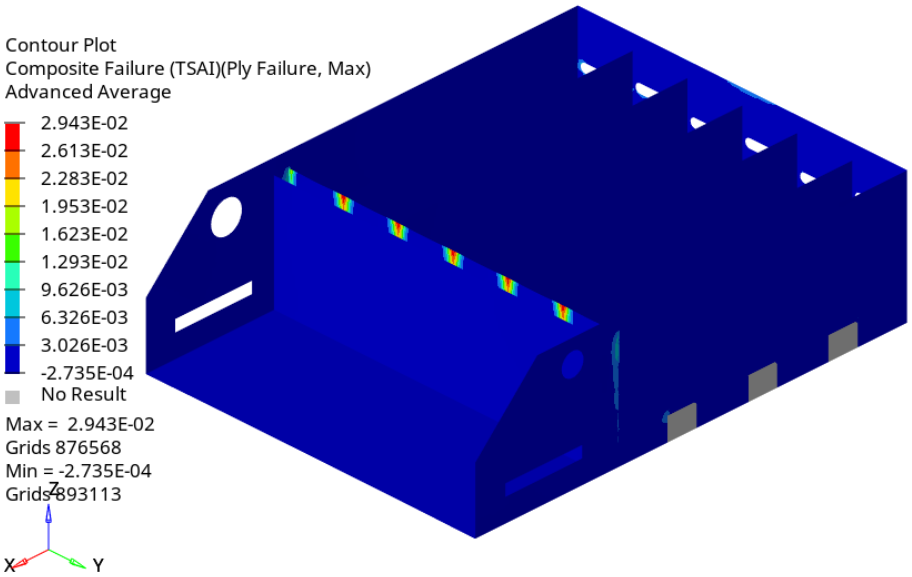

(d) Tsai-Wu failure index for a 40g front-to-back longitudinal acceleration;

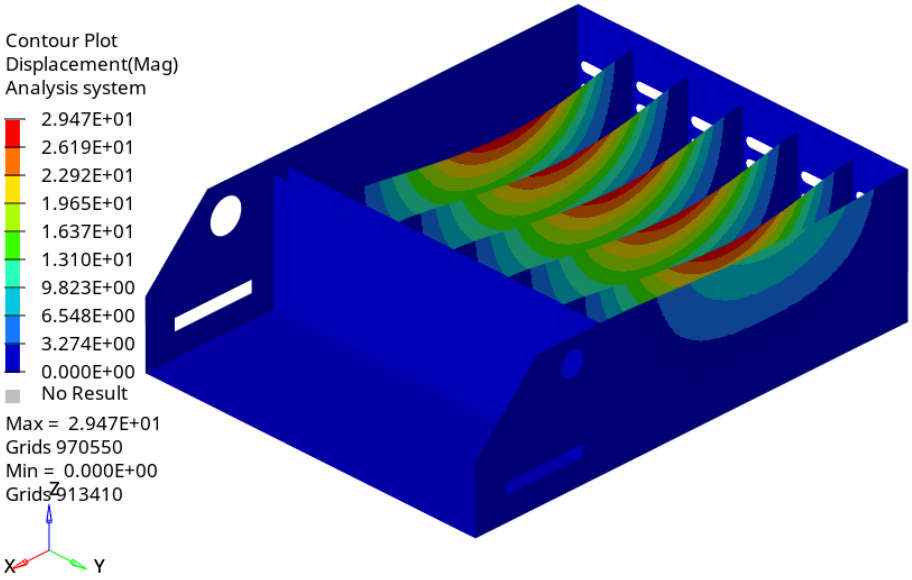

(e) displacement field for a 40g left-to-right tranversal acceleration;

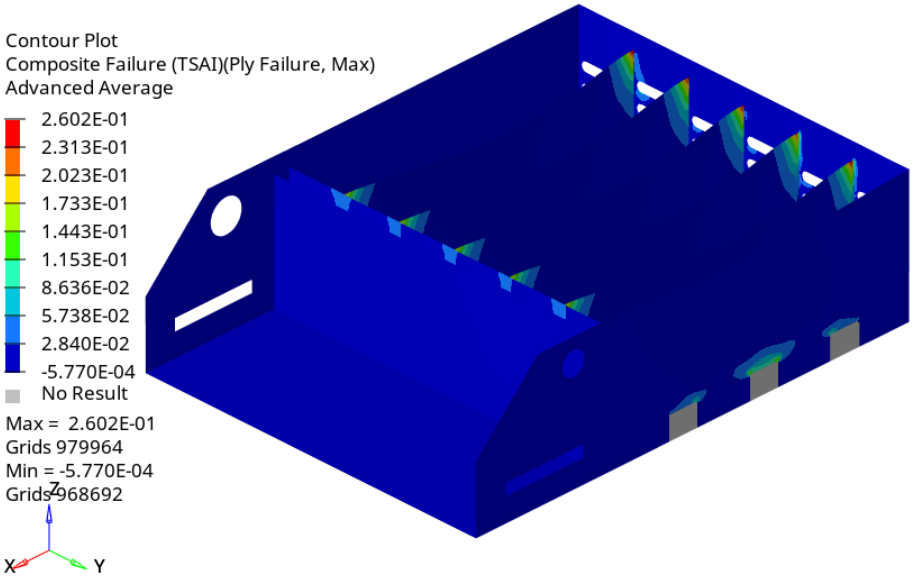

(f) Tsai-Wu failure index for a 40g left-to-right transversal acceleration;

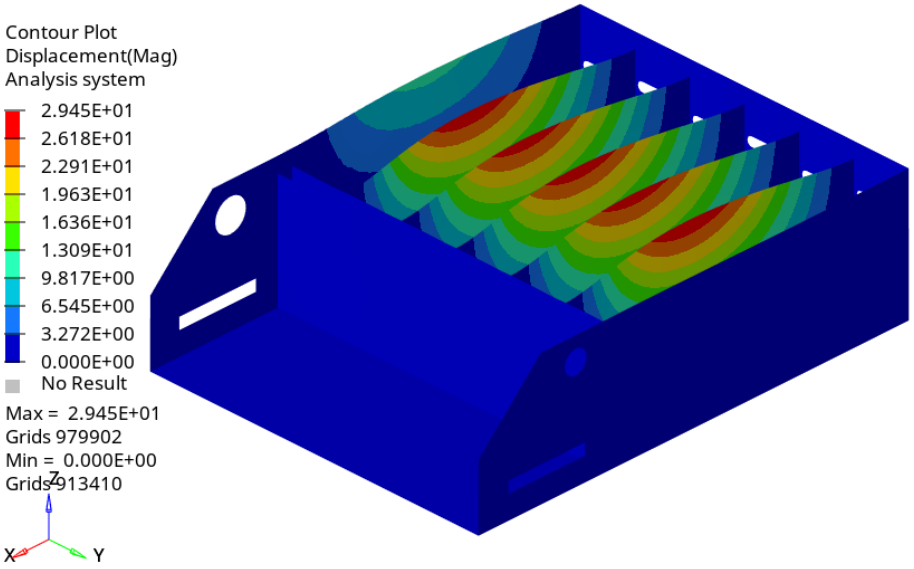

(g) displacement field for a 40g right-to-left tranversal acceleration;

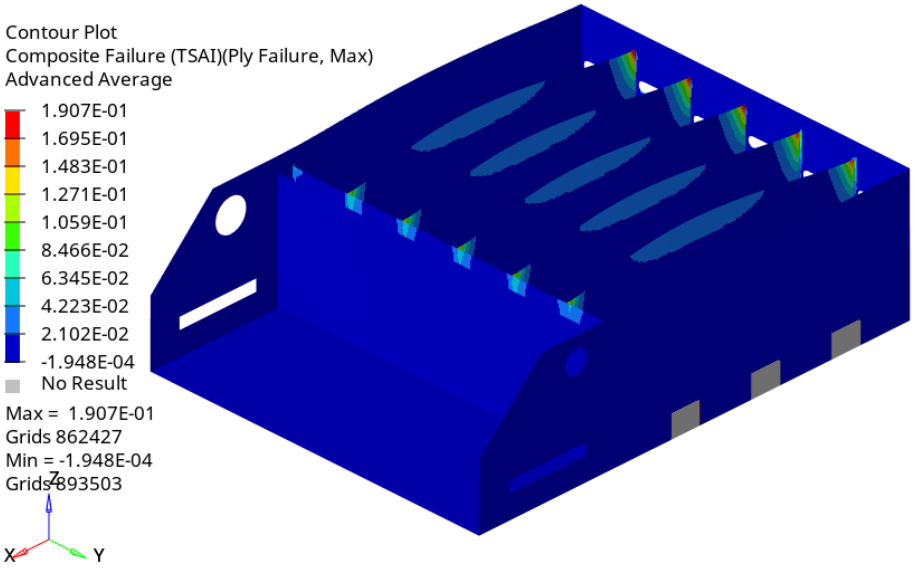

(h) Tsai-Wu failure index for a 40g right-to-left transversal acceleration;

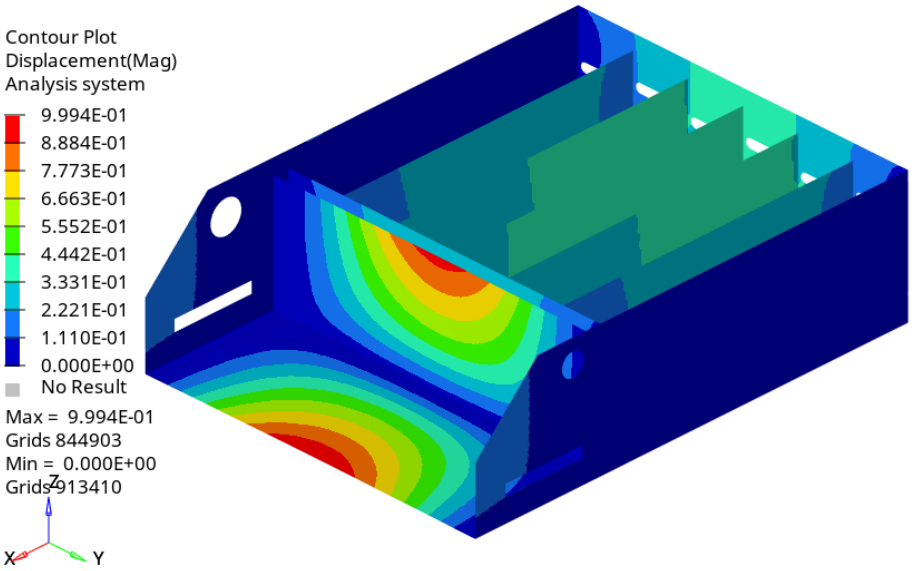

(i) displacement field for a 20g vertical acceleration;

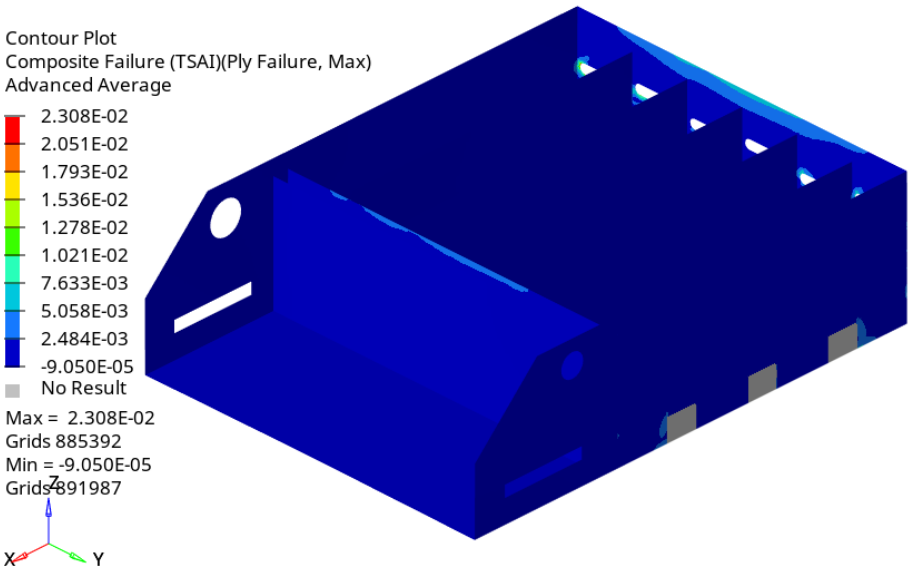

(j) Tsai-Wu failure index for a 20g vertical acceleration.

Figure 4.33: Shuffling results bottom container .

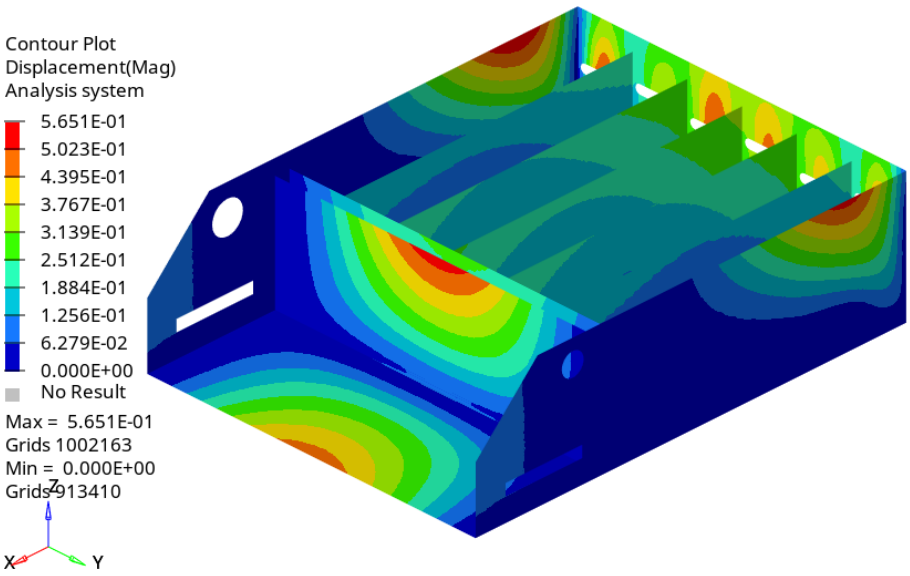

(a) displacement field for a 40g front-to-back longitudinal acceleration;

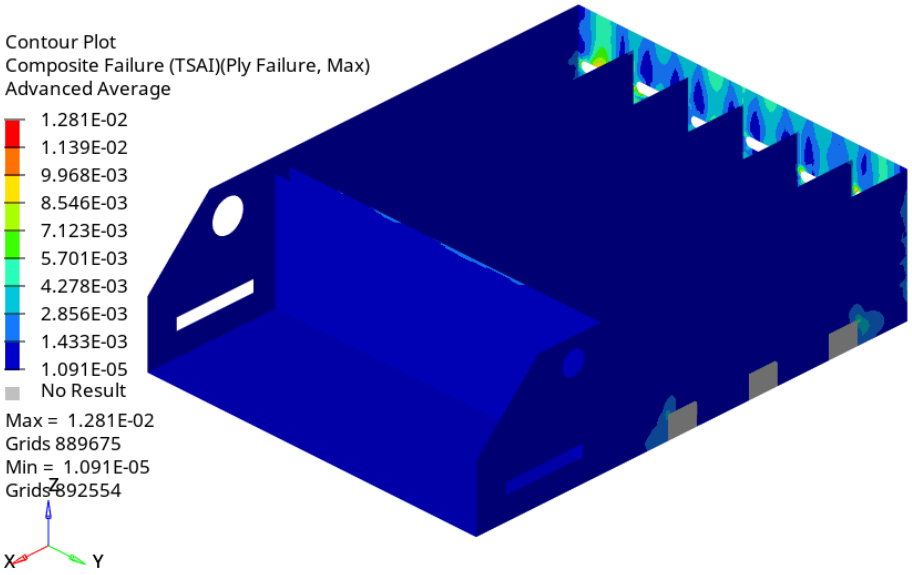

(b) Tsai-Wu failure index for a 40g front-to-back longitudinal acceleration;

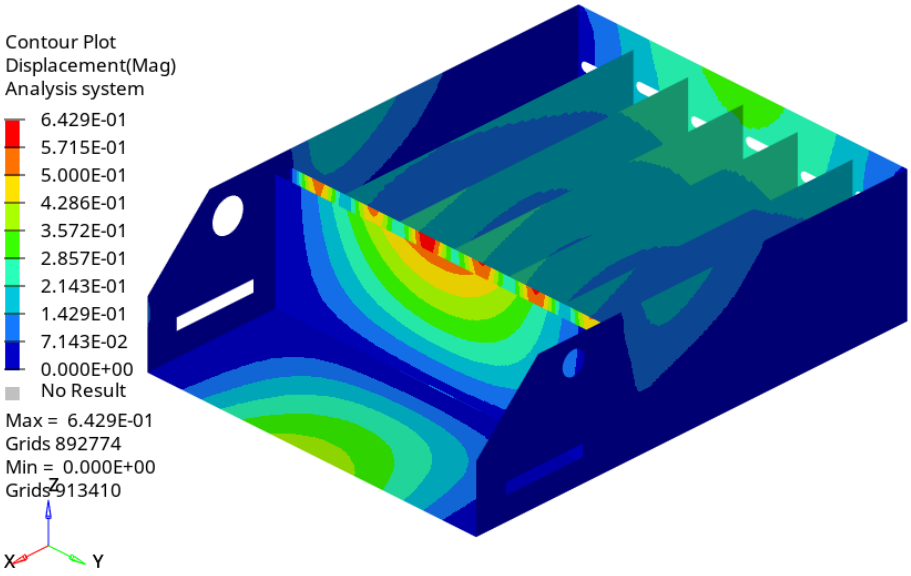

(c) displacement field for a 40g back-to-front longitudinal acceleration;

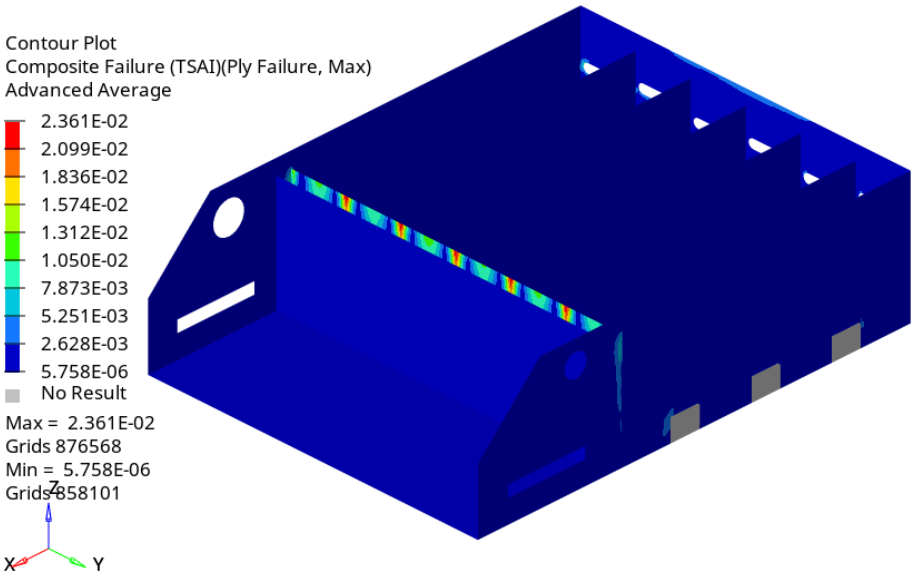

(d) Tsai-Wu failure index for a 40g front-to-back longitudinal acceleration;

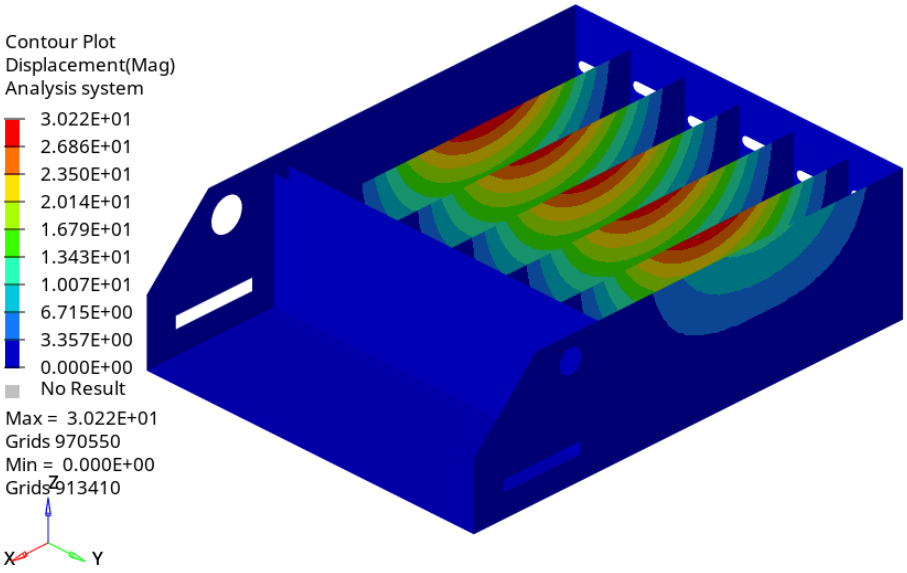

(e) displacement field for a 40g left-to-right tranversal acceleration;

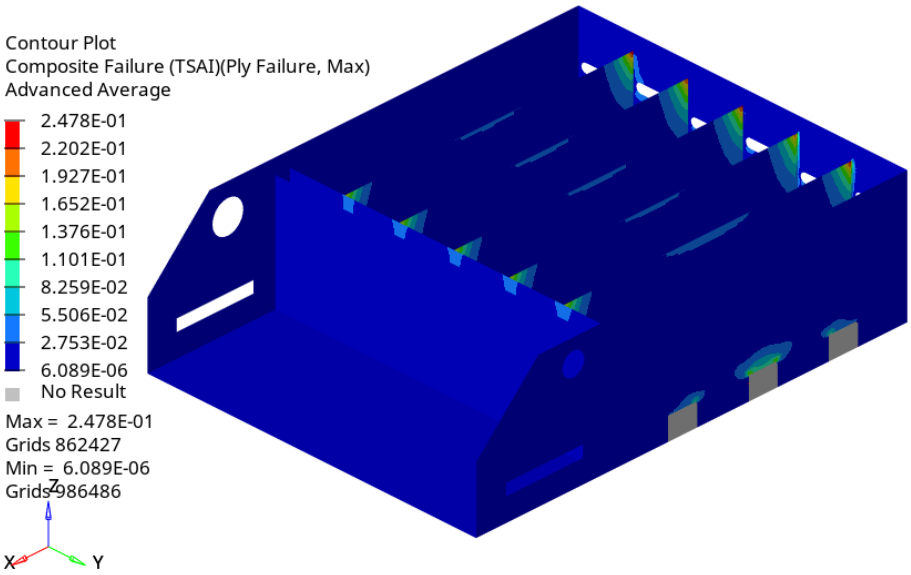

(f) Tsai-Wu failure index for a 40g left-to-right transversal acceleration;

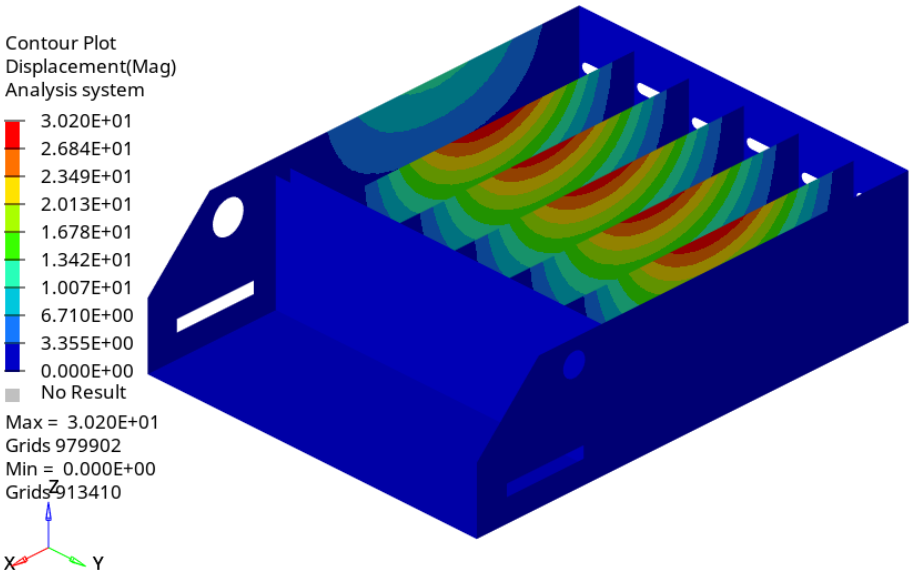

(g) displacement field for a 40g right-to-left tranversal acceleration;

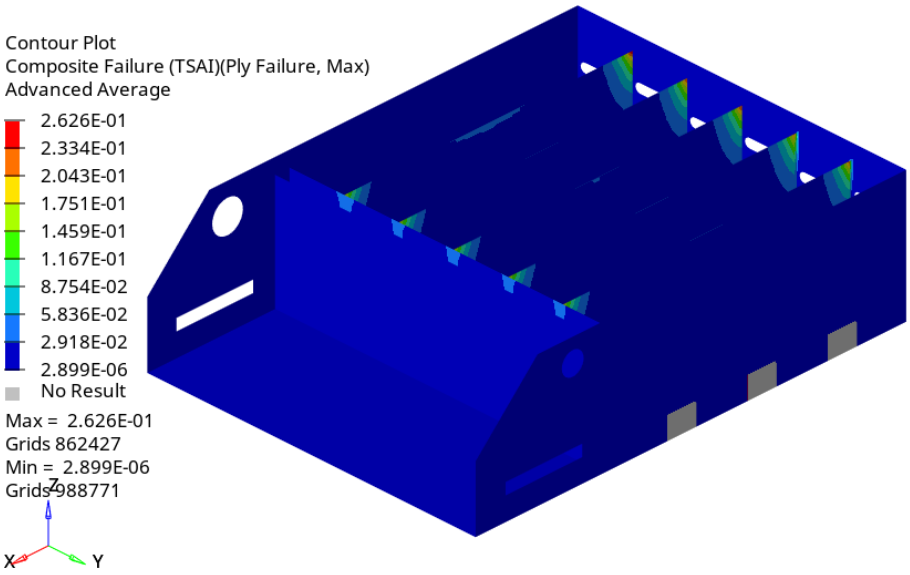

(h) Tsai-Wu failure index for a 40g right-to-left transversal acceleration;

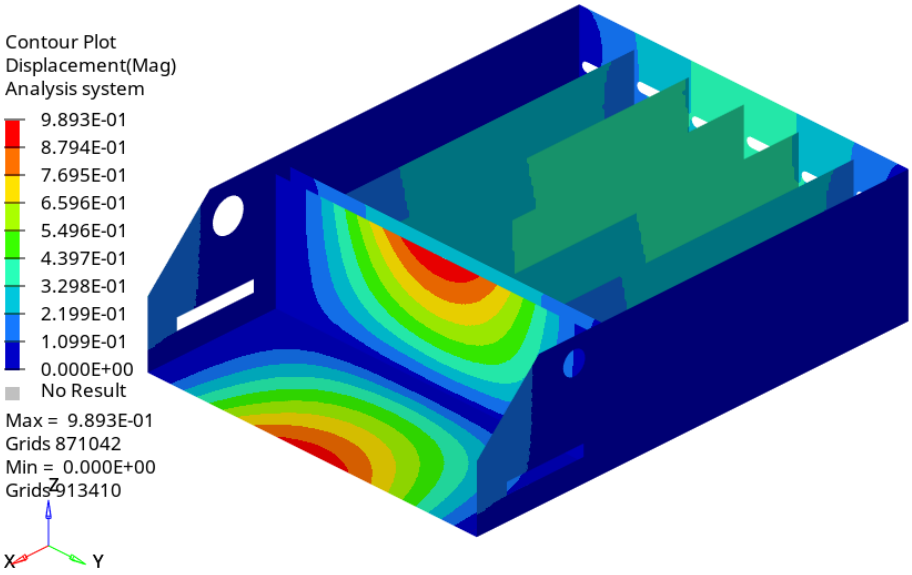

(i) displacement field for a 20g vertical acceleration;

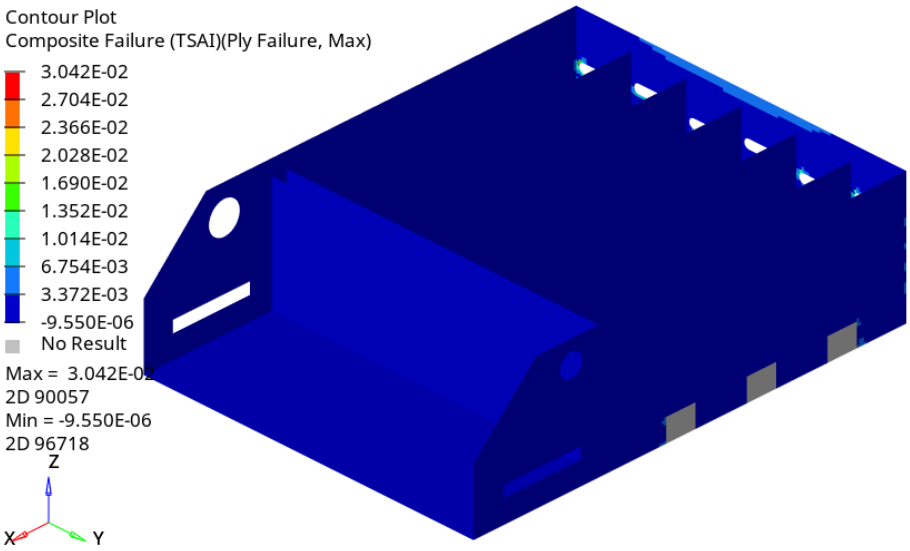

(j) Tsai-Wu failure index for a 20g vertical acceleration.

Figure 4.34: Final results bottom container.

Chapter 5

Design validation

It is necessary to perform and analyse experimental testing of the material to validate the design and simulations. Thus, this chapter will present all the tests and analyses done: three-point bending, four-point bending and perimeter shear strength.

5.1 Material selection

Although the design chosen material was TC346 FA/256 193gsm PW T700SC 12K 38% RW, this material was not immediately available for testing. Thus, it was decided to validate the process and the tools developed in this study by testing the Toray E745/IM7 pre-preg, with properties as listed in Table 5.1.

Table 5.1: Carbon fibre pre-preg Toray E745/IM7 properties (Dalli et al., 2020).

Material property	**Symbol [units]**	**Value**
Density	$\rho[kg/m^3]$	1504.8
In-plane tensile elastic moduli	$E_1^T = E_2^T$ [GPa]	63.6
In-plane compressive elastic moduli	$E_1^C = E_2^C$ [GPa]	61.0
In-plane tensile Poisson's ratio	ν_{12}^T [-]	0.03
In-plane compressive Poisson's ratio	ν_{12}^C [-]	0.03
Shear modulus	G_{12} [GPa]	3.69
In-plane tensile strengths	$X_t = Y_t$ [MPa]	1046
In-plane compressive strengths	$X_c = Y_c$ [MPa]	595
Shear strength	S_{12} [MPa]	100

5.2 Manufacturing

For testing purposes, two plates of 330x330 mm with 8 plies each of layup $[0/45/-45/90]_S$ were manufactured. Due to the small number, the plates were done by hand layup of the prepreg.

The process started by cutting the shapes with the respective orientation, as shown in Figure 5.1.

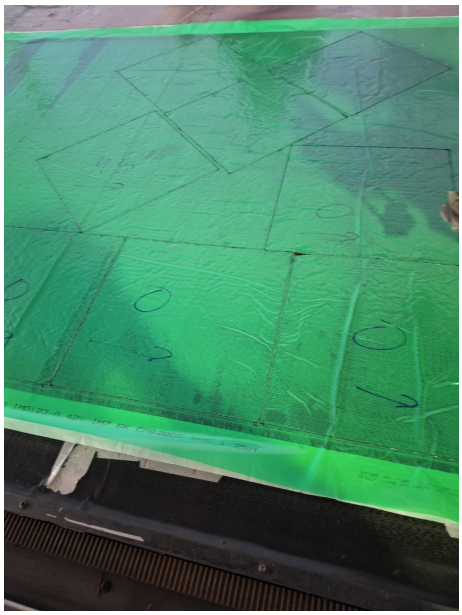

Figure 5.1: Prepeg nesting and cutting pattern.

After cutting the shapes, the next step was to carefully stack the laminate, while keeping the ply orientation, as seen in Figure 5.2.

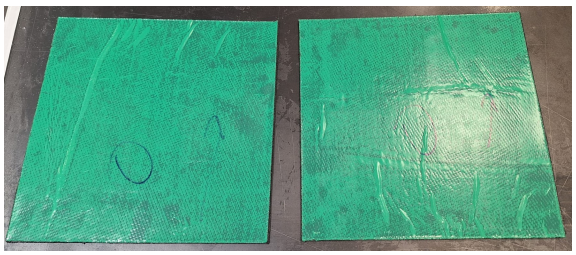

Figure 5.2: Stacked plies, forming the two plates.

After layup, a layer of teflon film is placed in either side of the plate and, subsquently, two layers of breather cloth on both sides. Subsequently, the assembly is bagged and placed under vaccum to confirm the absence of vacum leaks on the bag, as shown in Figure 5.3. Finnaly, a 8 mm-thick aluminium caul plate is place either side of the plate to ensure uniform pressure distribution on the surface, as seen in Figure 5.4.

Then, the plates were cured in an autoclave at a pressure of 6 bar and a temperature of 125°C. The log is shown in Figure 5.5. After cure, the caul plates were removed and the plates ended up as Figure 5.6 shows.

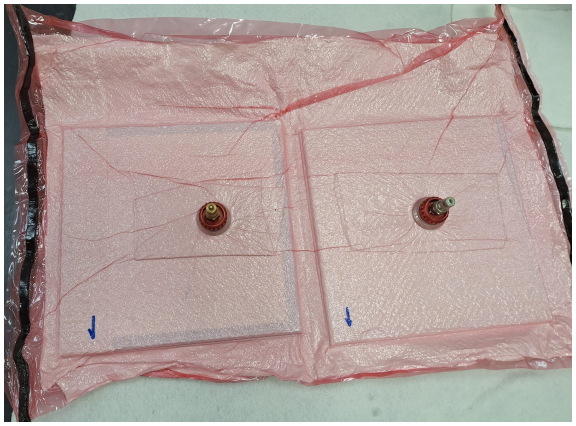

Figure 5.3: Plates inside the vacuum bag.

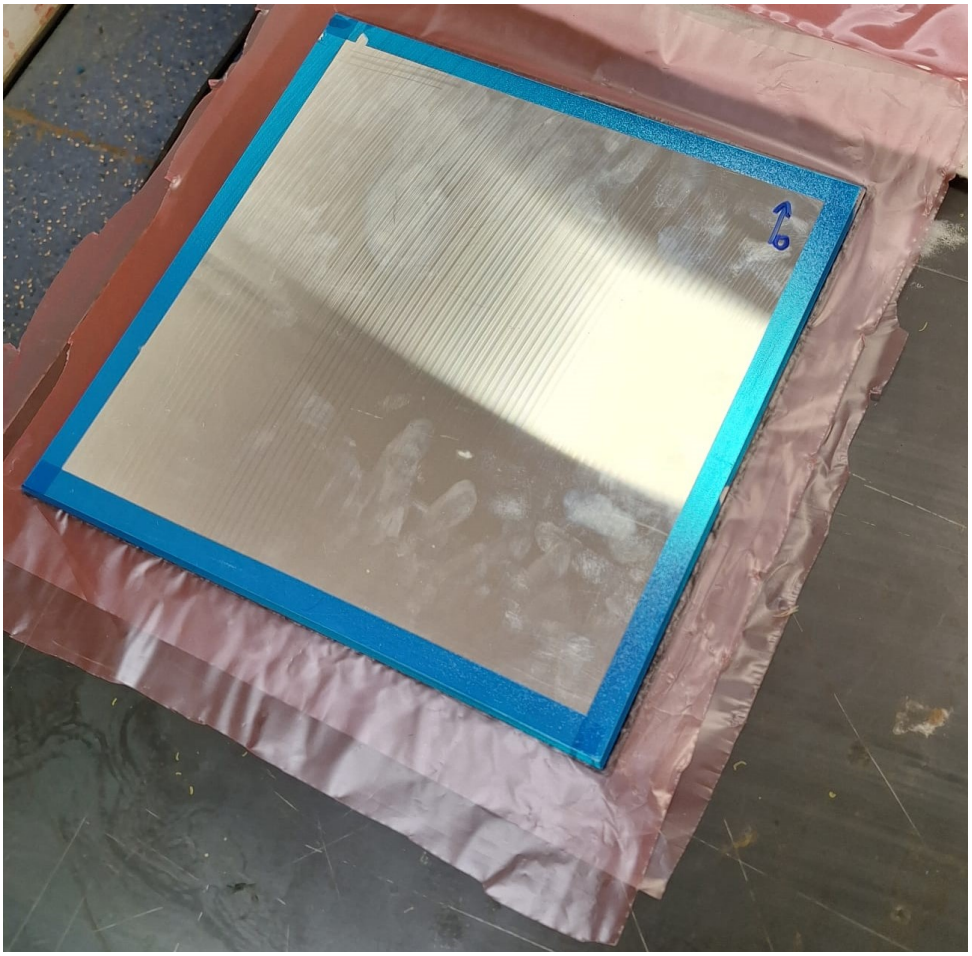

Figure 5.4: Stacked plies, forming the two plates.

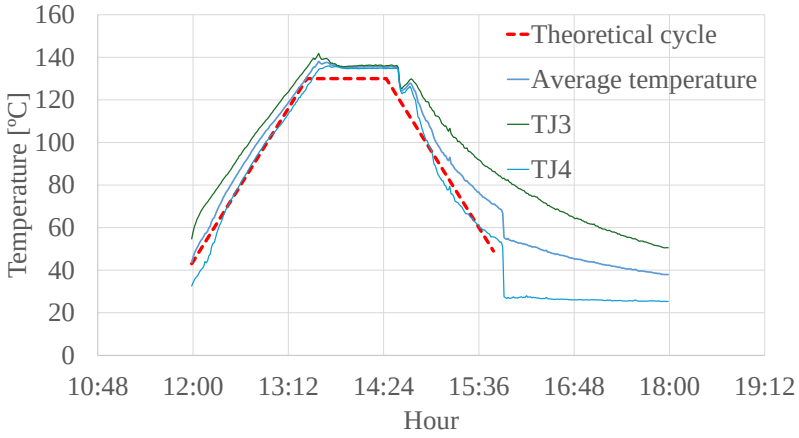

(a)

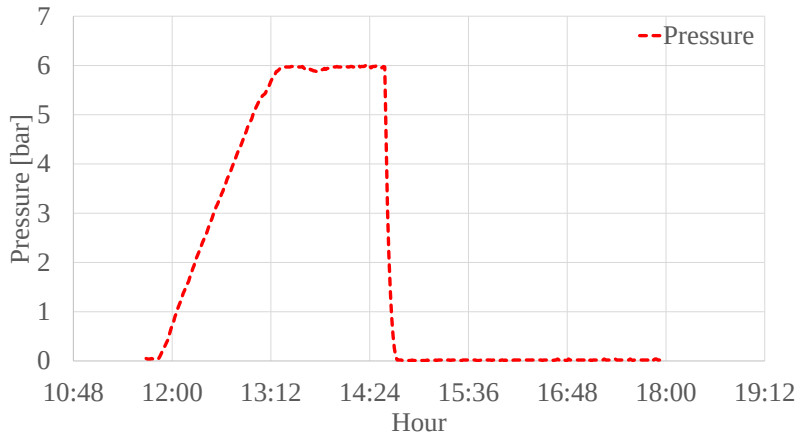

(b)

Figure 5.5: Manufacturing log: (a) temperature; (b) pressure.

Figure 5.6: Plates after the curing process.

5.3 Specimen geometry

After the curing process, a total of six specimens for each test were cut using a diamond-edge wet saw. All the specimens were measured, to consider the average dimensions of each, as shown in Table 5.2.

Table 5.2: Specimen dimensions.

Specimen	Length [mm]	Width [mm]	Thickness [mm]	Average [mm]
	99.90	13.05	2.50	
3PB1	99.95	13.05	2.55	99.92 × 13.05 × 2.53
	99.90	13.05	2.55	
	99.90	13.20	2.55	
3PB2	99.90	13.30	2.55	99.90 × 13.25 × 2.55
	99.90	13.25	2.55	
	99.50	13.15	2.50	
3PB3	99.55	13.10	2.55	99.53 × 13.22 × 2.53
	99.55	13.10	2.55	
	99.80	13.15	2.55	
3PB4	99.90	13.10	2.55	99.87 × 13.12 × 2.55
	99.90	13.10	2.55	
	99.88	13.25	2.55	
3PB5	99.90	13.25	2.55	99.90 × 13.25 × 2.55
	99.85	13.25	2.55	
	99.40	13.05	2.55	
3PB6	99.40	13.20	2.55	99.40 × 13.13 × 2.55
	99.40	13.15	2.55	
	100.00	13.05	2.55	
4PB1	100.00	13.10	2.55	100.00 × 13.07 × 2.55
	100.00	13.05	2.55	
	99.90	13.30	2.55	
4PB2	99.90	13.10	2.55	99.90 × 13.20 × 2.55
	99.90	13.20	2.55	
	99.95	13.45	2.55	
4PB3	100.00	13.40	2.55	99.97 × 13.42 × 2.55
	99.90	13.40	2.55	
	100.00	13.30	2.60	
4PB4	99.95	13.30	2.55	99.95 × 13.32 × 2.57
	99.90	13.35	2.55	
	99.85	13.35	2.55	
4PB5	99.85	13.40	2.55	99.87 × 13.38 × 2.55
	99.90	13.40	2.55	
	99.80	13.00	2.55	
4PB6	99.90	12.95	2.55	99.85 × 12.97 × 2.55
	99.85	12.95	2.55	

5.4 Testing

All the following tests were performed using an Instron machine and following the respective standards. Note that only 5 specimens of each test were tested.

5.4.1 Three-point bending

5.4.1.1 Test setup

The test dimensions followed the ASTM D7264 standard and had the dimensions shown in Table 5.3. Figure 5.7 shows the test setup.

Table 5.3: Three-point bending testing dimensions.

Dimension [units]	**Value**
Specimen thickness [mm]	2.55
Specimen width [mm]	13
Specimen length [mm]	100
Span [mm]	80

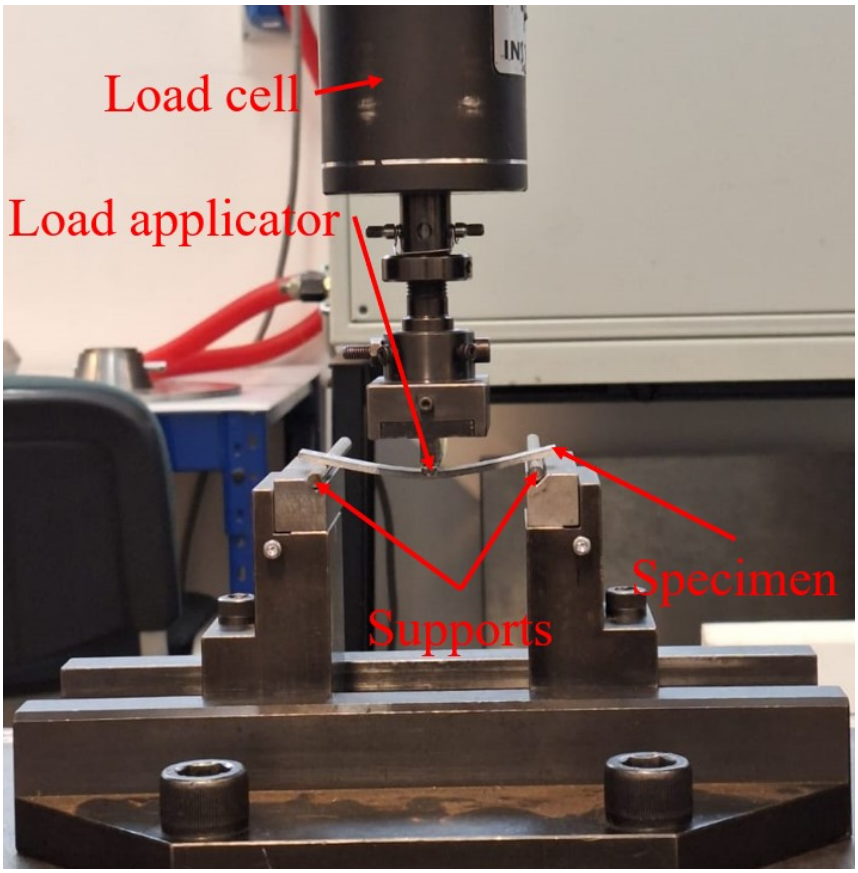

Figure 5.7: Three-point test setup.

5.4.1.2 Results and analysis

The results for each specimen are shown graphically in Figure 5.8, and the data, including ultimate flexural strength, calculated by Equation (2.28), flexural modulus, Equation (2.29), and ultimate strain, Equation (2.30), are presented in Table 5.4.

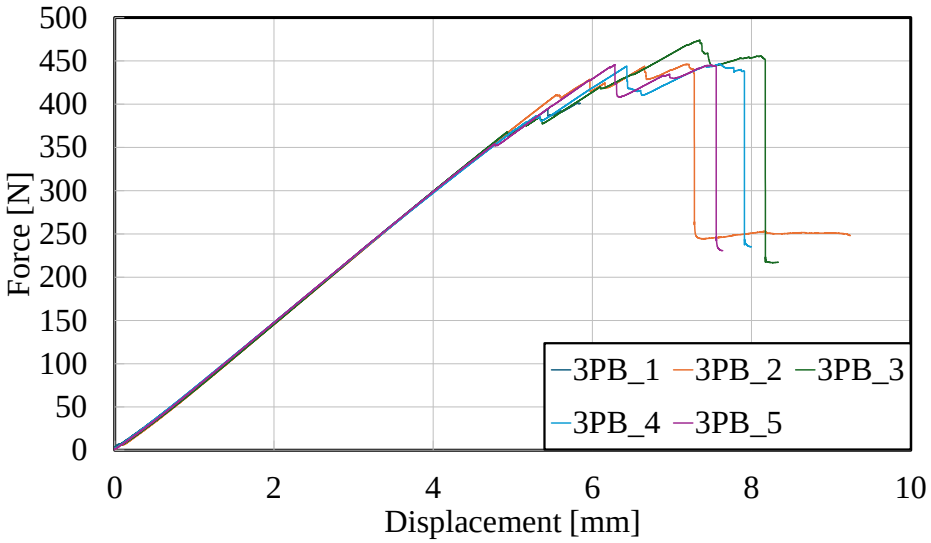

Figure 5.8: Three-point bending results.

Table 5.4: Three-point bending results.

Value [units]	3PB_1	3PB_2	3PB_3	3PB_4	3PB_5
Ultimate displacement [mm]	5.85	9.24	8.33	8.00	7.64
Average [mm]			7.82		
Standard deviation [mm]			1.25		
C.o.V [%]			16.0		
Ultimate load [N]	401.5	446.2	474.0	446.7	445.6
Average [N]			443.0		
Standard deviation [N]			0.03		
C.o.V [%]			5.9		
Ultimate flexural strength [MPa]	589.7	637.0	687.4	644.2	636.1
Average [MPa]			638.8		
Standard deviation [MPa]			34.7		
C.o.V [%]			5.4		
Flexural modulus [GPa]	48.34	46.68	47.73	47.16	46.68
Average [GPa]			47.32		
Standard deviation [GPa]			0.72		

C.o.V [%]			1.5		
Maximum strain [-]	0.0132	0.0210	0.0188	0.0182	0.0174
Average [-]			0.0177		
Standard deviation [-]			0.003		
C.o.V [%]			16.2		

In addition, the modelled test previously done is tested and the needed constants were refined and analysed to see which failure criteria better suits the curve. Starting with the maximum stress, maximum strain, Tsai-Hill and Tsai-Wu failure criteria, where the damage is modelled by evenly reducing stiffness, a study was conducted varying the damage parameter between 0.07, 0.1 and 0.14. The results are shown in Figure 5.9.

The first visible aspect is that the determined stiffness of the model is in good agreement with the one obtained during the tests. Note that this first part of the curve is equal in every case since in this part, the composite did not fail yet and the code is independent of the failure criteria and damage variable used.

Another common element is that in all failure criteria, in general, when the first ply fails, there is a sharp load drop that does not occur in the experimental testing. Note that the higher the damage parameter, the smaller the drop is. This happens because with higher parameters comes a lower stiffness drop. It can also be seen that with increasing damage parameters, the model predicts failure at higher loads and displacement. Once again, this is due to the increased damaged stiffness considered when a ply fails.

In addition, one can note that all the failure criteria predict failure sooner than it occurs in the experimental testing. This means that all the failure criteria are conservative. By analysing the first ply failure results for each model, one can notice that some models are omre conservative than others. This can be seen in Table 5.5.

Table 5.5: First ply failure data for every failure criteria.

Failure criteria	**Discplacement [mm]**	**Load [N]**
Maximum stress	4.60	329.5
Maximum stain	4.50	322.3
Tsai-Hill	4.10	293.6
Tsai-Wu	4.40	315.1

It can be noted that, for the first ply failure, the most conservative criterion is the Tsai-Hill, while the others are very similar among themselves, with the maximum stress criterion being slightly less conservative.

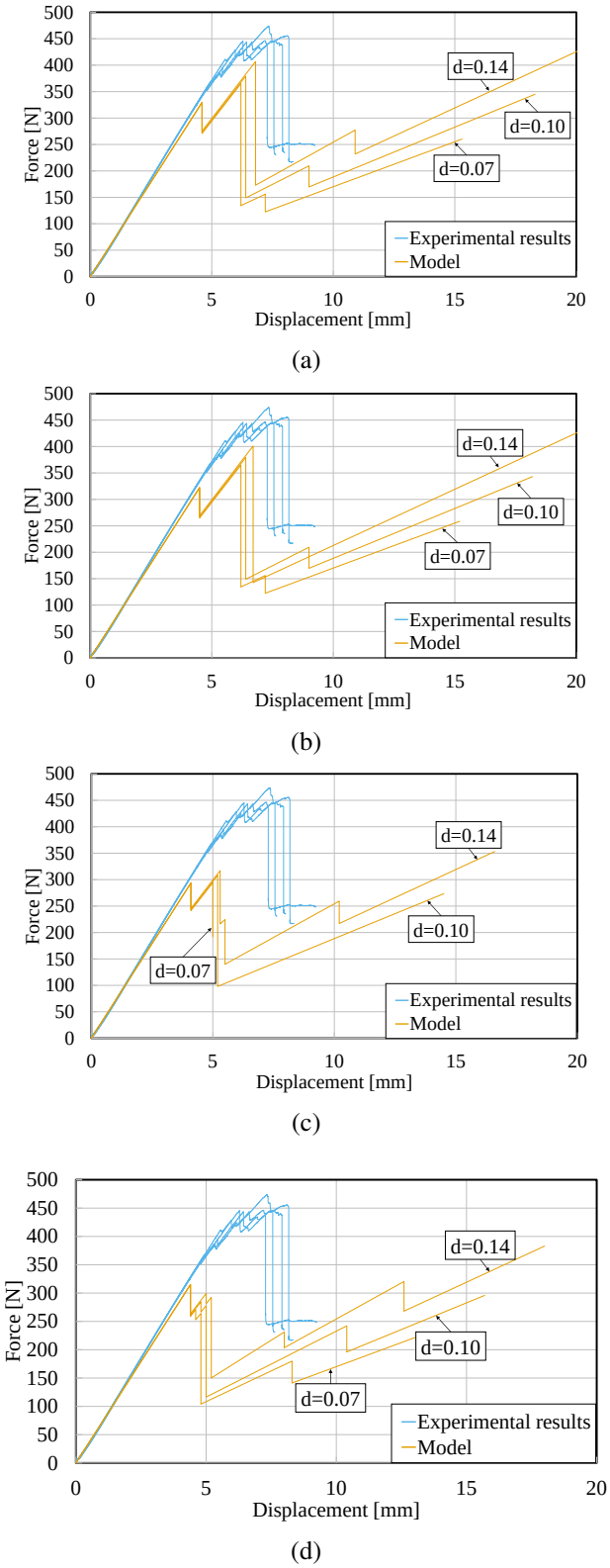

Figure 5.9: Damage variable study with different failure criteria: (a) maximum stress; (b) maximum strain; (c) Tsai-Hill; (d) Tsai-Wu.

One can also note that the maximum stress and maximum strain criteria are the ones that best match the experimental results, with the Tsai-Wu criterion not following that trend.

Now, focusing on the first part of the test, that is, until the first major load drop, one can see that the curve that is closer to the experimental data is the one with $d = 0.14$. However, in the second part of the test, there are considerable differences off stiffness and in load-displacement curve. This happens due to the fact that the stiffness reduction in these models does not take into consideration the type of failure of the ply and it reduces the stiffness equally for all failed plies. However, there are different parameters for ply failures in tension and compression that are not taken into account by these models.

This is why the Hashin failure criterion is applied to woven prepregs. Since the damage parameters are already experimentally determined, such as $d_1^T = 0.07$, $d_2^T = d_6^T = 0.2$, $d_1^C = 0.14$ and $d_2^C = d_6^C = 0.4$ (Melo et al., 2011), only the parameters that control the influence of the shear stress in the failure criterion were studied. By changing α_t and α_c, one is changing the contribution of the shear loads in the failure criteria. By raising these parameters, the failure criterion is increased, heredy decreasing the expected loads. This study is shown in Figure 5.10 for the adapted Hashin failure criteria.

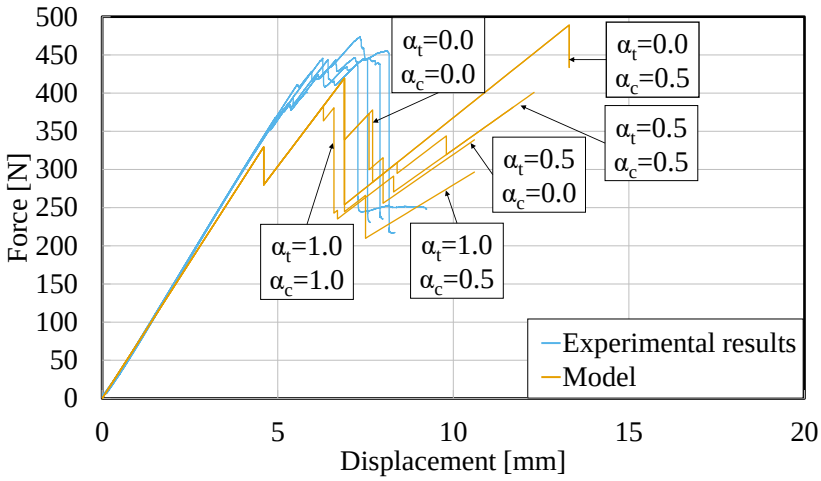

Figure 5.10: Shear stress contribution for the adapted Hashin failure criteria.

Starting with the zone until the first ply failure, as noticed in the previous failure criteria, the calculated stiffness is not far from the experimental one. Note that the first ply failure also occurs at the same point in all the cases. This means that, in this specific case, the first ply failure point is independent of the parameters.

The first difference in the curves happens in the second ply failure point, as for the $\alpha_t = \alpha_c = 1.0$ case, this failure occurs sooner than the other cases, as expected. In general, this curve is lower than the other ones.

The second major difference is that, although the second ply failure occurs at the same point, there is a disparity in the load drop for different cases. This comes as a consequence of the change in the failure criterion. While in some cases only one ply fails in that drop, in other cases more plies

are failing. The more significant the load drop, the more plies fail. It is also possible to correlate the failed ply number with the strength of the failure criteria. The lower drop corresponds to the cases $\alpha_t = \alpha_c = 0.0$ and $\alpha_t = 0.5, \alpha_c = 0.0$. The higher drop corresponds to the $\alpha_t = 1.0, \alpha_c = 0.5$, as would be expected. This also applies for the remainder of the test.

To choose the parameters that better represent the experimental results, one can right away discard the $\alpha_t = \alpha_c = 1.0$ since it has a lower maximum load in the first part of the test. The difference between the other cases is in the second part of the test. The curve that better suits the experimental results is the one from the $\alpha_t = 1.0, \alpha_c = 0.5$ case, as it features a high ultimate load and the load does not increase as much as the other cases in the last part of the test, although the stiffness still not matching the experimental results.

By using the best-suit curves for each failure criterion, it is possoble to see the results in Figure 5.11.

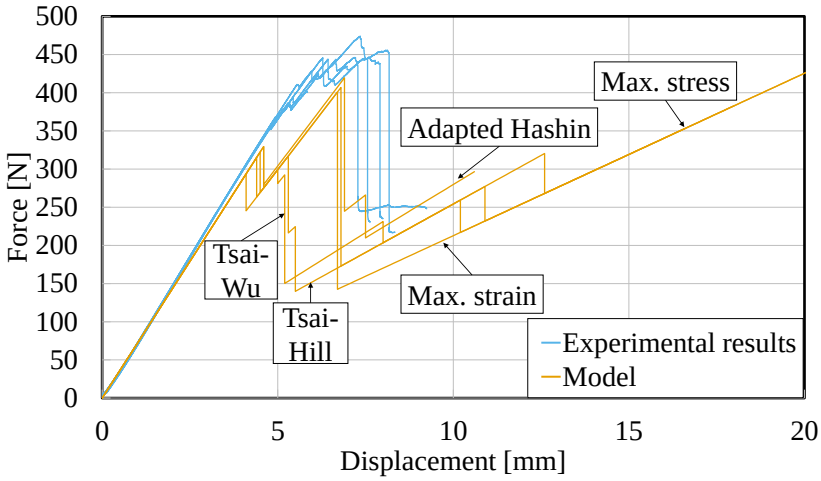

Figure 5.11: Experimental results compared to the best-fitted curve for each failure criterion.

As it is possible to see, the best-fitted curve is the adapted Hashin failure criterion one. Thus, for further analysis, this curve will be used for comparison as the model curve.

5.4.2 Four-point bending

5.4.2.1 Test setup

The test dimensions also followed the ASTM D7264 standard and had the dimensions shown in Table 5.6. Figure 5.12 shows the test setup.

5.4.2.2 Results and analysis

Figure 5.13 shows the force-displacement curves, while the test data, including ultimate flexural strength, calculated by Equation (2.31), flexural modulus, Equation (2.29), and ultimate strain, Equation (2.33), are presented in Table 5.7.

Table 5.6: Four-point bending testing dimensions.

Dimension [units]	**Value**
Specimen thickness [mm]	2.55
Specimen width [mm]	13
Specimen length [mm]	100
Span [mm]	80

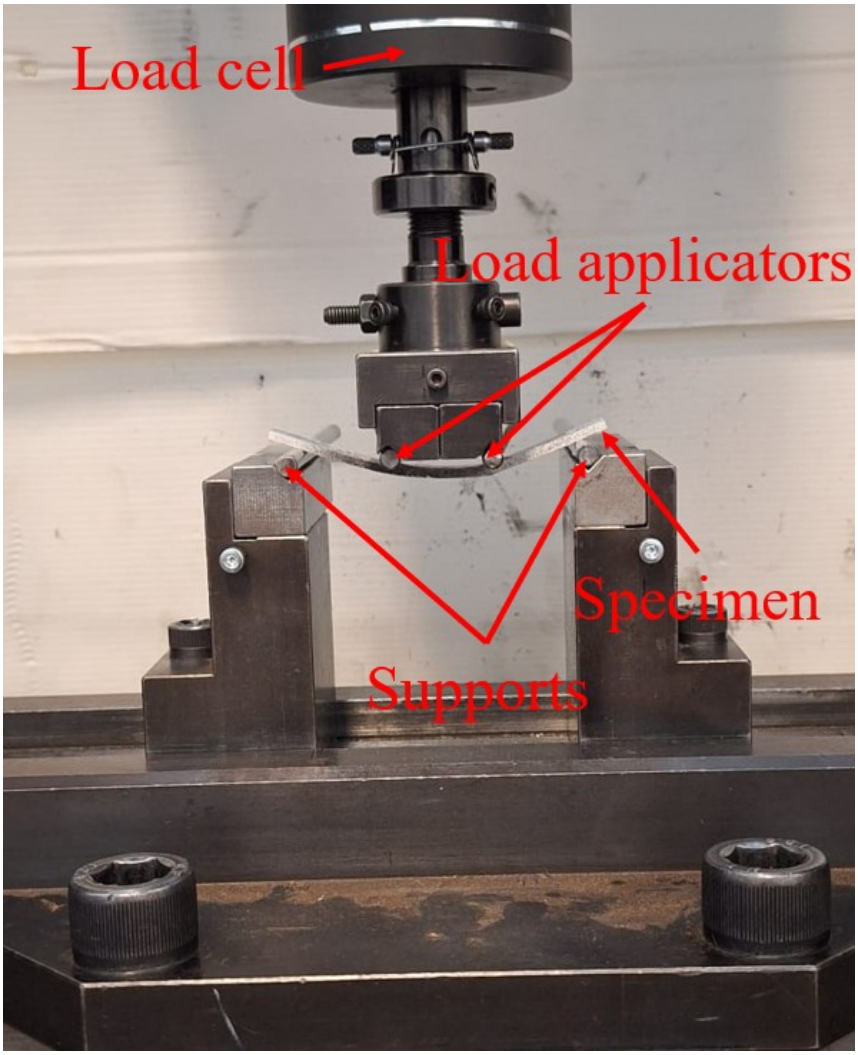

Figure 5.12: Four-point test setup.

Table 5.7: Four-point bending results.

Value [units]	**4PB_1**	**4PB_2**	**4PB_3**	**4PB_4**	**4PB_5**
Ultimate displacement [mm]	8.98	10.14	10.33	9.48	8.75
Average [mm]			9.54		
Standard deviation [mm]			0.69		

C.o.V [%]			7.3		
Ultimate load [N]	644.5	643.3	727.6	685.0	670.2
Average [N]			674.0		
Standard deviation [N]			0.04		
C.o.V [%]			5.1		
Ultimate flexural strength [MPa]	622.0	614.6	683.9	640.3	631.5
Average [MPa]			638.4		
Standard deviation [MPa]			27.18		
C.o.V [%]			4.3		
Flexural modulus [GPa]	45.81	45.34	44.61	44.08	44.72
Average [GPa]			44.91		
Standard deviation [GPa]			0.673		
C.o.V [%]			1.5		
Maximum strain [-]	0.0148	0.0168	0.171	0.0158	0.0145
Average [-]			0.0158		
Standard deviation [-]			0.001		
C.o.V [%]			7.3		

5.4.3 Comparison and analysis

The experimental results for all bending tests and the analytical predictions are shown in Figure 5.14.

The four-point bending tests lead to higher loads (443 N vs 674 N, average) and displacements (7.81 mm vs 9.53 mm, average) than three-point bending, as expected, due to the more uniform bending load in the middle section. The average ultimate flexural strength of the three-point bending test is 638.8 MPa, while in the four-point bending tests the average ultimate flexural strength is 638.4 MPa. Regarding the maximum strain, the average in the three-point bending test is 1.8%, while in the four-point bending test is 1.6%.

The average flexural modulus for the three-point bending tests was 47.3 GPa and for the four-point bending 44.9 GPa, meaning that the stiffness is almost independent of the test.

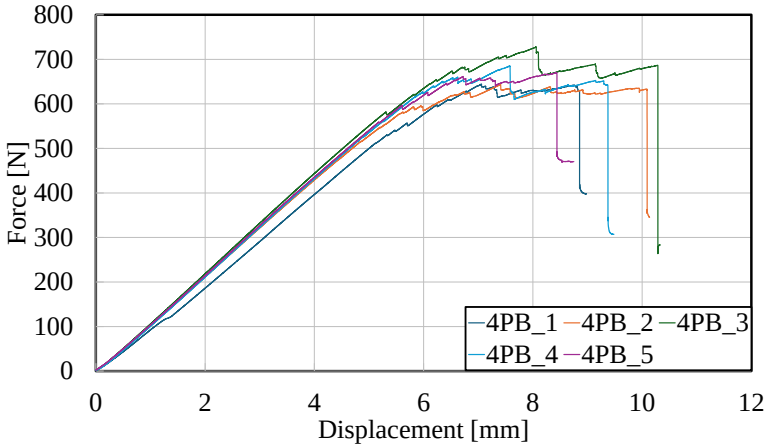

Figure 5.13: Four-point bending results.

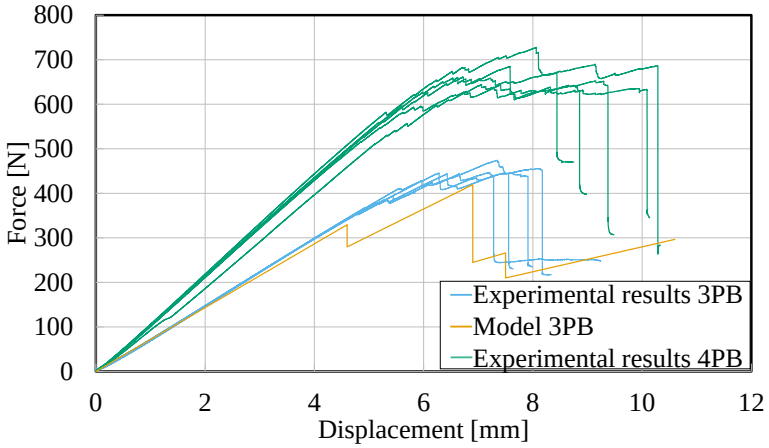

Figure 5.14: Three-point and four-point bending results compilation.

Chapter 6

Design for manufacturing

Taking into account all the studies and tests carried out so far in this work, the design phase ensues. The rules loosely specify the requirements for the box but these are mostly structural demands. Thus, the teams design the accumulator box acording to these demands and fit the size to their chassis space. This chapter reports the design phase of the accumulator. The final designed container is shown in Figure 6.1.

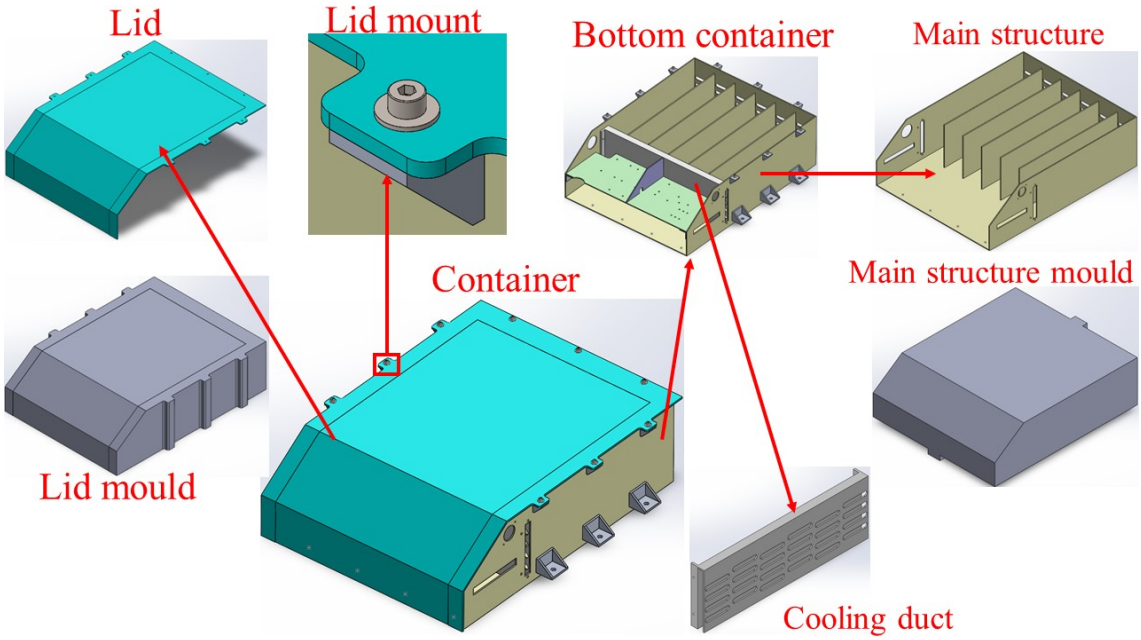

Figure 6.1: Container final design.

The production of the container in composite material requires the design of moulds to obtain the desired shape. The first step was to divide the container into two major components: the lid and the bottom part.

6.1 Lid design

The lid is a simple component with a simple geometry. The major feature of this component is its reinforcement in the bolted joints to the bottom container. When it comes to the mould, the first step is to fill the 3D shape of the component. Since it features quite a simple geometry, aspects such as draft angles are disregarded due to the absence of vertical walls.

6.2 Bottom container design

Due to the complexity pf the bottom portion of the accumulator box, a divison into smaller parts for manufacture is required. Note that the colours show the smaller components to be manufactured separately.

6.2.1 Main structure

The main structure of the bottom container is composed by the floor, external walls and main internal walls that divide the segments.

The long vertical walls that required a draft angle and the internal walls in the middle. However, it is important to have the external vertical walls without any draft angles so that the cell modules can enter the container and stay tight in their place. Thus, it was necessary to come up with a solution that did not require draft angles. This is done by dividing the mould into two symmetrical parts so that the mould can be demoulded through the sides without any problem. By having the middle separation in the master, it is possible to divide the carbon fibre mould into two parts, eliminating the need for draft angles in the external walls.

A simple way is to manufacture the internal walls is doing a big plate, cut it into the desired plate dimensions and use aluminium pieces to glue them to the floor and external walls. However, this method induces the same problem as draft angles - it could constrain the fitting of the cell modules - and induces more complexity as more processes and parts are present. Thus, another way of manufacturing the internal walls is by placing spacers to secure a low-thickness vertical plate with the desired dimensions. Then, the composite is laminated around that plate, the shape of the vertical wall. By doing this, it is possible to have a single structure, where the internal walls are directly connected to the floor and external walls.

6.2.2 Transverse internal walls

Tranverse walls create a separation between the cell modules zone and the electronic zone. Due to cooling requirements, this separation must be done by two walls, one holed wall to let air through, and the other to ensure the the physical separation of the two areas. As for the other internal walls, it was possible to do these walls with two different plates glued to the main structure. However, this induced the same problem. Thus, it was designed a cooling duct to be 3D printed in a fire-retardant filament.

However, the inner wall is structural, so it cannot be made of polymer only. Thus, as done for the internal walls, the manufacturing process of laying up the plies is done around the cooling duct, therefore providing the structural properties that the wall needs.

6.2.3 Eletronics stand-off and HV-LV separation plate

The electronics support plate and the HV and LV separation plate are the two plates at the front of the container. These two plates will be cut from a larger one and glued to the rest of the bottom container using aluminium placers, as shown in Figure 6.2.

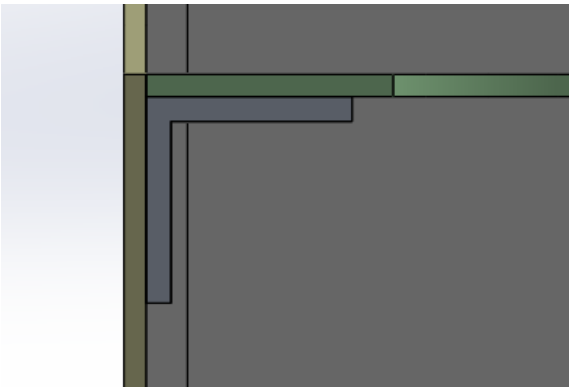

Figure 6.2: Aluminium placers for the electronics plate.

6.2.4 Chassis mounts

According to the rulebook, the chassis mounts must be manufactured from 1.6 mm thickness steel or 4 mm thickness aluminium and must have gussets to withstand bending loads. Since the aluminium mount, even considering the greater thickness, is lighter, the chosen material was aluminium, with the design shown in Figure 6.3.

These mounts will be glued to the main structure using a two-part epoxy adhesive. This connection must withstand a shear load of 20 kN. Knowing that the adhesive has a shear strength for etched aluminium of 15 MPa, one determine the margin of safety as:

$$MoS = \frac{\frac{20[kN]}{45[\text{mm}]\times[\text{m}m]}}{15[\text{MPa}]} - 1 = 0.0125 \tag{6.1}$$

Since the 20 kN load is already a safety measure, as the 40g acceleration would induce only 3043 N per attachment, a margin of safety of 0.0125 is acceptable in this case.

6.2.5 Lid mounts

To mount the lid, 9 supports are glued to the main structure. The margin of safety can also be determined for the 20g vertical loadcase divided by the 9 attachments and it is given by:

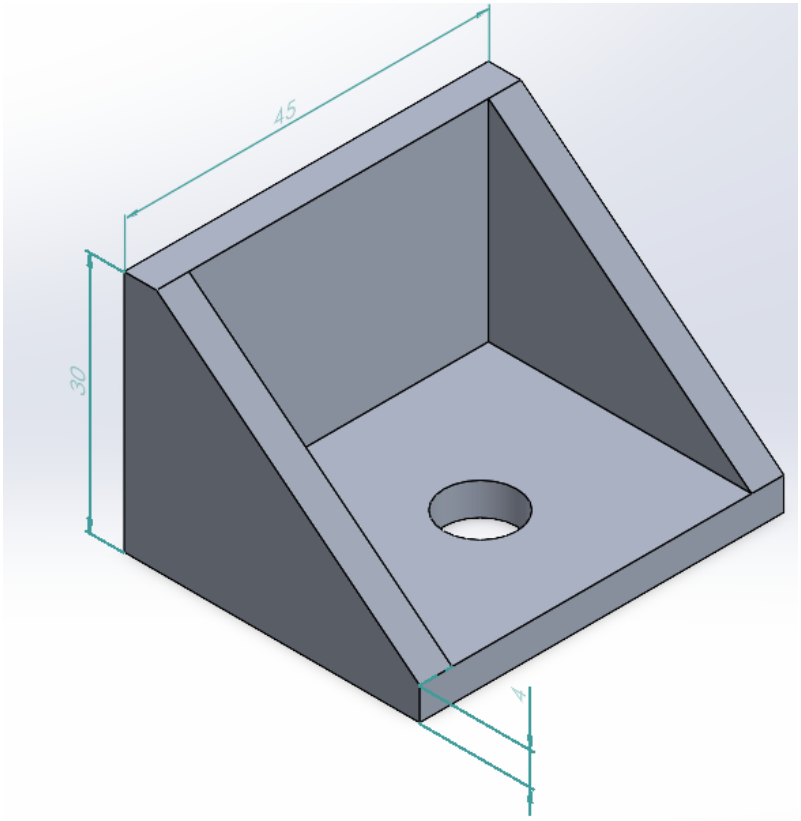

Figure 6.3: Aluminium chassis mount.

$$MoS = \frac{\frac{831.36[N]}{20[\text{mm}]\times 20[\text{mm}]}}{15[\text{MPa}]} - 1 = 6.2170 \tag{6.2}$$

Chapter 7

Conclusions and future work

In this thesis, the design of a new accumulator container for a Formula Student car was studied, employing composite material instead of aluminium. The main conclusions of the design solution proposed will be presented, while also presenting some suggestions of improvement and future work.

7.1 Conclusions

Due to the importance of the accumulator container to overall safety, the Formula Student competition requires experiments to validate the mechanical performance of the selected laminates. However, due to the cost associated with testing, whether due to the material itself, the manufacturing process or the testing execution, numerical models and simulations play a huge role in the design of the accumulator container in an initial phase. That is the reason why a numerical model to estimate the flexural properties of a laminate was important for preliminary material selection and layup design. In addition, Finite Element Analysis was key for designing and optimising the components.

Thus, after setting the targets and setting the constraints imposed by the chassis and the electrical components inside the container, a Python script for three-point bending analysis using classical composite theories was developed to predict bending failure of the laminate. The code predicts ply-by-ply failure and draws the predicted force-displacement curve of the test. The model parameters were adjusted using the test results that also served as a validation for the model. Although this model does not replace testing, it was employed in the pre-selection of the laminates that should be tested to make the final choice

It was found that the model was accurate during the first phase of the test, i.e, in the elastic region until first ply failure, with very good correlation between the experimental stiffness and the predictions. For last ply failure, the adapted Hashin failure criteria provided the best results. However, there were still some differences between the model and the experiments, although the maximum force and displacement predictions were reasonably good.

Layup optimisation was then performed using Finite Element Analysis. Optimisation was performed in two phases, the first one to optimise the lid and the last to optimise the container. By doing these simulations, it was to define the final layup and reinforce zones that were most likely to fail. The final layup and locally reinforced regions were optimised to decrease the weight while ensuring safety. Additional weight efficiency could be obtained, but fire retardancy standards imposed by the competition limited the minimum laminate thickness.

In the final design, the total weight was 7.4 kg, including the chassis mounts, while complying with the rules. This constitutes a decrease of 2.6 kg in relation to the aluminium equivalent. The container and the lid have CFRP to ensure good mechanical properties, an outer 0.5 mm-thick aluminium layer to ensure grounding to the chassis and an inner GFRP layer to provide electrical insulation between the segments and the walls.

7.2 Future work

After assessing some numerical models found in the literature, some were employed in this work. However, the one used in the three-point bending test needs to be improved. Although the model provides similar results to the experimental test results, there are ways to improvement. Possibly, combining Finite Element Analysis with analytical models would result in more accurate results than the ones obtained with this initial version of the model.

Due to some constraints in the material manufacturing, the experimental validation of the material to be used for the design was not performed. In turn, a similar composite material was used to generate a work flow for when the definitive material is available for the production of the box. The test material was used only for validation of the process. Thus, it is necessary to test the layups used with the material used, with the dimensions imposed by the rules. In addition, although at the time of writing, the specicimens for the perimeter shear test are ready, the test is yet to be performed. It must be done to prove equivalency to the steel and aluminium properties.

Finaly, when the selected material is available, the final manufacturing of the battery box will be possible by the mould design and layup studies conducted during this work, as well as a specific section of the experimental material characterisation.

References

International Energy Agency. Global EV Outlook 2023: Catching up with climate ambitions, 2023. URL https://www.iea.org/reports/global-ev-outlook-2023.

ASTM International. *Standard Test Method for In-plane Shear Response of Polymer Matrix Composite Materials by Tensile Test of a ± 450 Laminate*. 2007.

ASTM International. Standard Test Method for Tensile Properties of Polymer Matrix Composite Materials, 2008.

ASTM International. Standard test method for flexural properties of polymer matrix composite materials, 2015.

ASTM International. Standard test method for shear strength of plastics by punch tool, 2017.

R. Beigpour, H. Shokrollahi, and S. M. R. Khalili. Experimental and numerical analysis of a biodegradable hybrid composite under tensile and three-point bending tests. *Composite Structures*, 273:114255, 2021. ISSN 0263-8223. doi: 10.1016/j.compstruct.2021.114255.

Bold Valuable Tech. Formula 1 ESS Batteries. URL https://boldvaluable.tech/blog/formula-1-ess-batteries/. Accessed in January 2024.

P.P. Camanho, A. Arteiro, A.R. Melro, G. Catalanotti, and M. Vogler. Three-dimensional invariant-based failure criteria for fibre-reinforced composites. *International Journal of Solids and Structures*, 55:92–107, 2015. ISSN 0020-7683. doi: 10.1016/j.ijsolstr.2014.03.038. Special Issue Computational and Experimental Mechanics of Advanced Materials A workshop held at King Abdullah University of Science and Technology Jeddah, Kingdom of Saudi Arabia July 1-3, 2013.

D. Case. History of formula SAE, 1996. Formula SAE. Available at https://www.fsaeonline.com/page.aspx?pageid=c4c5195a-60c0-46aa-acbf-2958ef545b72, Accesed in September of 2023.

G. Catalanotti, P.P. Camanho, and A.T. Marques. Three-dimensional failure criteria for fiber-reinforced laminates. *Composite Structures*, 95:63–79, 2013. ISSN 0263-8223. doi: 10.1016/j.compstruct.2012.07.016.

C. C. Chan. The rise & fall of electric vehicles in 1828–1930: Lessons learned [scanning our past]. *Proceedings of the IEEE*, 101:206–212, 01 2013. doi: 10.1109/JPROC.2012.2228370.

SHD Composites. *FRVC411*.

D. Dalli et al. Assessing the current modelling approach for predicting the crashworthiness of formula one composite structures. *Composites Part B: Engineering*, 201:108242, 2020.

EAA. Electric vehicle history, 2021. Electric Auto Association. Available at https://studylib.net/doc/8119651/electric-vehicle-history---electric-auto-association, Accessed in September of 2023.

EVBox. History of the electric car, 2021. Available at https://blog.evbox.com/electric-cars-history, Accessed in September of 2023.

R. T. Fenner and J. N. Reddy. *Mechanics of solids and structures*. CRC Press/Taylor & Francis Group, 2012. ISBN 9781439858141.

A. Formisano, L. Boccarusso, M. Durante, and A. Langella. Punch tool based out-of-plane shear behaviour of gfrp composites. *Composite Structures*, 163:325–330, 2017. ISSN 0263-8223. doi: 10.1016/j.compstruct.2016.12.048.

FSG. Formula student rules 2024, 2023a. Formula Student Germany. Available at https://www.formulastudent.de/fileadmin/user_upload/all/2023/rules/FS-Rules_2023_v1.1.pdf, Accessed in September of 2023.

FSG. Chronicle, 2023b. Formula Student Germany. Available at https://www.formulastudent.de/fileadmin/user_upload/all/2024/rules/FS-Rules_2024_v1.0.pdf, Accessed in October of 2023.

Y. Hu, G. Han, F. Cheng, and X. Hu. Thickness effect on flexural strengths of laminar carbon fibre composites. *Thin-Walled Structures*, 186:110690, 2023. ISSN 0263-8231. doi: 10.1016/j.tws.2023.110690.

C. Höhne, P. Blaess, S. Ilinzeer, and P. Griesbaum. New approach for electric vehicle composite battery housings: Electromagnetic shielding and flame retardancy of pur/up-based sheet moulding compound. *Composites Part A: Applied Science and Manufacturing*, 167:107404, 2023. ISSN 1359-835X. doi: 10.1016/j.compositesa.2022.107404.

IMechE. History of Formula Student, 2021. Formula Student. Available at https://www.fsaeonline.com/page.aspx?pageid=c4c5195a-60c0-46aa-acbf-2958ef545b72, Accessed in September of 2023.

R. M. Jones. *MECHANICS OF COMPOSITE MATERIALS*. Taylor & Francis, 1999.

P. K. Mallick. *Fiber Reinforced Composites Materials, Manufacturing, and Design*. CRC Press, 2007.

J. D. D. Melo, S. K. Ha, and S. W. Tsai. *Strength & Life of Composites*. 2011. ISBN 978-0-9819143-1-2.

A. K. Mohanty, S. Vivekanandhan, N. Tripathi, P. Roy, M. R. Snowdon, L. T. Drzal, and M. Misra. Sustainable composites for lightweight and flame retardant parts for electric vehicles to boost climate benefits: A perspective. *Composites Part C: Open Access*, 12:100380, 2023. ISSN 2666-6820. doi: 10.1016/j.jcomc.2023.100380.

A. Puck and H. Schürmann. Failure analysis of frp laminates by means of physically based phenomenological models. *Composites science and technology*, 62(12-13):1633–1662, 2002.

Research and Markets. Global $4.47 bn electric vehicle (EV) battery housing market to 2025: Opportunities in housing with integrated cooling systems, 2021. URL https://www.researchandmarkets.com/r/bu5ps4.

K. S. Kumar, R. Rengaraj, G.R. Venkatakrishnan, and A. Chandramohan. Polymeric materials for electromagnetic shielding - a review. *Materials Today: Proceedings*, 47:4925–4928, 2021. ISSN 2214-7853. doi: 10.1016/j.matpr.2021.03.720. International Conference on Sustainable materials, Manufacturing and Renewable Technologies 2021.

C. Schludi and J. Joos. Lightweight and safe composite battery housings, 2019.

S. Sulardjaka, N. Iskandar, S. Nugroho, A. Alamsyah, and M.Y. Prasetya. The characterization of unidirectional and woven water hyacinth fiber reinforced with epoxy resin composites. *Heliyon*, 8(9):e10484, 2022. ISSN 2405-8440. doi: 10.1016/j.heliyon.2022.e10484.

S. F. Tie and C. W. Tan. A review of energy sources and energy management system in electric vehicles. *Renewable and Sustainable Energy Reviews*, 20:82–102, 2013. ISSN 1364-0321. doi: 10.1016/j.rser.2012.11.077.

Toray. *Toray TC346/T700SC*.

J. Warner. *The Handbook of Lithium-Ion Battery Pack Design*. Elsevier Science, 2015.

Appendix A

Code

A.1 Main code

```
"""
%%%%%%%%%%%%%%%%%%%%%%%%%%%%%%%%%%%%%%%%%%%%%%%%%%%%%%%%%%%%%%%%%%%%%%%%
% Renato Silva Costa                                                    %
%%%%%%%%%%%%%%%%%%%%%%%%%%%%%%%%%%%%%%%%%%%%%%%%%%%%%%%%%%%%%%%%%%%%%%%%

"""

import functions, matplotlib.pyplot as plt, numpy as np, os

input_folder = 'DIRECTORY' # Change as needed
output_folder = 'DIRECTORY' # Change as needed

inputs = os.listdir(input_folder)

with open(output_folder+'properties.txt', 'w') as file:

        file.write('Specimen number \t Thickness [mm] \t Ef [MPa]\n')

# AHASHIN CONSTANT

alphat = 1 # Contribution of shear stress to the tensile failure criteria
alphac = 0.5 # Contribution of shear stress to the compressive failure criteria

# DATA

for specimen in range(len(inputs)-3):

    input = input_folder+f'specimen{specimen+1}.txt'

    data = np.genfromtxt(input, delimiter='\t')

    E1 = data[1:,3] # Pa
```

```
    E2 = data[1:,4] # Pa
    G12= data[1:,5] # Pa
    nu12= data[1:,6] # Poisson ratio 12
    nu21= nu12*E2/E1 # Poisson ratio 21
    Xt = data[1:,7] # Tensile strength fiber direction
    Yt = data[1:,8] # Tensile strength perpendicular direction
    Xc = data[1:,9] # Compression strength fiber direction
    Yc = data[1:,10] # Compression strength perpendicular direction
    S12 = data[1:,11] # In Plane shear strength
    S23 = data[1:,12] # In Plane shear strength
    Xlt = Xt/E1 # Tensile strain fiber direction
    Ylt = Yt/E2 # Tensile strain perpendicular direction
    Xlc = Xc/E1 # Compression strain fiber direction
    Ylc = Yc/E2 # Compression strain perpendicular direction
    Sl12 = S12/G12 # In Plane shear strain

    lam = data[1:,1] # Laminate lay-up
    t = data[1:,2] # Ply thickness (for each lamina)

    t_total = sum(t) # total laminate thickness

    zb = np.zeros((len(lam)+1)) # Vector to store coordinates
    zb[0] = -t_total/2

    ndiv = 10 # number of divisions per ply

    force = np.array(([])) # variable to store the force
    displacement = np.array(([])) # variable to store the displacement

    # GEOMETRY (edit as required)

    b = 0.013 # specimen width [m]
    l = 0.082 # support span [m]

    # SYSTEM VARIABLES

    stop = False # variable to stop the loop
    failureMS = np.full((len(lam), ndiv+1), False) # variable to stop the Maximum
    Stress criteria
    failuredataMS = np.zeros((len(lam), 2))
    failureMSl = np.full((len(lam), ndiv+1), False) # variable to stop the Maximum
    Strain criteria
    failuredataMSl = np.zeros((len(lam), 2))
    failureTH = np.full((len(lam), ndiv+1), False) # variable to stop the Tsai-Hill
     criteria
    failuredataTH = np.zeros((len(lam), 2))
    failureTW = np.full((len(lam), ndiv+1), False) # variable to stop the Tsai-Wu
    criteria
    failuredataTW = np.zeros((len(lam), 2))
```

```
    failureAHashin = np.full((len(lam), ndiv+1), False) # variable to stop the Tsai
    -Wu criteria
    failuredataAHashin = np.zeros((len(lam), 2))
    disp = 0 # displacement initialisation
    fpf = False # variable to know if we are before or after FPF

    while stop == False:

        # CLT

        stressx, stressf, strainx, strainf, z, A, B, D, P,N = functions.CLT(disp, b
    , l, lam, E1, E2, nu12, nu21, G12, t,t_total, zb, ndiv, failureTW)

        force = np.hstack((force, P))
        displacement = np.hstack((displacement, disp*1000))
        plyfail = False # System variable to know when a ply fails

        for ply in range(len(z)):

            for i in range(len(z[0])): # for each point

                # Apply the criteria (COMMENT LINES AS NEEDED)
                '''
                if failureMS[ply, i] == False: # Maximum stress

                    failureMS[ply,i] = functions.MAXIMUMSTRESS(Xt[ply], Xc[ply], Yt
    [ply], Yc[ply], S12[ply], stressf[:, int(str(ply) + str(i))])

                    if failureMS[ply, i] == True:

                        failuredataMS[ply, 0] = disp*1000
                        failuredataMS[ply, 1] = P

                        failureMS[ply, :] = True
                        plyfail = True

                        d=0.07

                        # Ply damage
                        E1[ply] = d*E1[ply]
                        E2[ply] = d*E2[ply]
                        G12[ply] = d*G12[ply]

                        failurepointMS = np.array(([disp, P]))

                        print('--------------------------------------')
                        print('MAXIMUM STRESS')
                        print('--------------------------------------')
                        print('Failure in ply', ply, '. Load:', P, 'N')
```

```
124
125             if failureMSl[ply, i] == False: # Maximum stress
126
127                 failureMSl[ply,i] = functions.MAXIMUMSTRAIN(Xlt[ply], Xlc[ply],
    Ylt[ply], Ylc[ply], Sl12[ply], strainf[:, int(str(ply) + str(i))])
128
129                 if failureMSl[ply, i] == True:
130
131                     failuredataMSl[ply, 0] = disp*1000
132                     failuredataMSl[ply, 1] = P
133
134                     failureMSl[ply, :] = True
135                     plyfail = True
136
137                     d=0.07
138
139                     # Ply damage
140                     E1[ply] = d*E1[ply]
141                     E2[ply] = d*E2[ply]
142                     G12[ply] = d*G12[ply]
143
144                     failurepointMSl = np.array(([disp, P]))
145
146                     print('----------------------------------------')
147                     print('MAXIMUM STRAIN')
148                     print('----------------------------------------')
149                     print('Failure in ply', ply, '. Load:', P, 'N')
150
151             if failureTH[ply, i] == False:
152
153                 failureTH[ply, i] = functions.TSAIHILL(Xt[ply], Xc[ply], Yt[ply
    ], Yc[ply], S12[ply], stressf[:, int(str(ply) + str(i))])
154
155                 if failureTH[ply, i] == True:
156
157                     failuredataTH[ply, 0] = disp*1000
158                     failuredataTH[ply, 1] = P
159
160                     failureTH[ply, :] = True
161                     plyfail = True
162
163                     d=0.07
164
165                     # Ply damage
166                     E1[ply] = d*E1[ply]
167                     E2[ply] = d*E2[ply]
168                     G12[ply] = d*G12[ply]
169
170                     print('----------------------------------------')
```

```
                        print('TSAI-HILL')
                        print('---------------------------------------')
                        print('Failure in ply', ply, '. Load:', P, 'N')

                if failureTW[ply, i] == False:

                    failureTW[ply, i] = functions.TSAIWU(Xt[ply], Xc[ply], Yt[ply], Yc[ply], S12[ply], stressf[:, int(str(ply) + str(i))])

                    if failureTW[ply, i] == True:

                        failuredataTW[ply, 0] = disp*1000
                        failuredataTW[ply, 1] = P

                        failureTW[ply, :] = True
                        plyfail = True

                        d=0.14

                        # Ply damage
                        E1[ply] = d*E1[ply]
                        E2[ply] = d*E2[ply]
                        G12[ply] = d*G12[ply]

                        print('---------------------------------------')
                        print('TSAI-WU')
                        print('---------------------------------------')
                        print('Failure in ply', ply+1, '. Load:', P, '[N]', '. Displacement:', disp*1000, '[mm]')
                        print(N[3])

                        #functions.plot_CLT(z, stressx, strainx, stressf, strainf) # Plot stress and strain when failure occurs
                        if fpf == False:
                            functions.store_CLT(z, stressx, strainx, stressf, strainf, output_folder, specimen)
                            fpf = True
                            print(A)
                            print(B)
                            print(D)

                '''
                if failureAHashin[ply, i] == False:

                    failureAHashin[ply, i], TFF, CFF, TMF, CMF = functions.AHASHIN(Xt[ply], Xc[ply], Yt[ply], Yc[ply], S12[ply], S23[ply], alphat, alphac, stressf[:, int(str(ply) + str(i))])

                    if failureAHashin[ply, i] == True:
```

```
214
215                         failuredataAHashin[ply, 0] = disp*1000
216                         failuredataAHashin[ply, 1] = P
217
218                         failureAHashin[ply, :] = True
219                         plyfail = True
220
221                         d1=d2=d6=1
222
223                         if TFF == True:
224                             d1 = 0.07
225
226                         if CFF == True:
227                             d1 = 0.14
228
229                         if TMF == True:
230                             d2 = 0.2
231                             d6 = 0.2
232
233                         if CMF == True:
234                             d2 = 0.4
235                             d6 = 0.4
236
237                         # Ply damage
238                         E1[ply] = d1*E1[ply]
239                         E2[ply] = d2*E2[ply]
240                         G12[ply] = d6*G12[ply]
241
242                         print('--------------------------------------')
243                         print('AHASHIN')
244                         print('--------------------------------------')
245                         print('Failure in ply', ply+1, '. Load:', P, '[N]', '.
    Displacement:', disp*1000, '[mm]')
246                         print(TFF, CFF, TMF, CMF)
247
248                         #functions.plot_CLT(z, stressx, strainx, stressf, strainf)
    # Plot stress and strain when failure occurs (UNCOMMENT AS NEEDED)
249                         if fpf == False:
250                             functions.store_CLT(z, stressx, strainx, stressf,
    strainf, output_folder, specimen)
251                             fpf = True
252                         print(TFF, CFF, TMF, CMF)
253
254         if np.all(failureAHashin) or disp >= 0.02:
255             stop = True
256             break
257
258         if plyfail == False:
259             disp += 0.0001
```

```
260
261     # CALCULATE LAMINATE PROPERTIES
262
263     sigmaf = (3*np.max(force)*l)/(2*b*t_total**2)*10**(-6) # Flexural Strength, MPa
264
265     print(sigmaf, 'MPa')
266
267     # PLOT FORCE VS DISPLACEMENT RESULTS
268
269     label_points = np.arange(1, len(lam)+1)
270
271     plt.figure(figsize=(15, 7.5))
272     plt.plot(displacement, force, label='Force vs Displacement')
273     #plt.scatter(failurepointMS[0], failurepointMS[1], label='Failure Point Maximum
         Stress')
274     #plt.scatter(failurepointTH[0], failurepointTH[1], label='Failure Point Tsai-
        Hill')
275     for ply in range(len(lam)):
276         plt.scatter(failuredataAHashin[ply,0], failuredataAHashin[ply, 1], label=('
        Ply', label_points[ply]))
277     #plt.scatter(failurepointPUCK[0], failurepointPUCK[1], label='Failure Point
        Puck')
278     plt.xlim(np.min(displacement), np.max(1.1*displacement))
279     plt.ylim(np.min(force), 1.1*np.max(force))
280     plt.xlabel('Displacement [mm]')
281     plt.ylabel('Force [N]')
282     plt.legend()
283     plt.grid()
284     plt.title('Three Point Bending')
285     plt.savefig(output_folder+f'{specimen+1}forcevsdisplacement.png')
286     plt.show()
287
288     with open(output_folder+f'{specimen+1}forcevsdisplacement.txt', 'w') as file:
289
290         file.write('Force [N] \t Displacement [mm]\n')
291
292     with open(output_folder+f'{specimen+1}forcevsdisplacement.txt', 'a') as file:
293
294         for d, f in zip(displacement, force):
295
296             file.write(f"{d}\t{f}\n")
297
298     with open(output_folder+'properties.txt', 'a') as file:
299
300         file.write(f"{specimen}\t{t_total*1000}\t{sigmaf}\n")
```

A.2 Functions code

```
1 """
```

```
%%%%%%%%%%%%%%%%%%%%%%%%%%%%%%%%%%%%%%%%%%%%%%%%%%%%%%%%%%%%%%%%%%%%%%%%
% Renato Silva Costa                                                    %
%%%%%%%%%%%%%%%%%%%%%%%%%%%%%%%%%%%%%%%%%%%%%%%%%%%%%%%%%%%%%%%%%%%%%%%%

"""

import numpy as np, matplotlib.pyplot as plt
from matplotlib.lines import Line2D
from math import cos, sin, radians

def CLT(disp, b, length, l, E1, E2, nu12, nu21, G12, t, t_total, zb, ndiv, failure)
    :

    zn = np.empty((1,ndiv))

    N = np.zeros((6,1)) # Loads initialisation

    # Create Matrices

    A = np.zeros((3,3))
    B = np.zeros((3,3))
    D = np.zeros((3,3))

    for i in range(len(l)):

        # Constants

        Q11 = E1[i]/(1-nu21[i]*nu12[i])
        Q12 = (nu12[i]*E2[i])/(1-nu21[i]*nu12[i])
        Q22 = E2[i]/(1-nu21[i]*nu12[i])
        Q66 = G12[i]

        # Q matrix
        Q = np.zeros((3,3))
        m = cos(radians(l[i]))
        n = sin(radians(l[i]))
        Q[0,0] = Q11*m**4 + Q22*n**4 + 2*(Q12+2*Q66)*m**2*n**2
        Q[0,1] = (Q11+Q22-4*Q66)*m**2*n**2 + Q12*(m**4+n**4)
        Q[1,0] = Q[0,1]
        Q[1,1] = Q11*n**4 + Q22*m**4 + 2*(Q12 + 2*Q66)*m**2*n**2
        Q[0,2] = (Q11-Q12-2*Q66)*m**3*n - (Q22-Q12-2*Q66)*(n**3)*m
        Q[2,0] = Q[0,2]
        Q[1,2] = (Q11 - Q12 -2*Q66)*m*n**3 - (Q22-Q12-2*Q66)*m**3*n
        Q[2,1] = Q[1,2]
        Q[2,2] = (Q11 + Q22 -2*Q12 - 2*Q66)*m**2*n**2 + Q66*(n**4 + m**4)

        # Thickness

        zb[i+1] = zb[i]+t[i]
```

```
        zb1 = zb[i+1]-zb[i]
        zb2 = ((zb[i+1])**2)-((zb[i])**2)
        zb3 = ((zb[i+1])**3)-((zb[i])**3)

        # A, B, D matrices

        for p in range(3):

            for j in range(3):

                A[p,j] = A[p,j] + Q[p,j]*(zb1)
                B[p,j] = B[p,j] + Q[p,j]*(zb2)
                D[p,j] = D[p,j] + Q[p,j]*(zb3)

    B = B/2
    D = D/3

    for i in range(3):
        for j in range(3):
            if abs(A[i,j]) < 10**-5:
                A[i,j] = 0
            if abs(B[i,j]) < 10**-5:
                B[i,j] = 0
            if abs(D[i,j]) < 10**-5:
                D[i,j] = 0

    P = np.vstack((np.hstack((A,B)), np.hstack((B, D))))

    # LOAD CALCULATION

    Exx = (A[0,0]*A[1,1]-A[0,1]**2)/(t_total*A[1,1]) # apparent stiffness
    I = (b*t_total**3)/12
    EIb = Exx * I # bending stiffness
    F = -(48*disp*EIb)/(length**3) # force
    F = abs(F)

    N[3] = -((F*length)/4)/b

    # Deformations

    e0 = np.linalg.solve(P, N) # Deformations (traction, rotation)

    # Stresses

    stressx = np.array(([], [], [])) # Considered coordinate system
    strainx = np.array(([], [], [])) # Considered coordinate system
    stressf = np.array(([], [], [])) # Fiber coordinate system
    strainf = np.array(([], [], [])) # Fiber coordinate system
    sigma = np.zeros((1,3))
```

```
99
100     x = []
101     e = np.zeros((3,ndiv))
102
103     for i in range(len(l)):
104
105         # Constants
106
107         Q11 = E1[i]/(1-nu21[i]*nu12[i])
108         Q12 = (nu12[i]*E2[i])/(1-nu21[i]*nu12[i])
109         Q22 = E2[i]/(1-nu21[i]*nu12[i])
110         Q66 = G12[i]
111
112         # Q matrix
113         Q = np.zeros((3,3))
114         m = cos(radians(l[i]))
115         n = sin(radians(l[i]))
116         Q[0,0] = Q11*m**4 + Q22*n**4 + 2*(Q12+2*Q66)*m**2*n**2
117         Q[0,1] = (Q11+Q22-4*Q66)*m**2*n**2 + Q12*(m**4+n**4)
118         Q[1,0] = Q[0,1]
119         Q[1,1] = Q11*n**4 + Q22*m**4 + 2*(Q12 + 2*Q66)*m**2*n**2
120         Q[0,2] = (Q11-Q12-2*Q66)*m**3*n - (Q22-Q12-2*Q66)*(n**3)*m
121         Q[2,0] = Q[0,2]
122         Q[1,2] = (Q11 - Q12 -2*Q66)*m*n**3 - (Q22-Q12-2*Q66)*m**3*n
123         Q[2,1] = Q[1,2]
124         Q[2,2] = (Q11 + Q22 -2*Q12 - 2*Q66)*m**2*n**2 + Q66*(n**4 + m**4)
125
126         # Transformation matrix for stress
127         Ts = np.array([[m**2, n**2, 2*m*n], [n**2, m**2, -2*m*n], [-m*n, m*n, m**2-
    n**2]])
128
129         # Transformation matrix for strain
130         Te = np.array([[m**2, n**2, m*n], [n**2, m**2, -m*n], [-2*m*n, 2*m*n, m**2-
    n**2]])
131
132         x = np.linspace(zb[i], zb[i+1], ndiv)
133         zn = np.vstack((zn, x.reshape(1, -1)))
134         z = zn[1:]
135
136         for j in range(len(x)): # update of the strain vector for the point
137
138             e[0,j] = e0[0] + x[j]*e0[3]
139             e[1,j] = e0[1] + x[j]*e0[4]
140             e[2,j] = e0[2] + x[j]*e0[5]
141
142         sigma = np.dot(Q, e)
143         sigmaf = np.dot(Ts, sigma)
144         ef = np.dot(Te, e)
145
```

```
146         stressx = np.hstack((stressx, sigma)) # Stress along the original
    coordinate system
147         stressf = np.hstack((stressf, sigmaf)) # Stress along fiber coordinate
    system
148         strainx = np.hstack((strainx, e)) # Strain along the original coordinate
    system
149         strainf = np.hstack((strainf, ef)) #  Strain along fiber coordinate system
150 
151     return stressx, stressf, strainx, strainf, z, A, B, D, F,N
152 
153 def MAXIMUMSTRESS(Xt, Xc, Yt, Yc, S12, stress):
154 
155     failure = False
156 
157     if stress[0] >= 0: # Tensile failure fibre direction
158         X1 = Xt
159     else: # Compressive failure fibre direction
160         X1 = Xc
161 
162     if stress[1] >= 0: # Tensile failure perpendicular direction
163         X2 = Yt
164     else: # Compressive failure perpendicular direction
165         X2 = Yc
166 
167     X12 = S12 # Shear failure
168 
169     if abs(stress[0]) > X1:
170         failure = True
171 
172     if abs(stress[1]) > X2:
173         failure = True
174 
175     if abs(stress[2]) > X12:
176         failure = True
177 
178     return failure
179 
180 def MAXIMUMSTRAIN(Xlt, Xlc, Ylt, Ylc, Sl12, strain):
181 
182     failure = False
183 
184     if strain[0] >= 0: # Tensile failure fibre direction
185         Xl1 = Xlt
186     else:
187         Xl1 = Xlc # Compressive failure fibre direction
188 
189     if strain[1] >= 0: # Tensile failure perpendicular direction
190         Xl2 = Ylt
191     else: # Compressive failure perpendicular direction
```

```
192         Xl2 = Ylc
193 
194     Xl12 = Sl12 # Shear failure
195 
196     if abs(strain[0]) > Xl1:
197         failure = True
198 
199     if abs(strain[1]) > Xl2:
200         failure = True
201 
202     if abs(strain[2]) > Xl12:
203         failure = True
204 
205     return failure
206 
207 def TSAIHILL(Xt, Xc, Yt, Yc, S12, stress):
208 
209     failure = False
210 
211     # CONSTANTS
212 
213     if stress[0] >= 0:
214         F1 = Xt
215     else:
216         F1 = Xc
217 
218     if stress[1] >= 0:
219         F2 = Yt
220     else:
221         F2 = Yc
222 
223     F6 = S12
224 
225     factor = (stress[0]**2)/(F1**2) + (stress[1]**2)/(F2**2) + (stress[2]**2)/(F6
    **2) - (stress[0]*stress[1])/(F1**2)
226 
227     if factor >= 1:
228         failure = True
229 
230     return failure
231 
232 def TSAIWU(Xt, Xc, Yt, Yc, S12, stress):
233 
234     failure = False
235 
236     # CONSTANTS
237 
238     F1 = 1/Xt - 1/Xc
239     F2 = 1/Yt - 1/Yc
```

```
240     F11 = 1/(Xt*Xc)
241     F22 = 1/(Yt*Yc)
242     F12 = -0.5*np.sqrt(1/(Xt*Xc*Yt*Yc))
243     F6 = 1/S12 - 1/S12
244     F66 = 1/(S12**2)
245 
246     factor = F1*stress[0] + F2*stress[1] + 2*F12*stress[0]*stress[1] + F11*stress
        [0]**2 + F22*stress[1]**2 + F6*stress[2] + F66*stress[2]**2
247 
248     if factor >= 1:
249         failure = True
250 
251     return failure
252 
253 def AHASHIN(Xt, Xc, Yt, Yc, S12, S23, alphat, alphac, stress):
254 
255     failure = False
256     TFF = False # Tensile Fiber failure
257     CFF = False # Compressive Fiber failure
258     TMF = False # Tensile Matrix failure
259     CMF = False # Compressive Matrix failure
260 
261     if stress[0] >= 0:
262         factor = (stress[0]/Xt)**2 + alphat*(stress[2]/S12)**2
263 
264         if factor >= 1:
265             failure = True
266             TFF = True
267 
268     if stress[0] < 0:
269         factor = (stress[0]/Xc)**2 + alphac*(stress[2]/S12)**2
270 
271         if factor >= 1:
272             failure = True
273             CFF = True
274 
275     if stress[1] >=0:
276         factor = (stress[1]/Xt)**2 + alphat*(stress[2]/S12)**2
277 
278         if factor >= 1:
279             failure = True
280             TMF = True
281 
282     if stress[1] < 0:
283         factor = (stress[1]/Xc)**2 + alphac*(stress[2]/S12)**2
284 
285         if factor >= 1:
286             failure = True
287             CMF = True
```

```
288
289     return failure, TFF, CFF, TMF, CMF
290
291 def plot_CLT(z, stressx, strainx, stressf, strainf): # Just to plot the CLT if
        intended
292
293     z = z.reshape(1, -1)
294
295     for k in range(4):
296
297         if k == 0: # Stress in the global coordinate system
298             fun = stressx*10**-6
299             xlabel = 'Stress [MPa]'
300             ylabel = 'Thickeness [m]'
301             title = 'Stress distribution (global coordinate system)'
302         elif k == 1: # Strain in the global coordinate system
303             fun = strainx
304             xlabel = 'Strain [-]'
305             ylabel = 'Thickeness [m]'
306             title = 'Strain distribution (global coordinate system)'
307         elif k == 2: # Stress in the fiber coordinate system
308             fun = stressf*10**-6
309             xlabel = 'Stress [MPa]'
310             ylabel = 'Thickeness [m]'
311             title = 'Stress distribution (local coordinate system)'
312         elif k == 3: # Strain in the local coordinate system
313             fun = strainf
314             xlabel = 'Strain [-]'
315             ylabel = 'Thickeness [m]'
316             title = 'Strain distribution (local coordinate system)'
317
318         if k == 0 or k == 2:
319             label = ['S11', 'S22', 'S12']
320
321         else:
322             label = ['eps1', 'eps2', 'eps6']
323
324         color = ['black', 'red', 'blue']
325         handles = []
326
327         for i in range(3):
328
329             plt.plot(fun[i], z[0], color=color[i])
330
331             handles.append(Line2D([0], [0], color=color[i], lw=2, label=label[i]))
332
333         plt.xlim(np.min(fun), np.max(fun))
334         plt.ylim(np.min(z), np.max(z))
335         plt.xlabel(xlabel)
```

```
336         plt.ylabel(ylabel)
337         plt.legend(handles=handles, labels = label, labelcolor = color)
338         plt.title(title)
339         plt.grid()
340         plt.show()
341 
342 def store_CLT(z, stressx, strainx, stressf, strainf, output_folder, specimen): # Just to store the CLT if intended
343 
344     z = z.reshape(1, -1)
345 
346     for i in range(3):
347 
348         if i == 0:
349             dir = '11'
350         elif i == 1:
351             dir = '22'
352         else:
353             dir = '12'
354 
355         with open(output_folder+f'{specimen+1}clt_{dir}_fpf.txt', 'w') as file:
356 
357             file.write('z [mm] \t Stressx [MPa} \t Stressf [MPa} \t Strainx [-} \t Strainf [-}\n')
358 
359         with open(output_folder+f'{specimen+1}clt_{dir}_fpf.txt', 'a') as file:
360 
361             for h, sx, sf, stx, stf in zip(z[0], stressx[i], stressf[i], strainx[i], strainf[i]):
362 
363                 file.write(f"{h*1000}\t{sx*10**-6}\t{sf*10**-6}\t{stx*100}\t{stf*100}\n")
```

Appendix B

Code validation

B.1 Laminate 1

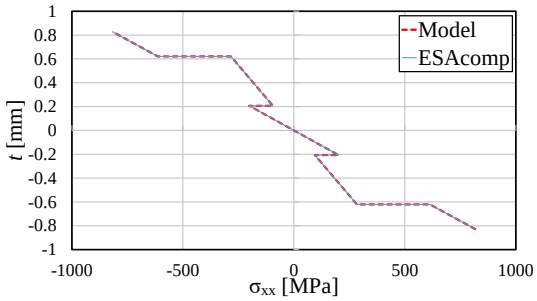

(a) σ_{xx}

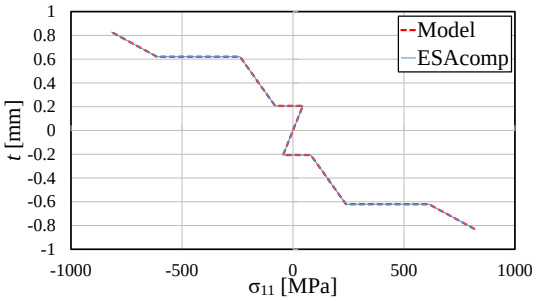

(b) σ_{11}

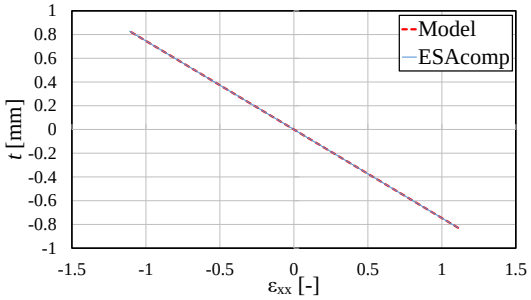

(c) σ_{yy}

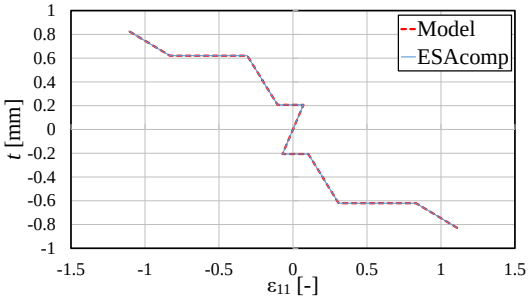

(d) σ_{22}

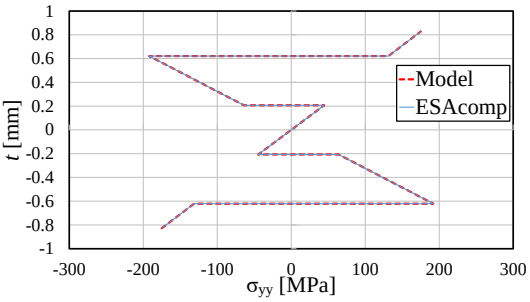

(e) σ_{xy}

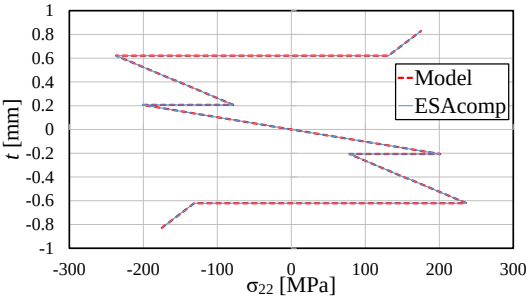

(f) σ_{12}

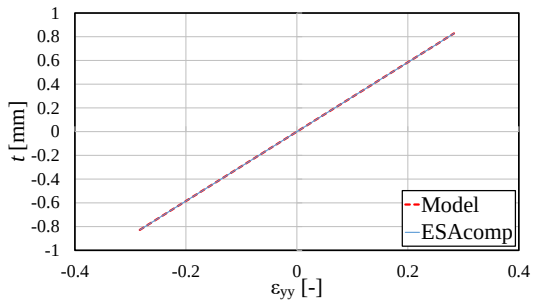

(g) ε_{xx}

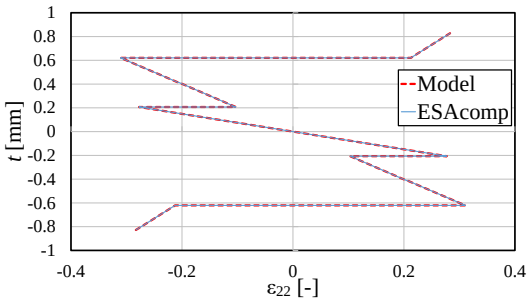

(h) ε_{11}

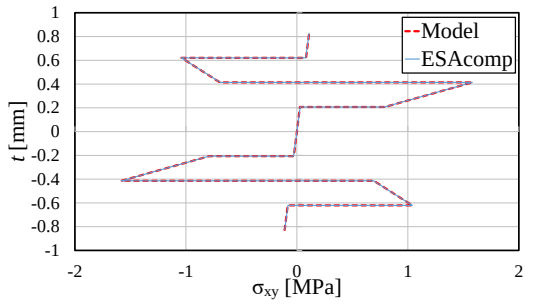

(i) ε_{yy}

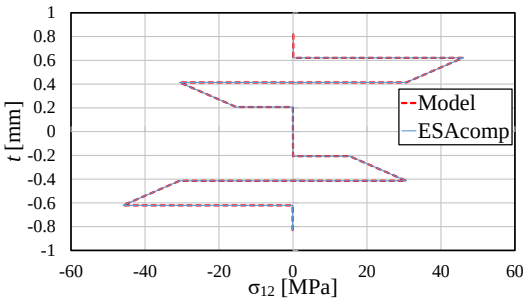

(j) ε_{22}

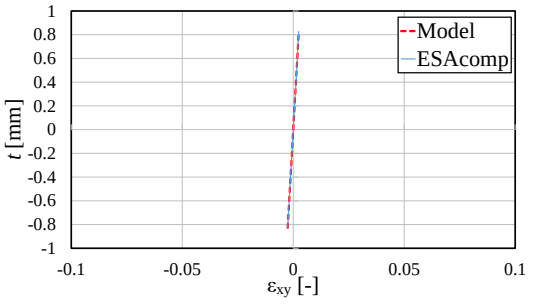

(k) ε_{xy}

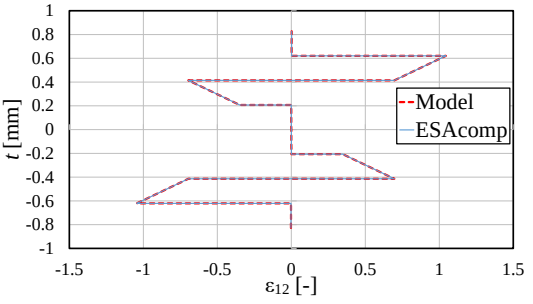

(l) ε_{12}

B.2 Laminate 2

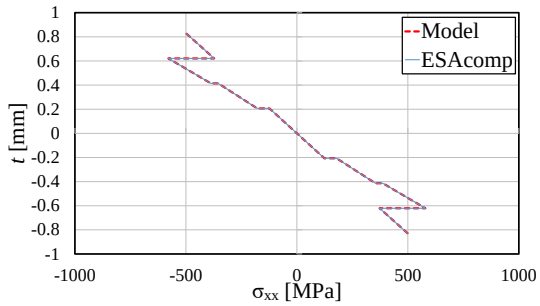

(a) σ_{xx}

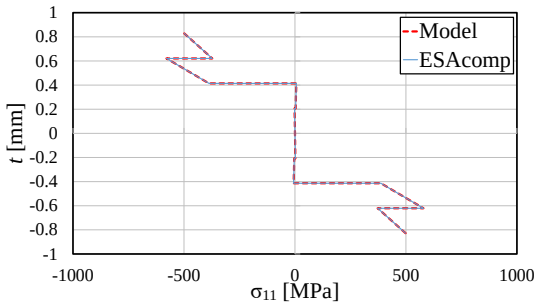

(b) σ_{11}

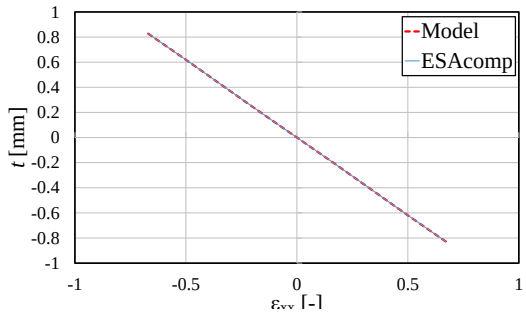

(c) σ_{yy}

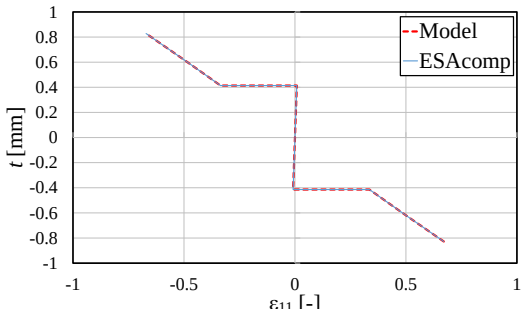

(d) σ_{22}

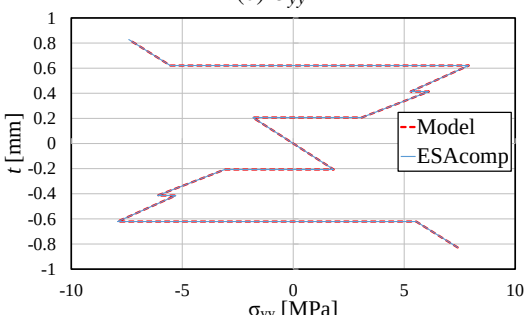

(e) σ_{xy}

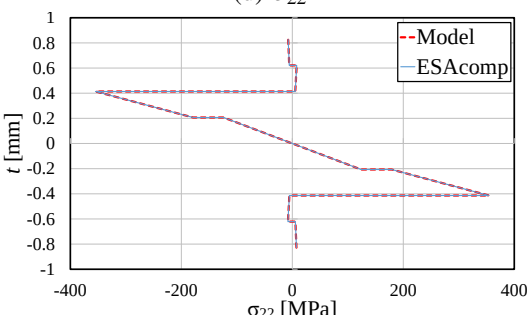

(f) σ_{12}

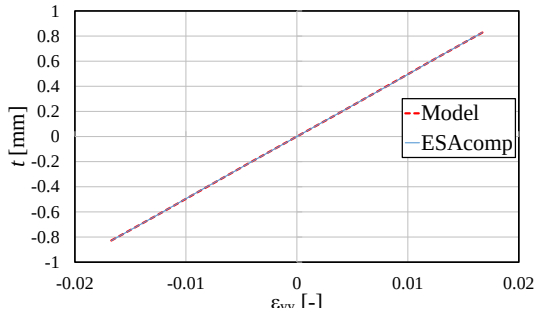

(g) ε_{xx}

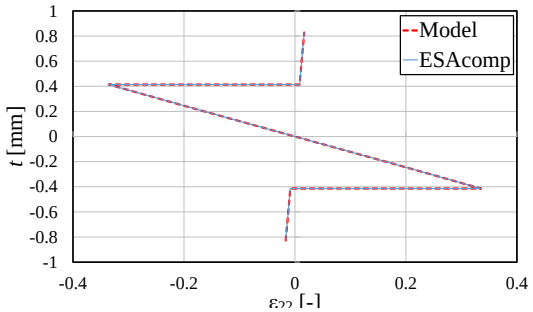

(h) ε_{11}

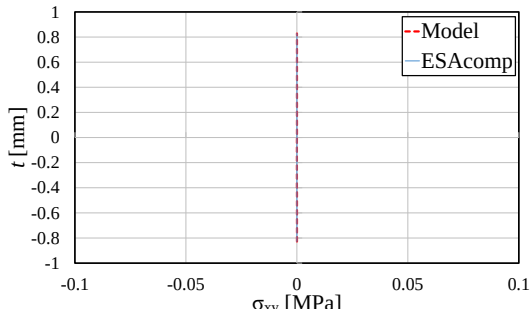

(i) ε_{yy}

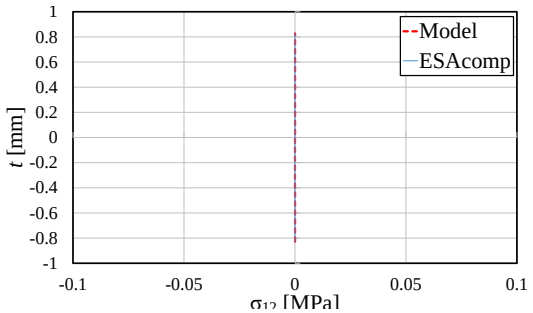

(j) ε_{22}

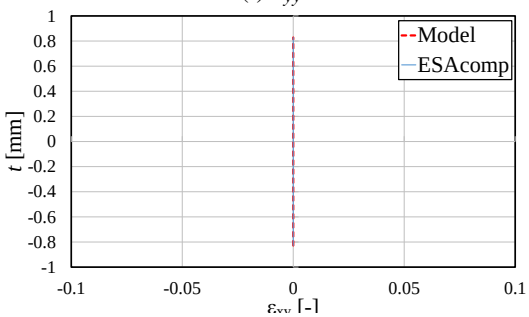

(k) ε_{xy}

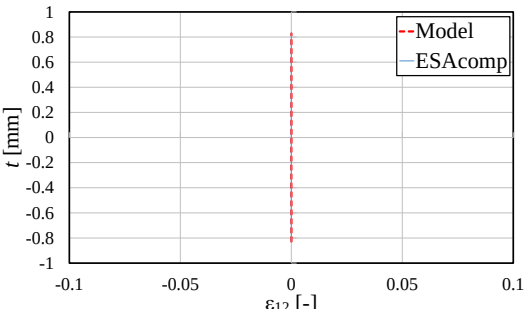

(l) ε_{12}

B.3 Laminate 3

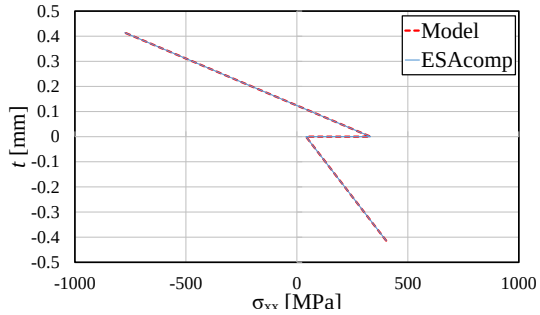

(a) σ_{xx}

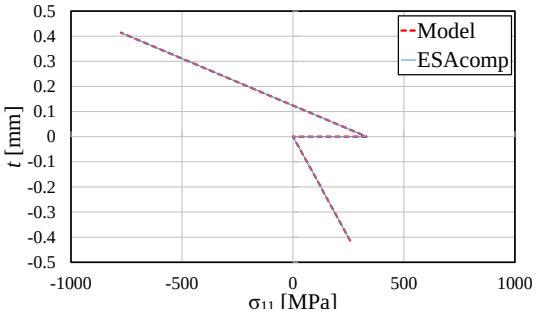

(b) σ_{11}

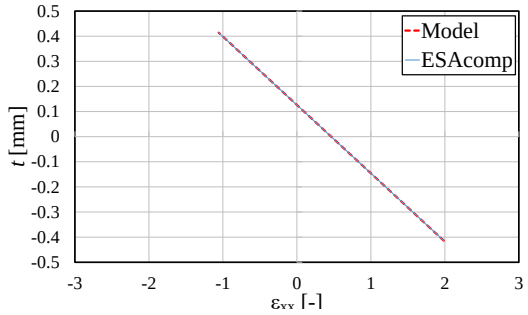

(c) σ_{yy}

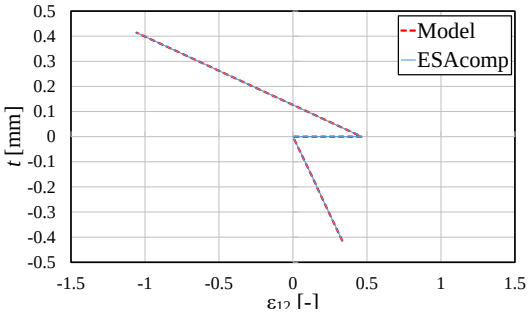

(d) σ_{22}

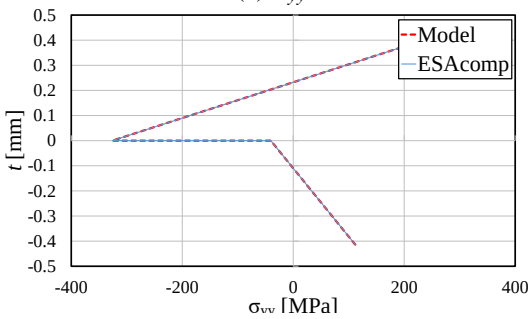

(e) σ_{xy}

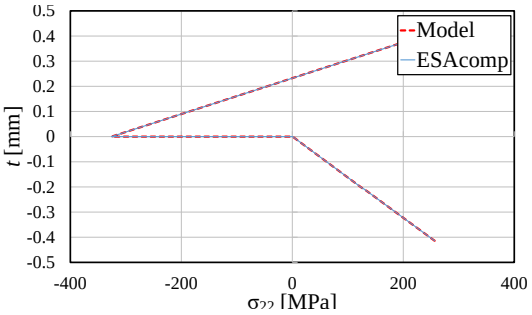

(f) σ_{12}

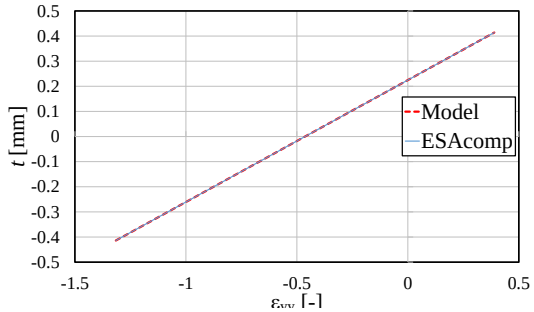

(g) ε_{xx}

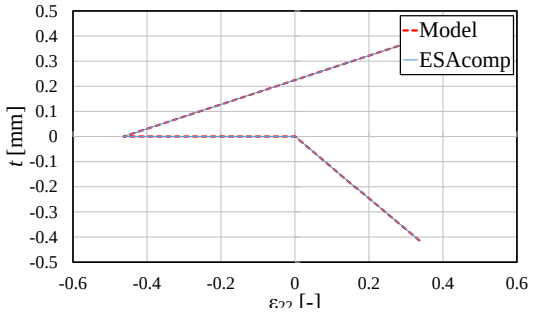

(h) ε_{11}

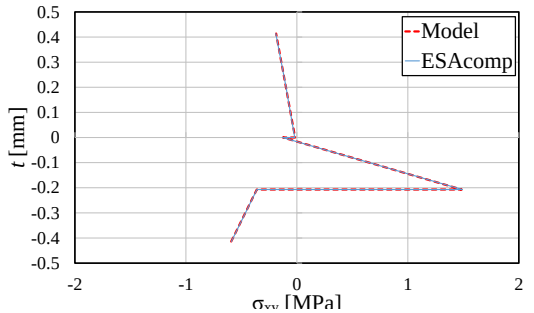

(i) ε_{yy}

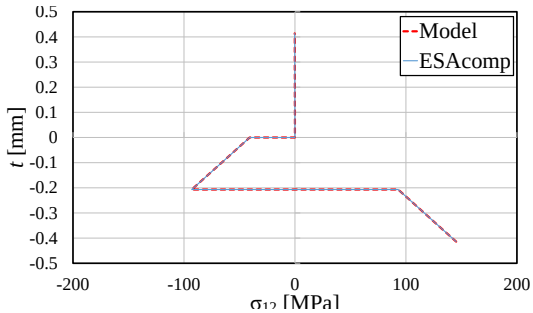

(j) ε_{22}

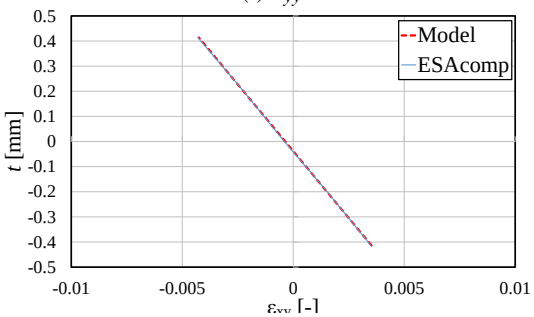

(k) ε_{xy}

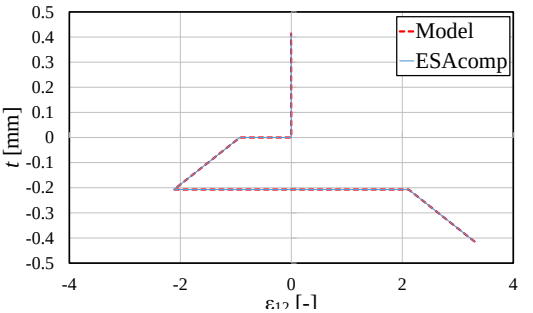

(l) ε_{12}

B.4 Laminate 4

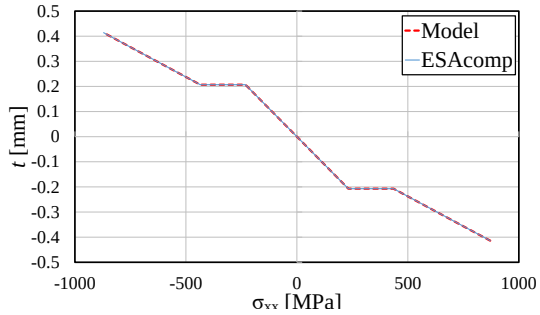

(a) σ_{xx}

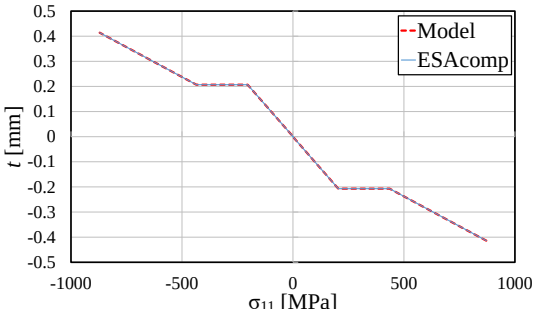

(b) σ_{11}

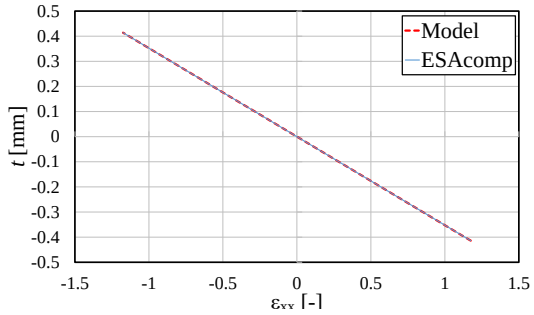

(c) σ_{yy}

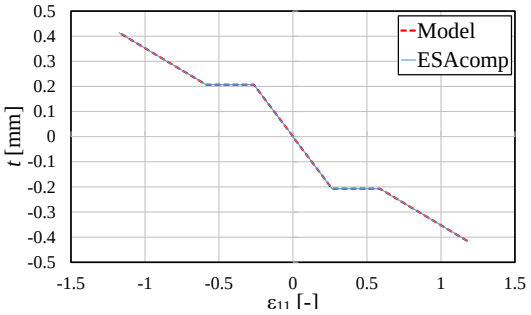

(d) σ_{22}

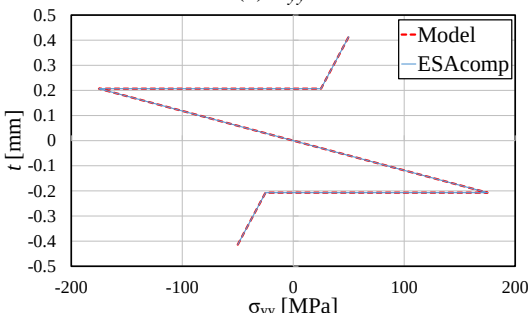

(e) σ_{xy}

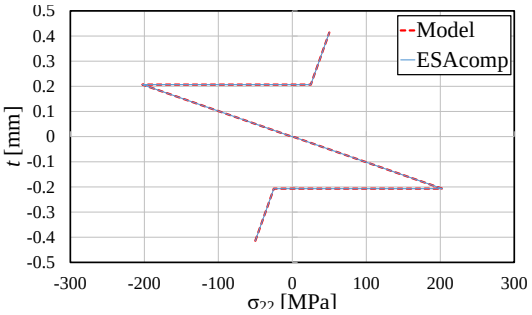

(f) σ_{12}

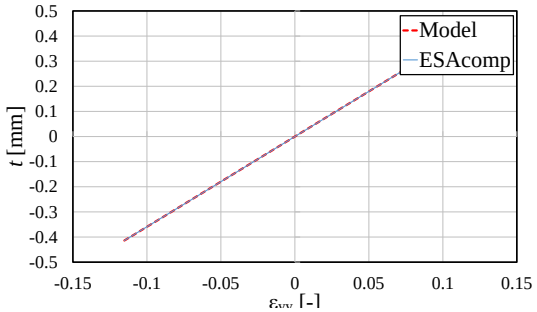

(g) ε_{xx}

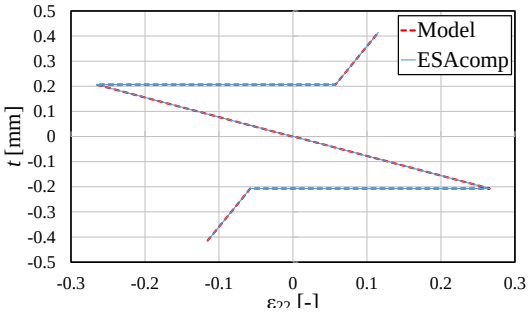

(h) ε_{11}

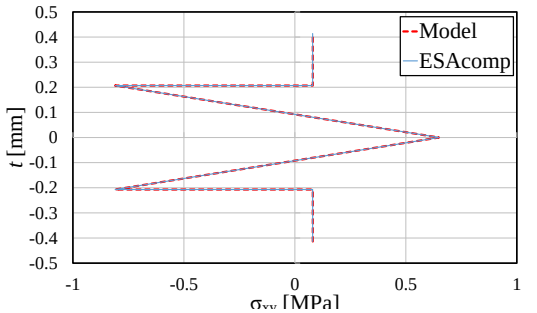

(i) ε_{yy}

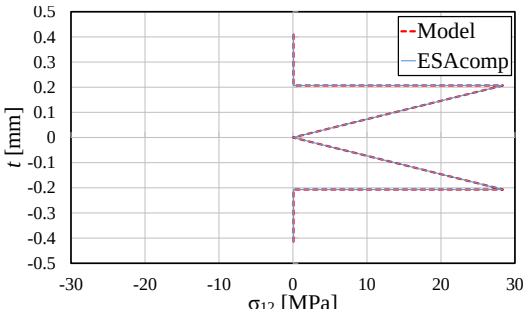

(j) ε_{22}

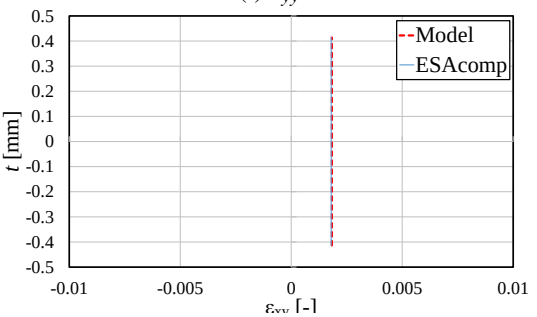

(k) ε_{xy}

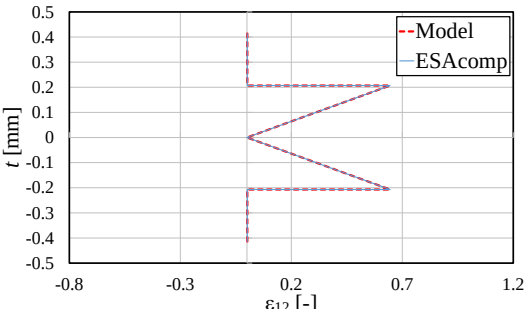

(l) ε_{12}